Elucidation of Isotropic and Anisotropic Shear Elasticity of *in vivo* Soft Tissue using Planar Magnetic Resonance Elastography

DISSERTATION

zur Erlangung des akademischen Grades

Dr. Rer. Nat.
im Fach Physik

eingereicht an der
Mathematisch-Naturwissenschaftlichen Fakultät I
der Humboldt-Universität zu Berlin

von
Dipl.-Phys. Sebastian Papazoglou
geboren am 25.02.1972 in Kiel

Präsident der der Humboldt-Universität zu Berlin:
Prof. Dr. Dr. h.c. Christoph Markschies

Dekan der Mathematisch-Naturwissenschaftlichen Fakultät I:
Prof. Dr. Lutz-Helmut Schön

Gutachter:
1. Prof. Dr. Jürgen Rabe
2. Prof. Dr. Gerd Buntkowsky
3. Dr. Ingolf Sack

eingereicht am: 19.12.2008
Tag der mündlichen Prüfung: 27.07.2009

An aller erster Stelle möchte ich mich bei meinem Betreuer, dem Arbeitsgruppenleiter der AG Sack am Institut für Radiologie der Charité Dr. Ingolf Sack, für die Gelegenheit bedanken über das spannende Thema der MR Elastographie zu promovieren. Ebenso gilt mein Dank meinen Kollegen Dr. Jürgen Braun, Dieter Klatt, Dr. Uwe Hamhaber, Dr. Jens Rump, Chao Xu, Dr. Katrin Rettig, Dr. Hasan Nuzha, Dr. Thomas Elgeti, Dr. Patrick Asbach und Dr. Bernd Beierbach für die zahlreichen anregenden Diskussionen. "Last but not least"gilt meinen Eltern ein ganz besonderer Dank für ihre Unterstützung. Vielen Dank!

Abstract

Magnetic resonance elastography (MRE) is a noninvasive method that allows the determination of *in vivo* shear elasticity of soft tissues. In this thesis methods for the determination of isotropic and anisotropic shear elasticities from MRE wave data were developed and evaluated. All methods presented in this work are based on planar MRE, i.e. they are based on the measurement of a single displacement component in the image plane. This way measurement time in MRE is greatly reduced. However, this imposes specific requirements on data evaluation in order to determine significant elastic constants. On the basis of planar MRE experiments on tissue mimicking gels, human skeletal muscle and numerical simulations it is demonstrated that correct shear elasticities can be determined, taking into account a small set of experimental boundary conditions as well as the employment of complementary data evaluation strategies. This thesis is particularly focussed on the analysis of noise and image resolution on the determined elastic constants. Moreover, methods for determining anisotropic elasticity and analyzing shear wave scattering effects on MRE wave data are introduced. The investigated influences on wave amplitudes and wave lengths are compared and discussed to develop a simple measurement protocol for the evaluation of *in vivo* MRE data. All methods employed in this work are summarized in the appendix along with the corresponding computer code, which is available on demand.

Zusammenfassung

Die Magnetresonanzelastographie (MRE) stellt ein nichtinvasives Verfahren dar, welches die Bestimmung der *in vivo* Scherelastizität weicher Gewebe ermöglicht. Im Rahmen diese Arbeit wurden Methoden zur Bestimmung isotroper und anisotroper Scherelastizitäten anhand von MRE Wellenbildern entwickelt und evaluiert. Alle in dieser Arbeit vorgestellten Methoden basieren auf planarer MRE, d.h. auf der Aufnahme einer einzelnen Auslenkungskomponente innerhalb der Bildschicht. Dadurch wird die MRE erheblich beschleunigt. Allerdings stellen sich dadurch auch besondere Anforderungen an die Datenauswertung zur Bestimmung aussagekräftiger elastischer Kenngrößen. Anhand von planaren MRE-Experimenten an Gewebephantomen und menschlicher Skelettmuskulatur sowie mittels numerischer Simulation wird gezeigt, dass bei Beachtung weniger experimenteller Randbedingungen und einer darauf abgestimmten Datenauswertung, korrekte Elastizitäten ermittelt werden können. Ein besonderer Schwerpunkt der Arbeit liegt in der Analyse experimenteller Einflüsse wie Bildrauschen und -auflösung auf die ermittelten elastischen Kenngrößen. Des Weiteren werden Methoden zur Bestimmung anisotroper Elastizitäten sowie zur Analyse von Streueffekten im MRE-Wellenbild vorgestellt. Die behandelten Einflüsse auf die Amplituden und Wellenlängen im MRE-Bild, werden vergleichend diskutiert und zusammengefasst, um ein einfaches Verfahrensprotokoll zur Analyse experimenteller *in vivo* MRE-Daten zu entwickeln. Alle in dieser Arbeit verwendeten Methoden und Programme sind im Anhang zusammengefasst und auf Anforderung erhältlich.

The results presented in this thesis led to the following publications in international peer-reviewed journals

- Papazoglou S, Braun J, Hamhaber U, Sack I. 2005 Two-dimensional waveform analysis in MR elastography of skeletal muscles. *Physics in Medicine and Biology* **50**(1) 1313-1325
- Papazoglou S, Rump J, Braun J, Sack I. 2006 Shear wave group velocity inversion in MR elastography of human skeletal muscle. *Magnetic Resonance in Medicine* **56**(6) 489-497
- Papazoglou S, Hamhaber U, Braun J, Sack I. 2007 Horizontal shear wave scattering from a nonwelded interface observed by magnetic resonance elastography. *Physics in Medicine and Biology* **52**(3) 675-684
- Papazoglou S, Hamhaber U, Braun J, Sack I. 2008 Algebraic Helmholtz inversion in planar magnetic resonance elastography. *Physics in Medicine and Biology* **53**(12) 3147-58
- Papazoglou S, Xu C, Hamhaber U, Siebert E, Bohner G, Klingebiel R, Braun J, Sack I 2009 Scatter-based MR Elastography. *Physics in Medicine and Biology* **54** 2229-41

Moreover, the author has contributed to the publications

- Hamhaber U, Sack I, Papazoglou S, Rump J, Klatt D, Braun J. 2006 Three-dimensional analysis of shear wave propagation observed by in vivo magnetic resonance elastography of the brain. *Acta Biomaterialia* **3**(1) 127-137
- Rump J, Braun J, Papazoglou S, Taupitz M, Sack I. 2006 Alterations of the proton-T2 time in relaxed skeletal muscle induced by passive extremity flexions. *Journal of Magnetic Resonance Imaging* **23**(4) 541-546
- Klatt D, Asbach P, Rump J, Papazoglou S, Somasundaram R, Modrow J, Braun J, Sack I. 2006 In vivo determination of hepatic stiffness using steady-state free precession magnetic resonance elastography. *Investigative Radiology* **41**(12) 841-848
- Elgeti T, Rump J, Hamhaber U, Papazoglou S, Hamm B, Braun J, Sack I. 2008 Cardiac magnetic resonance elastography. Initial results. *Investigative Radiology* **43**(11) 762-72
- Sack I, Beierbach B, Würfel J, Klatt D, Papazoglou S, Hamhaber U, Martus P, Braun J 2008 The impact of aging and gender on brain viscoelasticity, *Neuroimage* under revision
- Würfel J, Paul F, Beierbach B, Klatt D, Papazoglou S, Hamhaber U, Zipp F, Martus P, Braun J, Sack I 2008 Magnetic Resonance Elastography Reveals Degradation of Tissue Integrity in Multiple Sclerosis, *Neuroimage*, submitted

And finally, the following results have been presented on international congresses

- Papazoglou S, Kramer B, Kettemann S. 2003 1D Anderson localization including next-nearest neighbour hopping. *Proceedings of the 67th spring meeting of the German Physical Society (DPG), Dresden, Germany*

- Papazoglou S, Braun J, Taupitz M, Sack I. 2004 Determination of anisotropic elasticities of in vivo skeletal muscle using a geometric analysis of MR-elastography wave patterns *Proceedings of the Third Conference on the Ultrasonic Measurement and Imaging of Tissue Elasticity, Lake Windermere, UK*

- Papazoglou S, Sack I, Hamhaber U, Rump J, Klatt D, Braun J. 2005 Elucidation of in vivo anisotropic elasticities by MR elastography: Application to skeletal muscle. *Proceedings of the International Society of Magnetic Resonance in Medicine, Miami Beach, Florida, USA* **13** 593

- Papazoglou S, Rump J, Klatt D, Hamhaber U, Braun J, Sack I. 2006 Group-velocity inversion in MR elastography on skeletal muscles. *Proceedings of the International Society of Magnetic Resonance in Medicine, Seattle, Washington, USA* **14** 2557

- Papazoglou S, Rump J, Klatt D, Hamhaber U, Braun J, Sack I. 2006 Influence of the transducer near field in MR elastography wave images. *Proceedings of the International Society of Magnetic Resonance in Medicine, Seattle, Washington, USA* **14** 3039

- Papazoglou S, Rump J, Klatt D, Hamhaber U, Braun J, Sack I. 2007 Position dependent shear wave group velocities in in vivo human biceps muscle. *Proceedings of the International Society of Magnetic Resonance in Medicine, Berlin, Germany* **15** 1258

- Papazoglou S, Klatt D, Braun J, Sack I. 2008 Viscoelastic properties of the human brain analyzed by a novel two-compartment effective medium model. *Proceedings of the Seventh Conference on the Ultrasonic Measurement and Imaging of Tissue Elasticity, Austin, Texas, USA*

Abbreviations

Abbreviation	Description
AHI	Algebraic Helmholtz Inversion
b-SSFP	Balanced Steady-State Free Precession
CT	Computer Tomography
EPI	Echo Planar Imaging
FE, RO	Frequency Encode, Read Out
FID	Free Induction Decay
FOV	Field of View
FT	Fast Transverse Mode
GVI	Group Velocity Inversion
MEG	Motion Encoding Gradient
MR	Magnetic Resonance
MRE	MR Elastography
MRI	MR Imaging
P	Pressure
PE	Phase Encode
PET	Positron Emission Tomography
PSD	Phase Sensitive Detection
RF	Radio Frequency
ROI	Region of Interest
SH	Shear Horizontal
SPECT	Single Photon Emission Computed Tomography
SS	Slice Select
ST	Slow Transverse Mode
SV	Shear Vertical
US	Ultrasound

Mathematical Symbols

Symbol	Description
$\mathbf{B}_0$	Field vector of the static field of the MR scanner ($B_0 = \|\mathbf{B}_0\|$)
c	Phase speed
c^*	Apparent phase speed
c_s	Phase speed of the shear wave
c_p	Phase speed of the pressure wave
$\mathbf{C}$	Elastic tensor
C_{ijkl}	Cartesian components of the elasticity tensor
C_{ij}	Components of the elasticity tensor in Voigt's notation
δ_{ij}	Kronecker delta, i.e. $\delta_{ij} = 1$ for $i = j$ and $\delta_{ij} = 0$ else
$\delta(\mathbf{x} - \mathbf{x}'), \delta(t - t')$	Delta distribution
D	Local density of magnetic moments
$\triangle$	Laplace operator
ffl	Strain tensor
ϵ_{kl}	Cartesian components of the strain tensor
E, E_j	Young's moduli
$\mathbf{f}$	Force vector
f_i	Cartesian components of the force vector
Φ	Phase of the MR signal, i.e. the phase signal
γ	Gyromagnetic ratio of the proton
$\mathbf{G}$	Magnetic field gradient
$\mathbf{G}_{ss}, \mathbf{G}_{pe}, \mathbf{G}_{ro}$	Magnetic field gradients for spatial encoding
$\mathbf{\Gamma}$	Christoffel tensor
Γ_{ij}	Cartesian components of the Christoffel tensor
G_{jk}	Cartesian components of the Green's tensor
η	Viscosity according to the Voigt model
$\mathbf{k}$	Wave vector
k_1, k_2, k_3	Cartesian components of $\mathbf{k}$
κ	Specific compliance
λ	Wave length
$\mathbf{M}$	Macroscopic magnitization
M_1, M_2, M_3	Cartesian components of $\mathbf{M}$

Symbol	Description
μ, μ_{ij}	Shear moduli
ν, ν_{ij}	Poisson's ratios
∇	Nabla operator
$\Theta(t - t')$	Heaviside distribution
θ_{rel}	Phase difference between external vibration and MEG
ρ	Material density
R	Reflection coefficient
S	Complex signal measured by phase sensitive detection (PSD)
œ	Stress tensor
σ_{kl}	Cartesian components of the stress tensor
σ	Variance
$\mathbf{S}$	Compliance tensor
S_{ijkl}	Cartesian components of the compliance tensor
T_1	Longitudinal relaxation time
T_2	Transverse relaxation time
T_2^*	Transverse relaxation time including static field inhomogeneities
T_E	Echo time
T_P	Repitition time
ø	Traction vector
τ_1, τ_2, τ_3	Cartesian components of **ø**
T	Transmission coefficient
U	Voltage induced in a spin resonance experiment
$\mathbf{u}$	Vector of displacement
u_1, u_2, u_3	Cartesian components of $\mathbf{u}$
$\hat{\mathbf{u}}$	Temporal Fourier transform of the displacement vector
$\mathbf{v}$	Group velocity vector
v_1, v_2, v_3	Cartesian components of $\mathbf{v}$
ω_L	Larmor frequency
ω_{ext}	External vibration frequency
$\mathbf{x}$	Position vector
x_1, x_2, x_3	Cartesian components of $\mathbf{x}$
ξ	Specific stiffness, i.e. the inverse of κ
∂_j^n	Shorthand for $\frac{\partial^n}{\partial x_j^n}$

Inhaltsverzeichnis

1 Introduction

Today medical imaging is important in diagnosis and therapy monitoring Webb [1988]. For instance, in positron emission tomography (PET) and single photon emission computed tomography (SPECT) injected radionuclides are used to trace metabolic pathways or receptor proteins inside the human body. While PET and SPECT are sensitive to functional aspects they are less suited to display tissue structure. A much better spatial resolution is achieved by ultrasound (US), computed tomography (CT) and magnetic resonance imaging (MRI). In standard US the contrast is based on the speed of compressional waves in the tissue.The imaging contrast in CT depends on the material density and the absorption rate of atoms. The native proton-MRI signal is related to density and chemical environment of water protons. US, CT and MRI yield an excellent contrast and allow the distinction between different types of tissues. However, their contrast mechanisms are not directly related to the connectivity and assemblage of cells. These tissue-structural properties are important in diagnosis as they change dramatically with progression of tumors, fibrosis and degenerative diseases Fung [1993], Sarvazyan [1998], Humphrey [2003]. Soft tissues are nearly incompressible and hence changes in cell adhesion and rigidity primarily affect shear elasticity. The shear modulus is intuitively tested by the physician's fingers during palpation. Although palpation is an important diagnostic means, its reproducibility and comparability is limited. Futhermore, it strongly depends on the experience of the physician and depends on the accessibility of the tissue under investigation. Therefore it would be desirable to have an imaging-based modality for measuring the shear modulus of soft tissues. Such an äpparative"palpation is achieved by elastography, which was first introduced using US and static tissue deformation Parker et al. [1990], Yamakoshi et al. [1990], Lerner et al. [1990], Ophir et al. [1991], Skovoroda et al. [1995]. This initial elastography technique was still not able to examine soft tissues deep inside the human body. Moreover, ultrasound requires an acoustic window, which severely limits the applicability of US elastography, e.g. on brain or in obese patients. In contrast, magnetic resonance elastography (MRE) allows for the first time the measurement of tissue shear elasticity without these principle limitations Muthupillai et al. [1995, 1996], Plewes et al. [1995], Lewa and DeCertaines [1996]. MRE combines an externally applied oscillating stress with the motion sensitivity of the MR phase signal to visualize propagating shear waves inside the human body. From the measured wave images shear elasticity can be determined as a function of position by solving an appropriate inverse problem. To date, MRE has been successfully applied to in vivo liver Ziol et al. [2005], Klatt et al. [2006], Rouviere et al. [2006], Huwart et al. [2006], Klatt et al. [2007], Yin et al. [2007], brain Braun [2002], McCracken et al. [2005], Hamhaber et al. [2007], Sack et al. [2008], Kruse et al. [2008], breast Sinkus et al. [2000], Lorenzen et al. [2002], Van Houten et al. [2003], Sinkus et al.

[2005b,a, 2007] and skeletal muscle Dresner et al. [2001], Basford et al. [2002], Sack et al. [2002], Jenkyn et al. [2003], Heers et al. [2003], Uffmann et al. [2004], Oida Kang et al. [2005], Papazoglou et al. [2005], Galban et al. [2005a,b], Bensamoun et al. [2005, 2006], Papazoglou et al. [2006], Ringleb et al. [2007], Bensamoun et al. [2008].

Aside its potential in the clinic, MRE is a unique technique for fundamental studies of time resolved bulk shear waves in three dimensions. To date no other technique is able to capture the complete vector field of shear displacement directly at the location of the scattering entities. However, the inverse problem for calculating elastic constants is ill-posed due to the presence of noise and due to a lack of knowledge on boundary conditions Colton and Kress [1997], Barbone and Gokhale [2004]. A number of strategies are in use for solving the inverse problem in MRE such as direct algebraic inversions Sinkus et al. [2000], Bishop et al. [2000], Oliphant et al. [2001], combinations of forward simulation and optimization Van Houten et al. [1999, 2000], filtering techniques Knutsson et al. [1994], Braun et al. [2001] and manual evaluation of wave profiles Bensamoun et al. [2008]. A brief overview on inverse methods used in MRE can be found in Park and Maniatty [2006]. The methods can be further divided into methods relying on the measurement of the whole vector of displacement or methods based on only a single component of displacement. For developing clinically applicable techniques it is important to address patient comfort and time requirements. Therefore, in many MRE applications only a single Cartesian component of the displacement field is measured in a single image plane in many MRE applications Rouviere et al. [2006], Klatt et al. [2007], Yin et al. [2007], Sack et al. [2008], Kruse et al. [2008], Papazoglou et al. [2006], Bishop et al. [2000]. The reduction of information following from such planar measurements may increase the sensitivity of MRE to boundary effects, noise and anisotropy.

This work is dedicated to the development and the analysis of inversion methods applied to fast planar MRE. Both isotropic and anisotropic elasticity is accounted for. The performance of direct algebraic inversion in MRE is analyzed and an experimental setup is developed that helps to reduce methodological biases on the measured shear elasticity. Boundary effects imposed by elastic interfaces are studied and an MRE method is introduced, that allows the estimation of the degree of weldedness of tissue interfaces. Moreover, the anisotropy of human muscle tissue is elucidated. An analysis of shear anisotropy of human biceps brachii based on a 2D geometric wave form analysis is presented and an inversion method based on group velocity measurements is developed and validated. Since this work can be divided into three projects, the general structure of this thesis is in the order:

1. determination of the shear modulus in isotropic materials,
2. measurement of the specific compliance of elastic interfaces and
3. analysis of shear anisotropy of in vivo human biceps.

In chapter two the theoretical background on MRE and elastic wave propagation is provided. In chapter three the experiments are described and numerical methods employed for the simulation of elastic waves are explained. The results are presented in chapter four and discussed in chapter five. A summary is given in chapter seven and details on numerical methods for wave field simulation as well as the description of developed Matlab code are given in the appendix.

2 Theoretical Background

The following chapter provides the mathematical background on MR imaging of displacement fields and the propagation of linear waves. A detailed description of MRI in general can be found in Liang and Lauterbur [2000], Bernstein et al. [2004], whereas the background on linear wave propagation in isotropic and anisotropic materials is based on the monographs Landau and Lifshitz [1986], Aki and Richards [2002], Musgrave [1970], Fedorov [1968], Lai [1994].

2.1 MRI of Elastic Waves

Nuclei possess a microscopic magnetic moment parallel to their spin. In MRI ^{1}H, ^{13}C, ^{19}F and ^{31}P are used whereby the most important nucleus is the single proton ^{1}H. Without external magnetic field the corresponding quantum mechanical states of ^{1}H are degenerate, i.e. spin-up or spin-down occupy the same energy eigenstate. In an external static magnetic field, henceforth denoted by $\mathbf{B}_0$, this degeneracy is lifted (see figure 2.1). As a result of non commutativity of the single spin components and the fact that spin is an angular momentum, the microscopic moments then precess about the external field vector $\mathbf{B}_0$ at the Larmor frequency given by

$$\omega_L = \frac{\triangle E}{\hbar} \quad = \quad \gamma B_0. \tag{2.1}$$

Here, $\gamma = 42.58\,\mathrm{MHz/T}$ is the gyromagnetic ratio of the proton. Depending on the temperature of the spin system, there are continued transitions between spin states parallel and anti-parallel to the magnetic field. However, on the average a very small excess of moments is aligned parallel to the field resulting a small macroscopic magnetization. This effect is called nuclear paramagnetism, in analogy to the atomic paramagnetism. In his original paper Bloch estimated the bulk magnetization for a spin-1/2 system at room temperature ($T = 291$ K) in a field of 1 T using the Curie formula for the paramagnetic susceptibility, obtaining 0.1^{-9}T Bloch [1946]. At the same field strength, the Larmor frequency $\omega_L = 42.58$ MHz lies in the radio frequency (RF) regime. Thus, by an external RF-pulse which satisfies the resonance condition

$$\omega_{rf} = \omega_L, \tag{2.2}$$

energy can be transmitted to the spin system inducing transitions, given that the pulse features a component perpendicular to $\mathbf{B}_0$. This phenomenon called spin resonance is the foundation of NMR spectroscopy as well as MRI. After the RF-pulse is switched

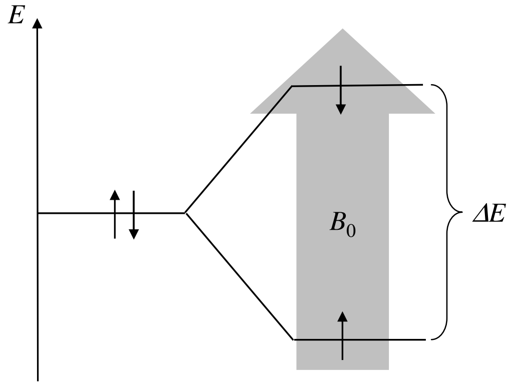

Abbildung 2.1: Zeemann splitting of a spin- 1/2 nucleus in an external magnetic field B_0.

off, the system returns into the state of equilibrium by transmitting energy, again in radio frequency regime. Since in MRI the macroscopic magnetic moment is the relevant quantity it is henceforth termed magnetic moment. The equation of motion for the resulting magnetic moment per unit volume, i.e. magnetization $\mathbf{M}$ ($[\mathbf{M}]$=Am^{-1}) and for a field $\mathbf{B}_0$ pointing along x_3, is the Bloch equation Bloch [1946], Torrey [1956]

$$\frac{d\mathbf{M}}{dt} = \gamma \mathbf{M} \times \mathbf{B}(t) - \frac{M_1 \hat{\mathbf{e}}_1 + M_2 \hat{\mathbf{e}}_2}{T_2} - \frac{(M_3 - M_{3,0})\, \hat{\mathbf{e}}_3}{T_1}. \tag{2.3}$$

Here, $M_{3,0}$ represents equilibrium magnitization along x_3. T_1 and T_2 denote times, that characterize the relaxation processes which influence the time evolution of the magnetization after excitation. According to the component of magnetization they effect, they are also referred to as longitudinal and transverse relaxation time. Microscopically, relaxation of the transverse component is influenced by spin-spin interactions, while the longitudinal relaxation is effected by spin-lattice interactions Slichter [1992]. More rigorously, the relaxation of the transverse component of magnetization is influenced by local field inhomogeneities. These are due to imperfections of the static field. If such effects are taken into account, the corresponding relaxation time is denoted T_2^*. In general $T_1 \geq T_2 > T_2^*$ whereby in living tissue one typically finds $T_1 = 300$ to 2000 ms and for $T_2 = 30$ to 150 ms. Moreover, the Coulomb shielding in different chemical environments causes a chemical shift of the Larmor frequencies. An ensemble of spins precessing at the same frequency is also called isochromat. In a static field the magnetic moment is simply aligned parallel to the field, since it has no net angular momentum due to the randomness of the phases of the microscopic moments. An RF-pulse results phase coincidence of the spins. Depending on the duration and field strength of the RF-pulse, the macroscopic magnetization is tilted away from its equilibrium position by a flip angle α. In MRI the RF-pulses is named accordingly α-pulse, e.g. 90°-pulse or $\pi/2$-pulse. After the RF-pulse, the magnetic moments precess freely about $\mathbf{B}_0$. During free precession the transverse components of the microscopic moments start to

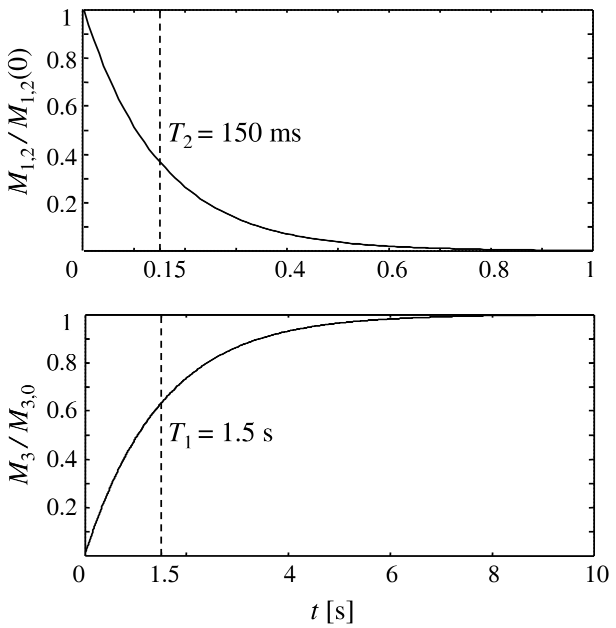

Abbildung 2.2: Temporal evolution of the transverse and the longitudinal magnetization $M_{x,y}$ and M_z after an RF-pulse as observed in a reference frame rotating with ω_L about x_3 (aligns 2.4).

dephase, causing a decrease in total transverse magnetization. Simultaneously, the longitudinal component increases until it has reached its equilibrium value depending on B_0. In a frame rotating with ω_L counterclockwise about the x_3-axis the components of magnetization can be written as

$$\begin{aligned} M_{1,2}(t) &= M_{1,2}(0)e^{-t/T_2}, \\ M_3(t) &= M_{3,0}\left(1 - e^{-t/T_1}\right) + M_3(0)e^{-t/T_1}, \end{aligned} \tag{2.4}$$

where $M_{1,2}(0)$ and $M_3(0)$ are the transverse and longitudinal magnetizations after the RF-pulse was applied (see figure 2.2). The decrease of the transverse component is called free induction decay (FID). The change of the magnetic field leads to a time dependent magnetic flux through the receiver coil and thus a voltage is induced. By a theorem of reciprocity Hoult and Richards [1976], Insko et al. [1998] the measured signal can be written as

$$U(t) = -\frac{\partial \Phi}{\partial t} = -\frac{\partial}{\partial t}\int_{sample} \mathbf{B}(\mathbf{x}) \cdot \mathbf{M}(\mathbf{x}, t)\, dV(\mathbf{x}), \tag{2.5}$$

where $[U] = V$ and $\mathbf{B}$ is the current normalized magnetic field at the position of the magnetic dipole produced by a uniform current inside the loop. In practice quadrature detection is used for signal detection, where the high-frequency signal is fed into two phase sensible detection (PSD) systems. In each PSD the signal is multiplied by a low-frequency sinusoidal reference signal, whereby the reference signals have a relative 90° phase shift. Afterward, they are recombined and low-pass filtered. This has two effects: First, the signal is not high-frequency anymore. Second, through the phase shift of the two reference signals, the measured signal can be combined to the complex signal

$$S(t) = S_1(t) + iS_2(t) \tag{2.6}$$

and hence both magnitude and phase of the signal are known. The complex signal can be brought into the form

$$S(t) = \int_{sample} D(\mathbf{x}) e^{i\Theta(\mathbf{x},t)} dV(\mathbf{x}), \tag{2.7}$$

where $D(\mathbf{x})$ represents the local density of magnetic moments. The phase $\Theta(\mathbf{x}, t)$ provides the key to a spatial localization of the signal as well as to motion encoding as explained in the next subsections.

Echo signals

Rapid spin dephasing due to static field inhomogeneities (governed by T_2^*) can be refocused by conducting a spin echo experiment Hahn [1950]. In a spin echo experiment a 180°-pulse is applied to the sample a time T after the excitation RF-pulse. After $2T$ the spins are rephased and an echo signal is received. The time $2T = T_E$ is referred to as the echo time. Multiple echo pulses yield a decreasing echo signal solely governed by T_2.

An echo signal can also be produced by using a magnetic gradient field (gradient echo). After the excitation pulse, a gradient is applied and as a result spins start to dephase corresponding to the strength and direction of the field gradient. If the gradient is inverted rephasing occurs. Since the gradient cannot balance field inhomogeneities of the static field $\mathbf{B}_0$, the decay of a gradient echo signal is governed by T_2^*. Signal acquisition takes place during the echo. Both the increase and the decrease of the echo signal is acquired for a symmetrical readout of k-space.

2.1.1 Spatial Encoding

Imaging requires the measured signal to be related to a specific location within the sample. In MRI this is achieved by applying weak gradient fields ($\sim$ 10 mT/m) in addition to the static field. Generally, the application of a linear gradient field G leads to a position dependence of the Larmor frequency according to

$$\omega_L(\mathbf{x}) = \gamma \left(B_0 + \mathbf{G} \cdot \mathbf{x} \right)$$

Three orthogonal gradients are used in MRI for spatial encoding.

Slice select gradient

The slice selection gradient G_{ss} is applied during RF-excitation. The application of a sinc shaped RF-pulse allows the excitation of magnetic moments located predominantly within a slice of thickness

$$h_{slice} = \frac{\triangle\omega}{\gamma G_{ss}}, \tag{2.8}$$

where $\triangle\omega$ is the bandwidth of the RF-pulse. This slice represents the image plane.

Phase encoding gradient

After spin excitation a further gradient perpendicular to G_{ss} is temporarily applied. Due to this gradient the spins accumulate a phase depending on their position inside the slice. Therefore this gradient is referred to as the phase encoding gradient G_{pe}. For a rectangular phase encoding gradient with duration T_{pe} the low-pass filtered phase encoded signal can be expressed as

$$S_{pe}(t) = \int_{slice} \rho(\mathbf{x}) e^{-i\gamma \mathbf{G}_{pe} \cdot \mathbf{x} T_{pe}} dV(\mathbf{x}). \tag{2.9}$$

Frequency encoding gradient

The third gradient is called frequency encoding gradient or read-out gradient. It is applied perpendicular to both G_{ss} and G_{pe} during signal acquisition, which results in a multi-frequency MR signal. A frequency encoded MR echo signal is of the form

$$S_{ro}(t) = \int_{slice} \rho(\mathbf{x}) e^{-i\gamma \mathbf{G}_{ro} \cdot \mathbf{x}(t-T_E)} dV(\mathbf{x}). \tag{2.10}$$

All spatial encoding gradients can be applied in any direction and hence an arbitrary imaging frame can be chosen.

k-space interpretation of the MR signal

The signal expressions (2.9) and (2.10) can formally transformed into Fourier transforms of the spin density distribution by the substitutions

$$\mathbf{k}_{pe} = \gamma \mathbf{G}_{pe} T_{pe} \tag{2.11}$$

and

$$\mathbf{k}_{fe} = \gamma \mathbf{G}_{fe}(t - T_E). \tag{2.12}$$

It is seen that at fixed T_{pe} the phase encoding gradient selects a distinct row in k-space whose position is given by the strength of the gradient G_{pe}. Thus in order to sample the

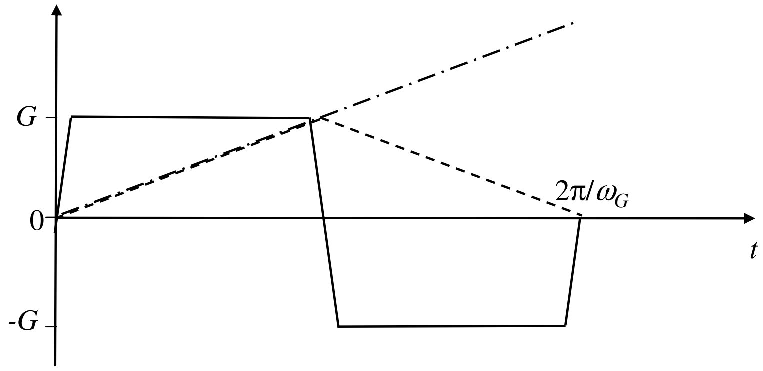

Abbildung 2.3: Schematic depiction of the effect ogf motion encoding with a trapezoidal MEG. The acquired phase of an isochromat at rest (dashed line) and a moving isochromat according to (2.17) (with $\omega_G = \omega_{ext}$) (dash dotted line) are superposed. At the end of the cycle at $t = 2\pi/\omega_G$ only the moving isochromat has accumulated a phase $\phi \neq 0$ due to the bipolar shape of the MEG.

whole k-space the gradient strength G_{pe} must be varied before each signal acquisition. Strategies for sampling k-space are described in detail in the literature Bernstein et al. [2004].

2.1.2 Motion Encoding

MRE employs the motion sensitivity of the spin phase of the protons, which is henceforth termed phase signal. The inherent motion sensitivity is a result of the high gyromagnetic ratio of protons which scales any interaction of magnetic field gradients and position of an isochromat. This principle underlies diffusion weighted imaging and blood flow measurements by MRI Moran [1982], Feinberg et al. [1984], Stejskal and Tanner [1965]. However, it was pointed out first in Muthupillai et al. [1995], Plewes et al. [1995] that this principle can also be employed to image strain waves inside the human body. For a time dependent gradient $\mathbf{G}(t)$ and a time dependent position of an isochromat $\mathbf{x}(t)$ the phase signal can be written as

$$\phi(\tau) = \gamma \int_0^{\tau < T_E} \mathbf{G}(t) \cdot \mathbf{x}'(t) dt. \tag{2.13}$$

In case of an elastic disturbance traveling through the sample the position of the isochromats with equilibrium position $\mathbf{x}$ is described by

$$\mathbf{x}'(t) = \mathbf{x} + \mathbf{u}(\mathbf{x}, t), \tag{2.14}$$

where $\mathbf{u}(\mathbf{x}, t)$ denotes the displacement. In order to obtain only contributions to the phase due to motion, the temporal shape of the motion encoding gradient (MEG) must ensure

$$\phi = \gamma \int_0^{\tau < T_E} \mathbf{G}(t) \cdot \mathbf{x} dt \quad = \quad 0, \tag{2.15}$$

so that no information on the spatial equilibrium position is encoded. For this reason bipolar gradients with zero momentum are used. Then, the acquired phase (2.13) is solely due to moving spins

$$\phi(\tau) = \gamma \int_0^{\tau < T_E} \mathbf{G}(t) \cdot \mathbf{u}(\mathbf{x}, t) dt. \tag{2.16}$$

MEGs commonly used in MRE are trapezoidal (see also figure 2.3) or sinusoidal. Assuming a linearly polarized wave $\mathbf{u}(x_1, t) = \mathbf{u}_0 \cos(kx_1 - \omega t + \theta_{rel})$, which is induced by an externally applied source vibrating at ω_{ext}, one obtains in case of N cycles of trapezoidal MEGs with duration equal to $2\pi/\omega_{ext}$ (neglecting ramp time)

$$\begin{aligned} \phi(\tau) = \gamma N(\mathbf{G} \cdot \mathbf{u}_0) & \left[\int_0^{\pi/\omega_{ext}} \cos(kx_1 - \omega_{ext} t + \theta_{rel}) dt \right. \\ & \left. - \int_{\pi/\omega_{ext}}^{2\pi/\omega_{ext}} \cos(kx_1 - \omega_{ext} t + \theta_{rel}) dt \right] \\ = 4\gamma N(\mathbf{G} \cdot \mathbf{u}_0) & \frac{\sin(kx_1 + \theta_{rel})}{\omega_{ext}}. \end{aligned} \tag{2.17}$$

The parameter θ_{rel} is varied during MRE scans by increasing the delay between start of the external vibration and application of the MEG. This allows the stroboscopic acquisition of a time resolved wave field. Since short MEGs ($N \approx 1$) are not frequency-specific, ω_{ext} has not necessarily to be matched with $2\pi/\omega_{ext}$. Though it was here assumed that the angular frequency of the MEG equals the external vibration frequency this need not be the case Rump et al. [2007].

2.2 Elasticity Theory

A deformation is called elastic when a solid body reassumes its original shape after external forces vanish. If the original shape is not resumed the deformation is called plastic. Here, only elastic deformations are considered. In the following section the engineering constants Young modulus E, Poisson's ratio ν and shear modulus μ are introduced by considering axial and shear deformations. Other elastic constants such as the bulk modulus and the Lamé coefficients are related. An elastic material featuring a given symmetry is completely characterized by a distinct number of independent parameters. Henceforth, E, ν and μ are used.

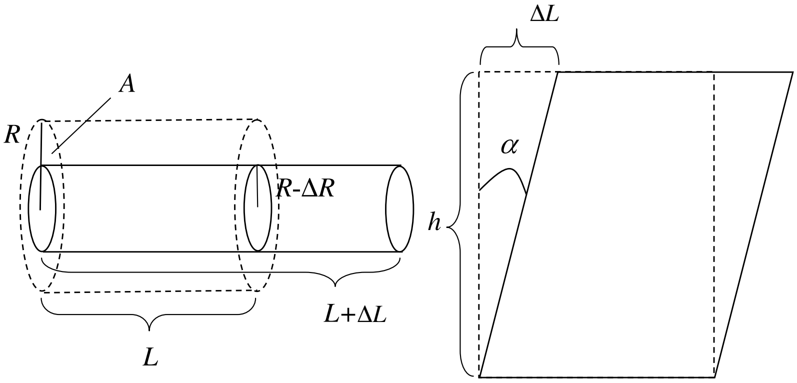

Abbildung 2.4: Basic deformation defining Young's modulus, Poisson's ratio and shear modulus.

2.2.1 Young's Modulus

To increase the length of a rod of initial length L and initial cross section A by an amount $\triangle L$ a force F must be applied . Under the assumption of small $\triangle L$ the force per initial area $\tau = F/A$ is proportional to the relative change in length $\epsilon_L = \triangle L/L$

$$\epsilon_L = \frac{1}{E}\tau. \tag{2.18}$$

This is Hooke's law in case of a continuous deformable rod. The constant of proportionality E is called Young's modulus or modulus of elasticity and its reciprocal value is termed compliance. Its dimension is $[E] = N/m^2 = Pa$. A deformation described by (2.18) is called a simple elongation or compression depending on the sign of $\triangle L$.

2.2.2 Poisson's Ratio

As the length of the rod increases its radius R decreases by $\triangle R$. If one defines $\epsilon_R = \triangle R/R$, the ratio of relative change

$$\nu = -\frac{\epsilon_R}{\epsilon_L} \tag{2.19}$$

is called Poisson's ratio. It is dimensionless. By looking at the relative change $\triangle V/V$ of volume one finds that Poisson's ratio is related to compressibility $\kappa = -1/V(\partial V/\partial p)$ by

$$\kappa = \frac{3}{E}(1-2\nu), \tag{2.20}$$

where the factor of three stems from the contributions from simple elongation into the three coordinate directions. From (2.20) it is readily seen that perfect incompressibility ($\kappa = 0$) implies $\nu = 1/2$ or an infinitely large Young's modulus E. The first case corresponds to material that can be elongated or jolted with no change in its volume, while in the second case the material is resistant to any such deformation. On the other hand, a perfectly compressible medium would not change its radius under simple elongation, i.e. $\triangle R = 0$, and hence according to (2.19) $\nu = 0$. However, there are certain types of materials for which the radius increases under elongation, i.e. $\triangle R < 0$, resulting a negative ν with the lowest possible value -1. Hence one has

$$\nu \in \left[-1, \frac{1}{2}\right]. \tag{2.21}$$

2.2.3 Shear Modulus

A deformation that does not change the volume is called a shear deformation. Consider a cube with height h of elastic material. If the top surface is displaced by $\triangle L$ with respect to the bottom then the force per unit area for small $\triangle L$ can be expressed by

$$\tau = \mu \tan \frac{\triangle L}{h} \approx \mu\alpha, \tag{2.22}$$

where $\alpha = \triangle L/h$. Relation (2.22) is also in the form of Hooke's law.

2.2.4 Tensor Description: Generalized Hooke's Law

Within the theory of continuum mechanics a deformation is described by dividing a given body into volume elements, that are thought to be large compared to the microscopic scale but small compared to the deformation. Their deviation from equilibrium position is called displacement and can be defined as the vector field

$$\mathbf{u}(\mathbf{x}, t) = \mathbf{x}'(t) - \mathbf{x}, \tag{2.23}$$

($[u_i] = m$) where $\mathbf{x}$ is the equilibrium position and $\mathbf{x}'$ the position after deformation. The change in distance between two small volume elements that were at a distance dl in equilibrium can be expressed as

$$dl'^2 = dl^2 + \epsilon_{kl} dx_k dx_l \tag{2.24}$$

where

$$\epsilon_{kl} = \frac{1}{2}\left(\partial_l u_k + \partial_k u_l\right) \tag{2.25}$$

is the dimensionless symmetric rank two strain tensor for small $\partial_j u_i$. Henceforth, Einstein's summation convention is implied if not mentioned otherwise. Since the trace of the strain tensor is the divergence of the displacement field,

$$\epsilon_{jj} = \nabla \cdot \mathbf{u}, \tag{2.26}$$

it represents the local change in volume due to the deformation. For this reason the diagonal elements of the strain tensor are used for the general definition of Poisson's ratios (no summation)

$$\nu_{ij} = -\frac{\epsilon_{jj}}{\epsilon_{ii}} \tag{2.27}$$

The deformation of a body results in internal forces, called stresses described by the symmetric rank two stress tensor **œ** ($[\sigma_{ij}] = Pa$). The relationship between stress tensor and strain tensor

$$\sigma_{ij} = C_{ijkl}\epsilon_{kl} \tag{2.28}$$

is called generalized Hooke's law. The rank four tensor **C** is called elasticity tensor ($[C_{ijkl}] = Pa$). The stress tensor defines vectors of surface traction or traction by

$$\tau_i = \sigma_{ij}n_j, \tag{2.29}$$

where the n_j are the components of the normal vector of the surface. The inverse of the elasticity tensor $\mathbf{S} = \mathbf{C}^{-1}$ is called compliance tensor and

$$\epsilon_{ij} = S_{ijkl}\sigma_{kl} \tag{2.30}$$

is also called Hooke's law ($[S_{ijkl}] = m^2/N$). Both rank four tensors have the following symmetry properties (shown only for **C**)

$$C_{ijkl} = C_{jikl} = C_{ijlk} = C_{klij}. \tag{2.31}$$

Since the elasticity tensor is of rank four, Hooke's law (2.28) cannot in general be written as a matrix align. Due to the symmetry properties, which reduce the number of independent moduli to 21, the elasticity tensor can be expressed as a symmetric 6×6 matrix using the reduced or Voigt's notation

$$\begin{aligned} &11 \leftrightarrow 1, \qquad && 22 \leftrightarrow 2, \qquad && 33 \leftrightarrow 3, \\ &23 \leftrightarrow 4, && 13 \leftrightarrow 5, && 12 \leftrightarrow 6. \end{aligned} \tag{2.32}$$

Using this notation Hooke's law can be written as

$$\begin{pmatrix} \sigma_{11} \\ \sigma_{22} \\ \sigma_{33} \\ \sigma_{23} \\ \sigma_{13} \\ \sigma_{12} \end{pmatrix} = \begin{pmatrix} C_{11} & C_{12} & C_{13} & C_{14} & C_{15} & C_{16} \\ C_{12} & C_{22} & C_{23} & C_{24} & C_{25} & C_{26} \\ C_{13} & C_{23} & C_{33} & C_{34} & C_{35} & C_{36} \\ C_{14} & C_{24} & C_{34} & C_{44} & C_{45} & C_{46} \\ C_{15} & C_{25} & C_{35} & C_{45} & C_{55} & C_{56} \\ C_{16} & C_{26} & C_{36} & C_{46} & C_{56} & C_{66} \end{pmatrix} \begin{pmatrix} \epsilon_{11} \\ \epsilon_{22} \\ \epsilon_{33} \\ 2\epsilon_{23} \\ 2\epsilon_{13} \\ 2\epsilon_{12} \end{pmatrix}. \tag{2.33}$$

Isotropy

The elastic behavior of an isotropic medium is completely characterized by two independent elastic constants, e.g. E and ν or μ, respectively. The corresponding compliance tensor reads in Voigt notation

$$\mathbf{S} = \begin{pmatrix} 1/E & -\nu/E & -\nu/E & 0 & 0 & 0 \\ -\nu/E & 1/E & -\nu/E & 0 & 0 & 0 \\ -\nu/E & -\nu/E & 1/E & 0 & 0 & 0 \\ 0 & 0 & 0 & 1/\mu & 0 & 0 \\ 0 & 0 & 0 & 0 & 1/\mu & 0 \\ 0 & 0 & 0 & 0 & 0 & 1/\mu \end{pmatrix} \tag{2.34}$$

with $\mu = E/2/(1+\nu)$. The components of the elasticity tensor are determined by the inverse of (2.34) as

$$\begin{aligned} C_{11} = C_{22} = C_{33} &= \frac{E(1-\nu)}{(1+\nu)(1-2\nu)}, \\ C_{12} = C_{13} = C_{23} &= \frac{E\nu}{(1+\nu)(1-2\nu)} \qquad \text{and} \\ C_{44} = C_{55} = C_{66} &= \mu. \end{aligned} \tag{2.35}$$

All other moduli are zero.

Transverse Isotropy

An elastic material with transverse isotropy is described by five elastic constants. Here the engineering constants $E_1, E_3, \nu_{31}, \nu_{21}$ and μ_{13} are chosen. The material features a plane of symmetry and perpendicular to it a plane of isotropy (see figure 2.5). For this reason transverse isotropy is suited for describing structures that consist of parallel fibers such as muscle. The compliance tensor for such kind of material reads

$$\mathbf{S} = \begin{pmatrix} 1/E_1 & -\nu_{21}/E_1 & -\nu_{31}/E_3 & 0 & 0 & 0 \\ -\nu_{21}/E_1 & 1/E_1 & -\nu_{31}/E_3 & 0 & 0 & 0 \\ -\nu_{13}/E_1 & -\nu_{13}/E_1 & 1/E_3 & 0 & 0 & 0 \\ 0 & 0 & 0 & 1/\mu_{13} & 0 & 0 \\ 0 & 0 & 0 & 0 & 1/\mu_{13} & 0 \\ 0 & 0 & 0 & 0 & 0 & 1/\mu_{12} \end{pmatrix}, \tag{2.36}$$

where due to symmetry of $\mathbf{S}$, $\nu_{13} = \nu_{31}E_1/E_3$. The shear modulus in the plane of isotropy μ_{12} is not independent and is given by

$$\mu_{12} = \frac{C_{11} - C_{12}}{2}. \tag{2.37}$$

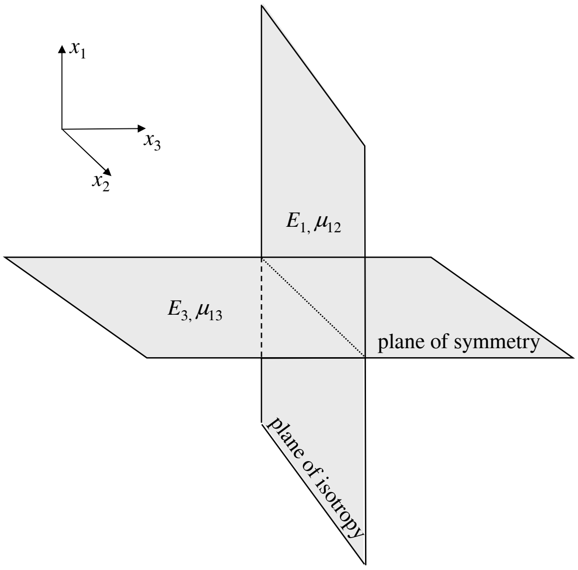

Abbildung 2.5: A transverse isotropic material features two different Young's moduli ($E_1 = E_2, E_3$) and two different shear moduli ($\mu_{23} = \mu_{13}, \mu_{12}$).

The corresponding moduli are

$$\begin{aligned}
C_{11} = C_{22} &= \frac{E_1}{1+\nu_{21}} \frac{1-\nu_{31}^2 E_1/E_3}{D} \\
C_{33} &= \frac{(1-\nu_{21})E_3}{D} \\
C_{12} &= \frac{E_1}{1+\nu_{21}} \frac{\nu_{21}+\nu_{31}^2 E_1/E_3}{D} \\
C_{13} = C_{23} &= \frac{E_1 \nu_{31}}{D} \\
C_{44} = C_{55} &= \mu_{13} \\
C_{66} &= \mu_{12}
\end{aligned} \tag{2.38}$$

(2.39)

with

$$D = 1 - \nu_{21} - 2\nu_{31}^2 \frac{E_1}{E_3}$$

Transverse Isotropy: Plane Stress

A situation in which stresses occur solely in a single plane is called plane stress. A plane stress-scenario of the x_1x_3-plane requires that $\sigma_{22} = \sigma_{23} = \sigma_{12} = 0$. Moreover, since $\sigma_{23} = \sigma_{12} = 0$ one finds that also $\epsilon_{23} = \epsilon_{12} = 0$. Hooke's law is then reduced to

$$\begin{pmatrix} \epsilon_{11} \\ \epsilon_{33} \\ 2\epsilon_{13} \end{pmatrix} = \begin{pmatrix} 1/E_1 & -\nu_{31}/E_3 & 0 \\ -\nu_{13}/E_1 & 1/E_3 & 0 \\ 0 & 0 & 1/\mu_{13} \end{pmatrix} \begin{pmatrix} \sigma_{11} \\ \sigma_{33} \\ \sigma_{13} \end{pmatrix}. \tag{2.40}$$

Because of symmetry $\nu_{13} = \nu_{31} E_1 / E_3$. In case of incompressibility $\nu_{31} = 1/2$. Hence the components of the elasticity tensor $\mathbf{C} = \mathbf{S}^{-1}$ are

$$\begin{aligned} C_{11} &= \frac{4E_1E_3}{4E_3 - E_1}, \\ C_{22} &= \frac{4E_3^2}{4E_3 - E_1}, \\ C_{12} &= \frac{2E_1E_3}{4E_3 - E_1} \end{aligned} \tag{2.41}$$

and $C_{21} = C_{12}$ and $C_{33} = \mu_{13}$.

2.3 Linear Elastic Waves

In MRE elastic waves are used to remotely "palpate"tissue inside the human body. In general, the aligns describing the temporal evolution of displacement fields are nonlinear. However, under the assumption that the deformations are small the theory can be linearized. In the following the background on linear wave propagation required for evaluating MRE wave data is presented.

2.3.1 General Equations of Motion

The propagation of elastic waves in general is described by the align of motion

$$\rho \ddot{u}_i - \partial_j \sigma_{ij} = f_i(\mathbf{x}, t), \tag{2.42}$$

where $u_i = u_i(\mathbf{x}, t)$ is the i-th component of displacement ($[u_i] = m$) and $f_i(\mathbf{x}, t)$ are the components of a body force ($[f_i] = N/m^3$). The Equations of Motion in an anisotropic medium is obtained by inserting Hooke's law (2.28) into (2.42) and using the definition of strain (2.25)

$$\rho \ddot{u}_i - \partial_j \left[C_{ijkl}(\mathbf{x}) \partial_k u_l \right] = f_i(\mathbf{x}, t). \tag{2.43}$$

This is a set of three coupled linear partial differential aligns of second order both in time and space. Their unique solution requires knowledge of boundary conditions and initial conditions. The boundary can be the surface of the deformed body or a surface/interface of discontinuity of $\mathbf{C}$ within the considered region. If the surface is called S, boundary conditions are

1. Displacement boundary conditions: $\mathbf{u}$ is prescribed on S, e.g. $\mathbf{u} = \mathbf{0}$ corresponds to a clamped surface.

2. Traction boundary conditions: $\boldsymbol{\o}$ is prescribed on S, e.g. if $\boldsymbol{\o} = \mathbf{0}$ the surface is traction free.

3. Mixed boundary conditions: S is divided, e.g. $S = S_1 \cup S_2$, with $S_1 \cap S_2 = 0$, and on S_1 and S_2 either the displacement or the traction is prescribed.

Particularly useful in MRE are non-reflecting boundary condition according to Sommerfeld

$$\partial_n u = iku, \tag{2.44}$$

where now ∂_n denotes the normal derivative at the boundary. The meaning of this boundary condition is that only outgoing plane waves exist at the boundary. Since in MRE most measurements are performed after a vibrational harmonic steady state is established, the align of motion relevant in MRE is the temporal Fourier transform of (2.43)

$$\rho\omega^2 \hat{u}_i + \partial_j \left[C_{ijkl}(\mathbf{x})\partial_k \hat{u}_l\right] = 0, \tag{2.45}$$

where $\hat{u}_i = \hat{u}_i(\mathbf{x}, \omega)$. In the following it will be assumed that elasticity is locally constant. Under this assumption the displacement field satisfies locally the align of motion

$$\rho\omega^2 \hat{u}_i + C_{ijkl}(\mathbf{x})\partial_j \partial_k \hat{u}_l = 0. \tag{2.46}$$

This assumption simplifies the inverse problem in MRE to a purely algebraic inversion.

2.3.2 Plane Wave Modes in Anisotropic Media

There is no closed form solution to (2.46) neither for anisotropy nor for a general geometry including boundary conditions. Therefore, an important tool is provided by plane wave modes, which propagate in the bulk of a material featuring elastic anisotropy. Consider a plane wave

$$u_i = u_{0i} e^{i\mathbf{k}\cdot\mathbf{x}}, \tag{2.47}$$

where the u_{i0} are constants determining the initial polarization of the wave and $\mathbf{k}$ is the wave vector with length $k = \omega/c$, where c is the phase velocity of the wave. Inserting (2.47) into (2.46) one obtains

$$\left(c_{ijkl} k_j k_k - \omega^2 \delta_{il}\right) u_{0i} = 0. \tag{2.48}$$

Here, δ_{il} is the Kronecker delta and $c_{ijkl} = C_{ijkl}/\rho$ ($[c_{ijkl}] = m^2/s^2$). Nontrivial solutions (for which at least one $u_{0i} \neq 0$) for the components u_i exist only for angular frequencies

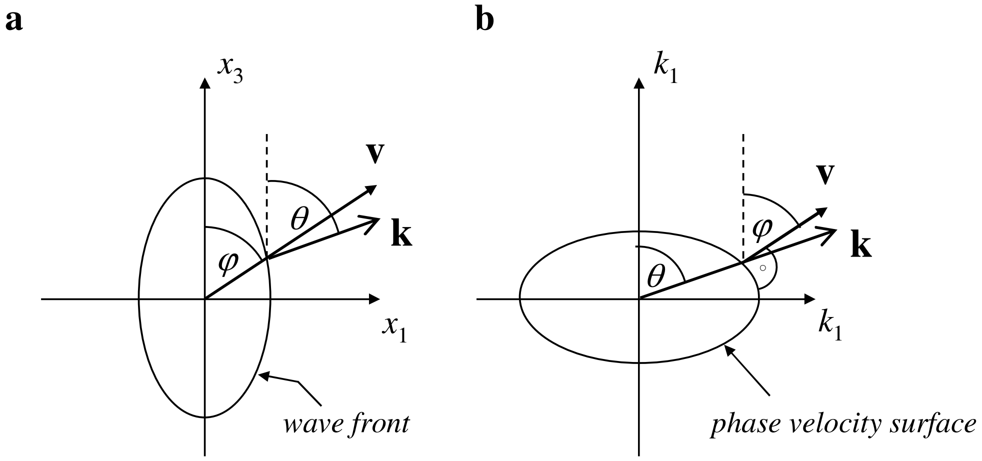

Abbildung 2.6: Schematic 2D illustration of the directional relationship between group velocity **v** and wave vector **k** in the case of anisotropy. a: If waves emanate from a point source, their group velocity determines the wave front. b: In *k*-space, the inherent frequencies of a wave field are shown in relation to the phase velocity. Note: **k** and **v** are only parallel along the 1-direction and the 3-direction of **x** and **k**. This is fundamentally different from isotropic elasticity.

ω, that satisfy the characteristic align

$$\det\left(c_{ijkl}k_j k_k - \omega^2 \delta_{il}\right) = 0. \tag{2.49}$$

This is the eigenvalue align of the Christoffel tensor

$$\Gamma_{il} = c_{ijkl}k_j k_k. \tag{2.50}$$

align (2.49) is of order d in ω^2, where d is the spatial dimension. Consequently, in 3D exist three solutions called modes. These modes are characterized by the relative orientations of **k** and their vector of polarization $\mathbf{u}_0$ as quasi-transverse and quasi-longitudinal. The solutions are functions of the wave vector depending parametrically on the moduli that define surfaces of constant angular frequency. By dividing (2.49) through $|\mathbf{k}|$ one obtains a corresponding align, whose solutions are surfaces of constant phase velocity. Although these surfaces are given in **k**-space or wave normal space, their symmetry properties are maintained in position space. This makes them particularly useful for analyzing waveforms. In an anisotropic medium the phase speed depends on the direction of **k**. There, the direction of energy transport is given by the group velocity

$$\mathbf{v} = \nabla_{\mathbf{k}}\omega(\mathbf{k}), \tag{2.51}$$

where $\nabla_{\mathbf{k}}$ denotes the gradient with respect to the wave vector $\mathbf{k}$. The direction of $\mathbf{v}$ in general differs from the direction of $\mathbf{k}$. Figure 2.6 shows a sketch of the phase velocity surface and wave front projected onto the x_1x_3-plane that is considered to be the image plane in the MRE experiments. Here, two angles θ and φ describe the directions of $\mathbf{k}$ and $\mathbf{v}$, respectively.

2.3.3 Equations of Motion: Isotropy

The Equations of Motion for the displacement field in an isotropic medium is obtained by using (2.33) together with (2.35) and inserting the resulting expressions for the stress into (2.42)

$$\rho\ddot{\mathbf{u}} - c_s\triangle\mathbf{u} - \left(c_p^2 - c_s^2\right)\nabla\left(\nabla\cdot\mathbf{u}\right) = \mathbf{0}, \tag{2.52}$$

where ∇ represents the Nabla operator and $\triangle$ is the Laplace operator. The parameters c_s and c_p are

$$c_s = \sqrt{\frac{\mu}{\rho}} \qquad \text{and} \qquad c_p = \sqrt{\frac{E}{2(1+\nu)(1-2\nu)}}. \tag{2.53}$$

align (2.52) may be separated into two ordinary wave aligns Landau and Lifshitz [1986] by taking note that the total wave field is the sum of shear field and pressure field $\mathbf{u}(\mathbf{x},t) = \mathbf{u}^{(s)}(\mathbf{x},t) + \mathbf{u}^{(p)}(\mathbf{x},t)$ with

$$\nabla\cdot\mathbf{u}^{(s)} = 0, \tag{2.54}$$

and

$$\nabla\times\mathbf{u}^{(p)} = \mathbf{0}, \tag{2.55}$$

i.e. the shear field is volume preserving while the pressure field has no vortices. Under the assumption of harmonic time dependence and using the properties (2.54) and (2.55), (2.52) yields a separate Helmholtz align for each of the displacement components

$$\triangle u_i^{(s)} + k_s^2 u_i^{(s)} = 0 \qquad \text{with} \quad k_s = \frac{\omega}{c_s}, \tag{2.56}$$

and

$$\triangle u_i^{(p)} + k_p^2 u_i^{(p)} = 0 \qquad \text{with} \quad k_p = \frac{\omega}{c_p}. \tag{2.57}$$

From (2.56) and (2.57) it is readily seen that c_s and c_p are the phase speeds of shear waves and pressure waves, respectively. The inverse problem in MRE is to determine either c_s or c_s and c_p from the measured displacement field. The density ρ of soft tissue is assumed to be constant. Due to their large water content most human soft tissues are almost incompressible Fung [1993]. Since in incompressible media the majority of elastic energy is carried by the shear wave Catheline et al. [1999], $u_i^{(p)}$ is of comparably small amplitude and is therefore often neglected. Then, the only remaining align is the Hemholtz align for the shear field (2.56) in combination with (2.54), the latter being automatically satisfied due to the assumptions.

2.3.4 Equations of Motion: Transverse Isotropy

The equations of motion for elastic waves in a material featuring transverse isotropy follows from (2.33), (2.38) and (2.42):

$$\rho\ddot{\mathbf{u}} - \left(\mathbf{A}_1\partial_1^2 + \mathbf{A}_2\partial_2^2 + \mathbf{A}_3\partial_3^2 + \mathbf{A}_4\partial_1\partial_2 + \mathbf{A}_5\partial_1\partial_3 + \mathbf{A}_6\partial_2\partial_3\right)\mathbf{u} = \mathbf{0}, \tag{2.58}$$

with $\mathbf{u} = \mathbf{u}(\mathbf{x}, t)$ and

$$\begin{aligned}
\mathbf{A}_1 &= \begin{pmatrix} C_{11} & 0 & 0 \\ 0 & \mu_{12} & 0 \\ 0 & 0 & \mu_{13} \end{pmatrix} \\
\mathbf{A}_2 &= \begin{pmatrix} \mu_{12} & 0 & 0 \\ 0 & C_{11} & 0 \\ 0 & 0 & \mu_{23} \end{pmatrix}, \\
\mathbf{A}_3 &= \begin{pmatrix} \mu_{13} & 0 & 0 \\ 0 & \mu_{23} & 0 \\ 0 & 0 & C_{33} \end{pmatrix}, \\
\mathbf{A}_4 &= \begin{pmatrix} 0 & C_{12}+\mu_{12} & 0 \\ C_{12}+\mu_{12} & 0 & 0 \\ 0 & 0 & 0 \end{pmatrix}, \\
\mathbf{A}_5 &= \begin{pmatrix} 0 & 0 & C_{13}+\mu_{13} \\ 0 & 0 & 0 \\ C_{13}+\mu_{13} & 0 & 0 \end{pmatrix} \qquad \text{and} \\
\mathbf{A}_6 &= \begin{pmatrix} 0 & 0 & 0 \\ 0 & 0 & C_{23}+\mu_{23} \\ 0 & C_{23}+\mu_{23} & 0 \end{pmatrix}.
\end{aligned} \tag{2.59}$$

A complete separation of pressure and shear waves as in case of isotropy (aligns (2.56) and (2.57)) is not possible for an anisotropic medium.

2.3.5 Equations of Motion: Transverse Isotropy under Plane Stress

The corresponding equations of motion are again determined using (2.33) together with (2.41) and insertion of the resulting expressions for the strain into (2.43) :

$$\rho\ddot{\mathbf{u}} - \mathbf{A}_1\partial_1^2\mathbf{u} - \mathbf{A}_2\partial_3^2\mathbf{u} - \mathbf{A}_3\partial_1\partial_3\mathbf{u} = \mathbf{0}, \tag{2.60}$$

where

$$\mathbf{u} = \begin{bmatrix} u_1(x_1, x_3, t) \\ u_2(x_1, x_3, t) \end{bmatrix} \tag{2.61}$$

and

$$\begin{aligned} \mathbf{A}_1 &= \begin{pmatrix} C_{11} & 0 \\ 0 & \mu_{13} \end{pmatrix}, \\ \mathbf{A}_2 &= \begin{pmatrix} \mu_{13} & 0 \\ 0 & C_{22} \end{pmatrix} \qquad \text{and} \\ \mathbf{A}_3 &= \begin{pmatrix} 0 & C_{11}/2 + \mu_{13} \\ C_{11}/2 + \mu_{13} & 0 \end{pmatrix}. \end{aligned} \tag{2.62}$$

2.3.6 Algebraic Helmholtz Inversion

Algebraic Helmholtz inversion (AHI) simply means solving the Helmholtz align (2.56) for the wave number. The corresponding indices are omitted in the following, since there is now only a shear field. Thus AHI yields

$$k = \left[-\frac{\triangle u_i(\mathbf{x}, \omega)}{u_i(\mathbf{x}, \omega)} \right]^{1/2}. \tag{2.63}$$

The wave number carries no index since it is identical for any component $i = x, y, z$ under the assumptions. Moreover, it has been required in writing (2.63) that the wave is locally a superposition of plane waves featuring the same wave number k and hence k does not depend on the position $\mathbf{x}$ at which (2.63) is evaluated. Under these conditions we have for the phase speed

$$c = \frac{\omega}{k} \tag{2.64}$$

and since then

$$c \equiv c_s, \tag{2.65}$$

the shear modulus is readily obtained by

$$\mu = \rho c^2. \tag{2.66}$$

2.3.7 Elastodynamic Green's Function

The elastodynamic Green's function of an infinite, homogeneous and isotropic medium is the solution to (2.52) with a source or body force term of unit strength

$$f_{jk}(\mathbf{x}, t; \mathbf{x}', t') = \delta_{jk}\delta(\mathbf{x} - \mathbf{x}')\delta(t - t'). \tag{2.67}$$

The Green's function, denoted G_{jk}, is a symmetric rank two tensor, which describes the j-th component of the displacement field at $(\mathbf{x}, t)$ due to a delta pulse at $(\mathbf{x}', t')$ into k-direction. Since the aligns are coupled, such a unidirectional pulse produces shear and pressure waves. Hence, the Green's function is often divided into the parts

$$\begin{aligned} G^{s}_{jk}(\mathbf{x}-\mathbf{x}', t-t') &= -\frac{1}{4\pi\rho c_s^2}\left(\gamma_j\gamma_k - \delta_{jk}\right)\frac{1}{x}\delta(t-t'-x/c_s), \\ G^{p}_{jk}(\mathbf{x}-\mathbf{x}', t-t') &= \frac{1}{4\pi\rho c_p^2}\gamma_j\gamma_k\frac{1}{x}\delta(t-t'-x/c_p), \\ G^{c}_{jk}(\mathbf{x}-\mathbf{x}', t-t') &= \frac{1}{4\pi\rho}\left(3\gamma_j\gamma_k - \delta_{jk}\right)\frac{1}{r^3}\int_{r/c_p}^{r/c_s}\tau''\delta(t-t'-t'')d\tau'', \end{aligned} \tag{2.68}$$

where $\gamma_j = x_j/r$ are the direction cosines. G^s_{jk} and G^p_{jk} describe the shear and pressure far-field, respectively, while G^c_{jk} represents the so-called coupling-field or near-field. It comprises the shear- and pressure near field. The complete Green's function is

$$G_{jk} = G^s_{jk} + G^p_{jk} + G^c_{jk}. \tag{2.69}$$

From the Green's function (2.69) the response of an elastic medium to a point source with arbitrary time dependence is deduced by convolution. Moreover, the Green's function can be used to express the displacement field due to a surface traction **ø**$(\mathbf{x}, t)$ that acts on some region $R \subseteq S$, where S is the surface bounding the given volume. The remainder $S \setminus R$ is assumed to be traction free. The field can then be expressed implicitly as

$$\begin{aligned} u_k(\mathbf{x}, t) = &\int_{-\infty}^{\infty} dt' \int_S\int G_{jk}(\mathbf{x}-\mathbf{x}', t-t')\tau_j(\mathbf{x}', t')dS(\mathbf{x}') \\ &+ \int_{-\infty}^{\infty} dt' \int_S\int u_j(\mathbf{x}', t')C_{jklm}n_k\partial_m G_{lm}(\mathbf{x}-\mathbf{x}', t-t')dS(\mathbf{x}'). \end{aligned} \tag{2.70}$$

The first term in (2.70) can be interpreted in the sense of Huygen's principle. Every surface point with nonzero traction radiates a point source field (2.69). The second term requires knowledge of the displacement field itself at the surface and corresponds to possible surface effects such as Rayleigh waves or head waves. The displacement field due to an extended harmonic source acting in k-direction on a quasi half-space is given for the case of incompressibility, i.e. $c_p >> c_s$. The Green's function (2.69) is expanded by c_s^2 and the small parameter $\epsilon = c_s/c_p$ is introduced. Then, substituting $x' = c_s\tau'/x$, the Green's function (2.69) reads

$$\begin{aligned} G_{jk} = &-\frac{1}{4\pi\rho c_s^2}\left(\gamma_j\gamma_k - \delta_{jk}\right)\delta(t - x/c_s) \\ &+ \frac{\epsilon^2}{4\pi\rho c_s^2}\gamma_j\gamma_k\delta(t - x/c_p) \\ &+ \frac{1}{4\pi\rho c_s^2}(3\gamma_j\gamma_k - \delta_{jk})\frac{1}{x}\int_\epsilon^1 x'\delta(t - x'x/c_s)dx'. \end{aligned} \tag{2.71}$$

The integral yields

$$\int_\epsilon^1 \dots dx' = \frac{c_s^2 t}{x^2}\left[\Theta(t - \epsilon x/c_s) - \Theta(t - x/c_s)\right], \tag{2.72}$$

where Θ is the Heaviside step function. Instead of convoluting the Green's function with a harmonic source time function (2.71) is temporally Fourier transformed and then multiplied by the temporal Fourier transform of a sinusoidal source. The Fourier transform of the first two time dependent terms in (2.71) reads

$$\begin{aligned} g_{jk}(\mathbf{x},\omega) &= \int_{-\infty}^{\infty}\delta(t - x/c_{s,p})e^{i\omega t}dt \\ &= e^{i\omega x/c_{s,p}}. \end{aligned}$$

The time dependent part of the near-field transforms to

$$\int_{\epsilon x/c_s}^{x/c_s} t e^{i\omega t}dt = \frac{1}{\omega^2}\left[\left(1 - \frac{i\omega x}{c_s}\right)e^{i\omega x/c_s} - \left(1 - \frac{i\epsilon\omega x}{c_s}\right)e^{i\epsilon\omega x/c_s}\right].$$

Thus, the Fourier transform of (2.71) reads

$$\begin{aligned} g_{jk}(\mathbf{x},\omega) = &-\frac{1}{4\pi\rho c_s^2}\left(\gamma_j\gamma_k - \delta_{jk}\right)e^{i\omega x/c_s} \\ &+ \frac{\epsilon^2}{4\pi\rho c_s^2}\gamma_j\gamma_k e^{i\epsilon\omega x/c_s} \\ &+ \frac{1}{4\pi\rho\omega^2}(3\gamma_j\gamma_k - \delta_{jk})\frac{1}{x^3}\left[\left(1 - \frac{i\omega x}{c_s}\right)e^{i\omega x/c_s} - \left(1 - \frac{i\epsilon\omega x}{c_s}\right)e^{i\epsilon\omega x/c_s}\right]. \end{aligned} \tag{2.73}$$

Incompressibility corresponds to the case that $\epsilon = 0$. The remaining field then reads

$$\begin{aligned} g_{jk}(\mathbf{x},\omega) = &-\frac{1}{4\pi\rho c_s^2}\left(\gamma_j\gamma_k - \delta_{jk}\right)e^{i\omega x/c_s} \\ &+ \frac{1}{4\pi\rho\omega^2}(3\gamma_j\gamma_k - \delta_{jk})\frac{1}{x^3}\left[\left(1 - \frac{i\omega x}{c_s}\right)e^{i\omega x/c_s} - 1\right]. \end{aligned} \tag{2.74}$$

The first term in (2.74) is the shear far field. The second term comprises two parts of which the oscillatory part represents the shear near field and the non-oscillatory part is the remainder of the pressure field in the limit of incompressibility. There is no propagating pressure field in this approximation. The Fourier transform of a sinusoidal

$$\begin{aligned}\int_{-\infty}^{\infty} \sin \omega t e^{i\Omega t} dt &= \frac{1}{2i}\int_{-\infty}^{\infty}\left(e^{i(\omega+\Omega)} - e^{i(\omega-\Omega)}\right) dt \\ &= i\pi\left[\delta(\omega-\Omega) - \delta(\omega+\Omega)\right], \end{aligned} \tag{2.75}$$

was used with the convention for Fourier transform

$$\int_{-\infty}^{\infty} e^{i(\ldots)t} dt = 2\pi\delta(\ldots). \tag{2.76}$$

A useful quasi half-space model can be derived performing two more steps. First, by an image charge argument Lhemery [1994] the Green's function for the quasi half-space can be written as

$$\begin{aligned}\bar{h}_{jk}(\mathbf{x},\omega) = &-\frac{i}{2\rho c^2}\left(\gamma_j\gamma_k - \delta_{jk}\right)\frac{1}{x}e^{i\omega x/c} \\ &+ \frac{i}{2\rho\omega^2}\left(3\gamma_j\gamma_k - \delta_{jk}\right)\frac{1}{x^3}\left[\left(1-\frac{i\omega x}{c}\right)e^{i\omega x/c} - 1\right]. \end{aligned} \tag{2.77}$$

Second, in the expression for the field due to an extended strain source (2.70) the second part is neglected, resulting in an explicit expression. Assuming that the strain source acts into the j-th direction the field can then be expressed as the tensor

$$u_{jk}(\mathbf{x},\omega) = \int_{-d/2}^{d/2}\int_{-d/2}^{d/2} \bar{h}_{jk}(\mathbf{x}-\mathbf{x}',\omega)dx_2'dx_3', \tag{2.78}$$

where the index k refers to the excitation direction.

2.3.8 Shear Wave Scattering from Interfaces

Scattering occurs when an elastic wave hits a surface at which the elastic properties change discontinuously. Since in general an elastic medium carries both shear and pressure (P) waves, a shear wave can also yield a scattered pressure wave and vice versa. This phenomenon is called mode conversion. If the surface of the elastic discontinuity, henceforth called interface, is a plane, one usually divides the shear wave into a wave whose vector of polarization lies within the interface and a shear wave whose vector of polarization meets with the interface at an angle. The first type is called shear horizontal (SH)-wave while the other is called shear vertical (SV)-wave (figure 2.7). An SH-wave produces only scattered SH-waves, while an SV-wave produces scattered SV- and P-waves. Mathematically, the displacement and the traction across the interface must be continuous for a welded contact interface between two elastic half-spaces. This is in contrast to a non-welded interface for which only the traction across the interface

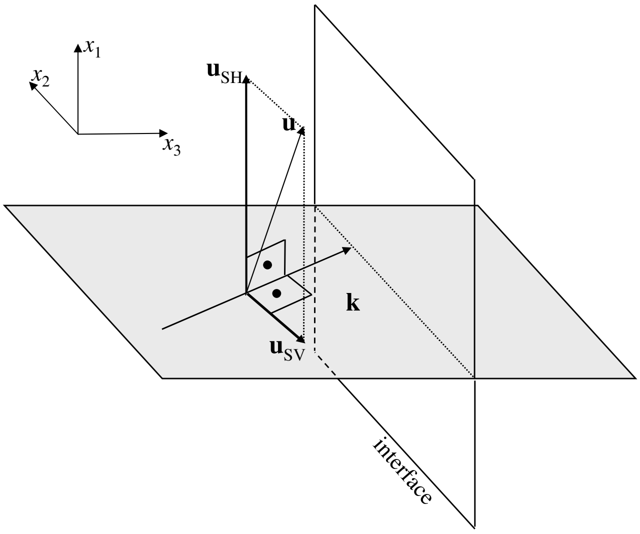

Abbildung 2.7: Classification of a shear wave as a shear horizontal (SH) and shear-vertical(SV) wave in front of a plane elastic discontinuity. The polarization $\mathbf{u}$ of the shear wave is assumed to hit the interface at an angle and the wave vector $\mathbf{k}$ is assumed to lie within a plane perpendicular to the interface. The projection of displacement into this plane yields the SV- wave $\mathbf{u}_{SV}$. Correspondingly, the polarization of the shear horizontal wave is parallel to the interface given by $\mathbf{u}_{SH} = \mathbf{u} - \mathbf{u}_{SV}$.

must be continuous while the displacement is allowed to be discontinuous Schoenberg [1980]. The discontinuity in displacement can be interpreted as slip. If the degree of discontinuity is proportional to the traction across the interface, then this is called linear slip. Cartesian coordinates are chosen such that the interface coincides with the x_2x_3-plane at $x_1 = 0$. A plane wave travels in positive x_1-direction hitting the interface at an angle α_1 inclined by its wave vector $\mathbf{k}$ and the x_1-axis (figure 2.8). The wave vector is assumed to have no component pointing out of the x_1x_2-plane, while the polarization vector is in x_3-direction, i.e. parallel to the interface. Thereby the elastic wave is characterized as an SH-wave. In scattering, it is useful to consider the inverse velocity or slowness instead of the wave vector, since the horizontal component p of the slowness is preserved during the scattering process. The incident, reflected and transmitted waves ($\mathbf{u}_i$, $\mathbf{u}_r$, and $\mathbf{u}_t$, respectively) can be expressed as

$$\mathbf{u}_i = \exp\left[i\omega\left(px_2 + \frac{\cos\alpha_{(1)}}{c_{(1)}}x_1 - t\right)\right]\mathbf{e}_3\,,$$

$$\mathbf{u}_x = R\exp\left[i\omega\left(px_2 - \frac{\cos\alpha_{(1)}}{c_{(1)}}x_1 - t\right)\right]\mathbf{e}_3 \tag{2.79}$$

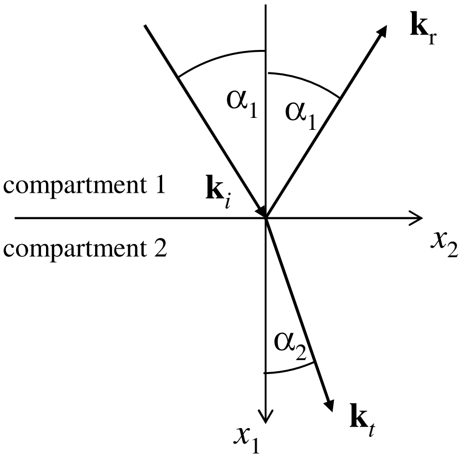

Abbildung 2.8: Sketch of an incident plane SH-wave (displacement is out of plane) with wave vector $\mathbf{k}_i$ hitting a contact surface (at $x_1 = 0$) at an angle α_1. Correspondingly, the wave vectors of the reflected and transmitted waves are labeled $\mathbf{k}_r$ and $\mathbf{k}_t$.

and

$$\mathbf{u}_t = T \exp\left[i\omega\left(px_2 + \frac{\cos\alpha_{(2)}}{c_{(2)}}x_1 - t\right)\right]\mathbf{e}_3, \tag{2.80}$$

where $c_{(1)}$ and $c_{(2)}$ are the shear wave speeds in the upper and the lower compartment, and $\mathbf{e}_3$ denotes the Cartesian unit vector in the corresponding direction (indeces in brackets henceforth refer to the compartment). The reflection and transmission coefficients R and T are calculated by imposing boundary conditions at the elastic interface. Defining

$$\begin{aligned} u^{(1)}\mathbf{e}_3 &= \mathbf{u}_i + \mathbf{u}_r \qquad \text{and} \\ u^{(2)}\mathbf{e}_3 &= \mathbf{u}_t \end{aligned} \tag{2.81}$$

the boundary conditions at $x_1 = 0$ defining a linear slip interface read

$$u_3^{(2)} - u_3^{(1)} = \xi\tau_{13}^{(1,2)} \qquad \text{and} \qquad \tau_{13}^{(2)} - \tau_{13}^{(1)} = 0, \tag{2.82}$$

where ξ is the specific compliance of the interface and

$$\tau_{13}^{(1,2)} = \rho^{(1,2)}c_{(1,2)}^2\frac{\partial u_3^{(1,2)}}{\partial x_1}. \tag{2.83}$$

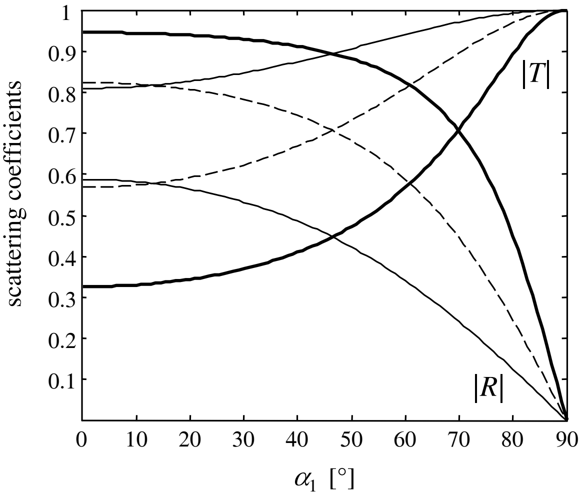

Abbildung 2.9: Angular dependency of the reflection coefficient $|R|$ and the transmission coefficient $|T|$ corresponding to (2.84) at three different frequencies: 50 Hz (thin solid line), 100 Hz (dashed line), 200 Hz (fat sold line). The material was assumed to be identical on both sides of the interface with $c_1 = c_2 = 3.3$ m/s and $\rho_1 = \rho_2 = 1000$ kg/m^3. The specific stiffness of the contact was $\kappa = 0.7$ kPa/mm.

The traction (2.83) in either compartment can be chosen to evaluate the right-hand side of the first align in (2.82). Inserting (2.79) and (2.80) into (2.82) yields for R and T

$$\begin{aligned} R &= \frac{\rho_{(1)}c_{(1)}\cos\alpha_{(1)} - \rho_{(2)}c_{(2)}\cos\alpha_{(2)} - \triangle}{\rho_{(1)}c_{(1)}\cos\alpha_{(1)} + \rho_{(2)}c_{(2)}\cos\alpha_{(2)} - \triangle}, \\ T &= \frac{2\rho_{(1)}c_{(1)}\cos\alpha_{(1)}}{\rho_{(1)}c_{(1)}\cos\alpha_{(1)} + \rho_{(2)}c_{(2)}\cos\alpha_{(2)} - \triangle}, \end{aligned} \tag{2.84}$$

where

$$\triangle = i\xi\omega\rho_{(1)}\rho_{(2)}c_{(1)}c_{(2)}\cos\alpha_{(1)}\cos\alpha_{(2)},$$

and $|T + R| = 1$. Setting $\xi = 0$ reproduces the result for SH-wave scattering from a welded surface Aki and Richards [2002]. The absolute values of the scattering coefficients as a function of the angle of incidence are shown in figure 2.9. The specific compliance is introduced here as a phenomenological parameter quantifying the degree of weldedness between two elastic compartments. A three layer model can provide more physical insight. In case of a plane wave normally incident on the intermediate layer with thickness d and shear wave speed $\bar{c}$, the scattering coefficients read ($c_{(1)} = c_{(2)} = c$)

$$R = \frac{(\bar{c}^2 - c^2)\sin(\omega d/\bar{c})}{2i\bar{c}c\cos(\omega d/\bar{c})) + (\bar{c}^2 + c^2)\sin(\omega d/\bar{c}))} \qquad \text{and}$$

$$T = \frac{2i\bar{c}c}{2i\bar{c}c\cos(\omega d/\bar{c})) + (\bar{c}^2 + c^2)\sin(\omega d/\bar{c}))}. \tag{2.85}$$

In the limit of vanishing layer thickness $d \to 0$ and $\bar{c} << c$ (2.85) reduces to (2.84) with $\alpha = 0$ and

$$\xi = \frac{d}{\rho\bar{c}}, \tag{2.86}$$

where $\bar{c}$ is the shear wave speed inside the intermediate layer. Viscosity η can be included into this model by replacing the real phase speed $\bar{c}$ by its complex counterpart according to the Voigt model

$$\bar{c} = \left(c_0^2 - \frac{i\omega\eta}{\rho}\right), \tag{2.87}$$

where c_0 is the phase speed in the limit $\omega \to 0$.

3 Methods and Materials

3.1 Experiments

MRE experiments were performed on a 1.5 T MR scanner (Sonata, Siemens, Erlangen, Germany). A schematic description of the general experimental setup is shown in figure 3.1. A sinusoidal signal was generated by a wave generator that drove an actuator unit after amplification. The motion sensitive sequence triggered the wave generator. In all experiments a steady state of shear vibration was established by starting measurements after a preset period of external vibration. Wave motion was measured by incremental variation of the relative phase θ_{rel} between motion encoding and external vibration between zero and $2\pi - \omega\Delta t$ (see figure 3.2).

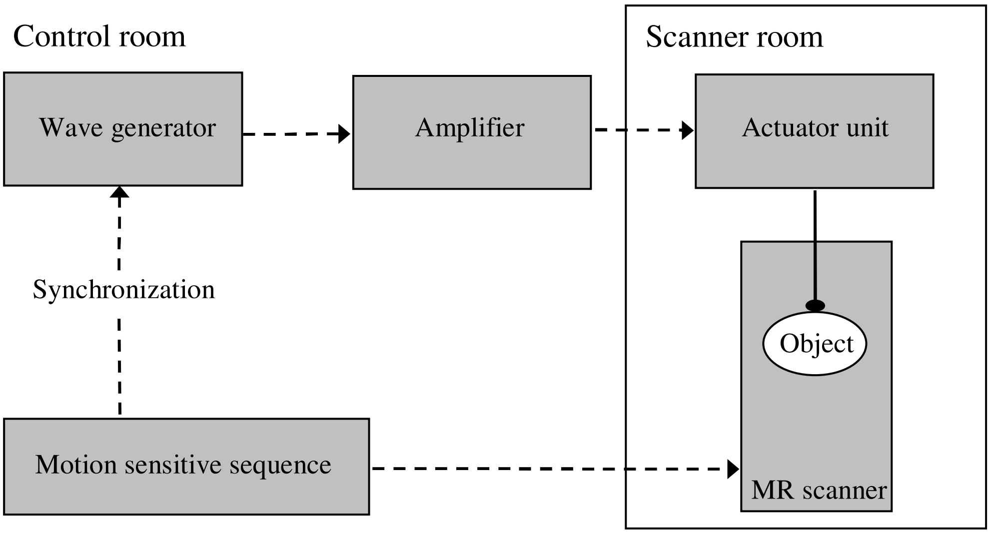

Abbildung 3.1: Principal experimental setup of MRE experiments. Different actuator units and motion sensitive sequences were used in experiments on gel phantoms and in vivo human biceps (for details see text).

3.1.1 MRE Experiments on Homogeneous Gel Phantoms

For investigating the influence of diffraction, discretization and noise on the determined elasticities by AHI an experiment was performed on a gel phantom made of 1 : 5 parts of Wirogel (Bego Inc., Bremen, Germany) : water. A square-plate actuator of $d = 8.5$ cm edge size attached to the top surface of the phantom was vibrated with

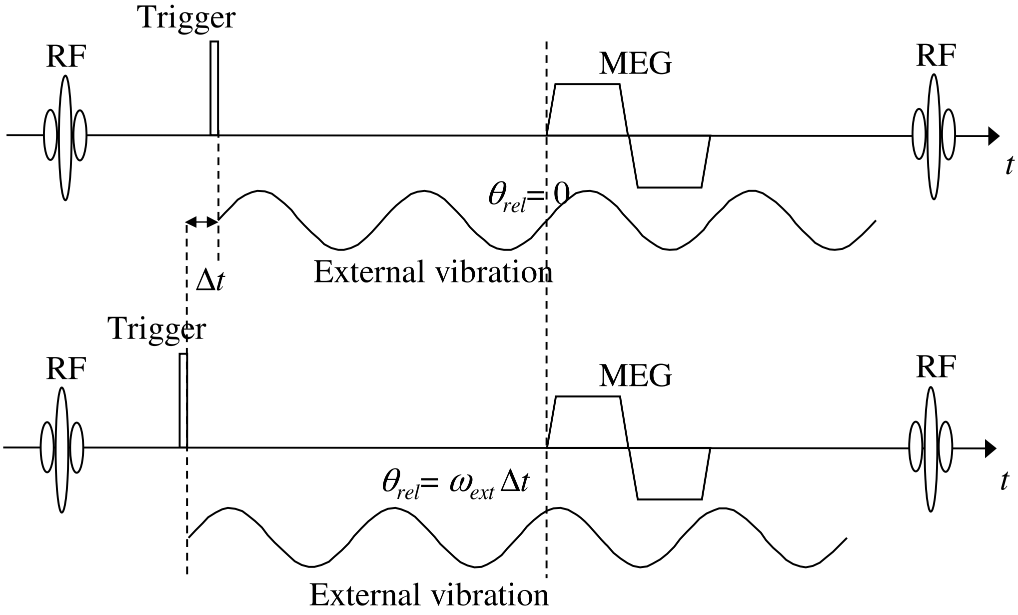

Abbildung 3.2: Steady state wave motion is measured in MRE experiments by shifting the relative phase θ_{rel} defined in equation (2.17) between external vibration and motion encoding.

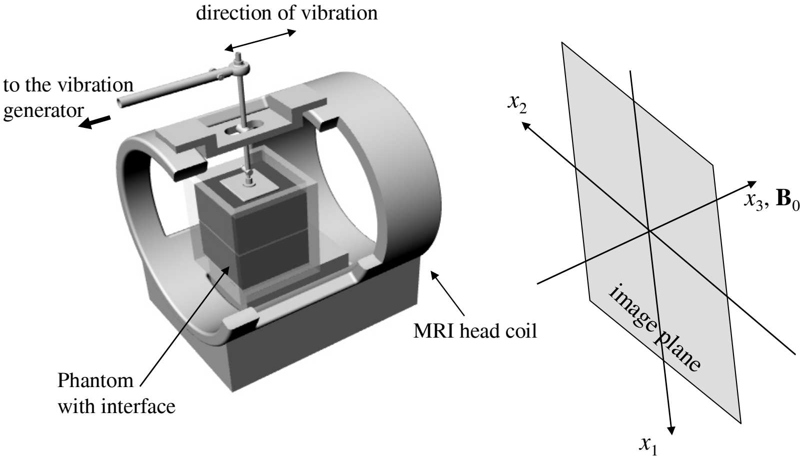

Abbildung 3.3: Experimental setup of MR elastography phantom experiments for studying SH-wave scattering.

an acousto-mechanical actuator at driving frequencies $f = 10$, 15, 20, 25, 30, 35, 40, 50, 60, 70, 80, 90 and 100 Hz for changing the spatial resolution of the waves given in wavelengths per pixel size (λ/a) with $a = 1.5$ mm. The orientation of the image slice, the vibration direction and the direction of motion sensitization were adjusted so that out-of image plane displacement was acquired. For data processing, wave images we-

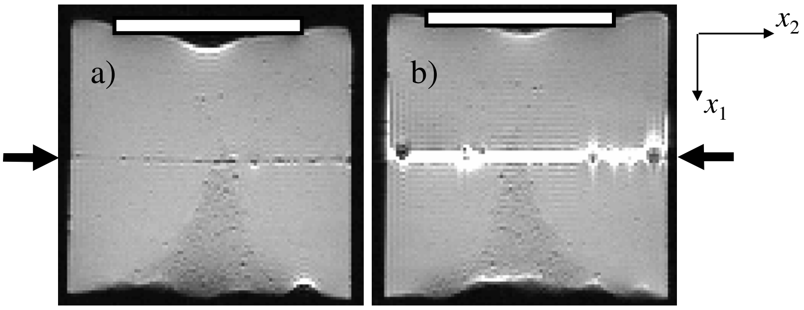

Abbildung 3.4: T_2 weighted MRI magnitude images of a homogeneous phantom that includes an interface which behaves either welded (a) or non-welded (b) in the vibration frequency range of this study. The arrow indicates the position of the interface. In (b) the non-welded interface is well visible as an intense signal of the aqua gel layer (thickness $d \approx 4$ mm), which is caused by a larger T_2 relaxation time than in the surrounding phantom. The position of the transducer plate is demarcated at the upper boundary.

re low-pass filtered using a Butterworth filter ($k_0 = 1000$ m^{-1}) and inverted using the Matlab function (The MathWorks Inc., Natick, MA, USA) AHI described in the appendix 6. The phase speed was derived as a mean quantity from a ROI with $l_x = 10.6$ cm and $l_y = 8.5$ cm edge size.

3.1.2 MRE Experiments on Phantoms with Interface

The experimental setup for studying the scattering of elastic waves from a plane interface is shown in figure 3.3. The setup was chosen so that predominantly scattering of SH- waves normally incident on an interface between two elastically identical halfspaces is considered. In case of an ideally welded contact, no scattering would occur and thus all scattering observed will be due to the linear slip at the interface. The degree of weldedness of the interface was measured by degree of wave studying the scattering as function of frequency. Twenty time steps were recorded that encompass a whole vibration cycle. Shear waves were induced by a transducer plate on top of the phantom (figure 3.3) driven by an acousto-mechanical vibration generator outside of the magnet Klatt et al. [2006]. A 13.5x13.5x14 cm gel phantom (Wirogel[Bego Inc., Bremen, Germany]/water = 1/3) was horizontally cut into two equal-sized compartments. In a first experiment, the two compartments were directly in contact welded by friction. In a second experiment, an approximately 4 mm thick layer of aqua gel (SteriPharm, Berlin, Germany) was introduced to allow both compartments to slip against each other (figure 3.4). In the following both kinds of interfaces are referred to as being the 'welded' and 'non-welded' contact, respectively. The shear wave excitation frequency was 100, 200, 300 and 400 Hz for the phantom with the welded interface and 50, 60, 75, 90, 100, 150, 200, 300 and 400 Hz for the non-welded contact phantom. The shear wave speed

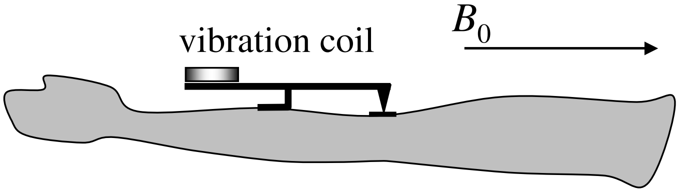

Abbildung 3.5: Schematic image of the electromechanical rocker unit used in MRE experiments on human biceps. Vibrations were introduced into the muscle via the distal tendon.

of the layer was determined in a separate experiment by exciting a container of aqua gel using vibration frequencies of 75, 100 and 150 Hz. A spatio-temporal directional filtering of the 3-dimensional wave data $u_3(x_1, x_2, t)$ was used to separate the incident and transmitted waves (waves with no direction components from bottom to top) from those reflected by the contact interface and the bottom of the container (waves with no direction components from top to bottom). First the data was Fourier-transformed from the position time-domain $(\mathbf{x}, t)$ to the wave number frequency-domain $(\mathbf{k}, \omega)$. The Fourier half-spaces were filtered using two symmetrically mirrored directional filters with $\cos^2$ dependence with respect to the direction of $\mathbf{k}$ Manduca et al. [2003]. The filtered images were inversely Fourier-transformed with respect to $\mathbf{k}$. The obtained wave images $\hat{u}_3(x_1, x_2, \omega)$ were then used to determine $|T|$ and $|R|$ by means of the magnitudes of the amplitudes $(|\hat{u}_3(x_1, x_2, \omega)|)$ of transmitted and reflected waves normalized to the incident wave. Thus, $|\hat{u}_3(x_1, x_2, \omega)|$ was averaged over a small spatial region of $\triangle x_1 = 1.4$ cm and $\triangle x_2 = 4.2$ cm located at the center of the phantom directly above or beneath the interface for determining the scattering coefficients. Further simulation parameters were: $c = 3.3$ m/s, $\rho = 1000$ kg/m^3.

3.1.3 In vivo MRE Experiments on Human Biceps

For studying the elastic anisotropy of human biceps two studies were performed:

1. The plane stress model described in section (2.2.4) was used and
2. a group velocity inversion was developed for elucidating elastic constants from 2D- wave images of skeletal muscle.

For 1. an MRE experiment on an agarose phantom (1.5% in water) and an experiment on a healthy volunteer was conducted. Physical coordinates were assigned to the scanner system with x_1: left → right, x_2: anterior → posterior and x_3: head→ feet. For inducing shear vibrations in x_1-direction in the gel phantom an actuator was designed that allowed a main shear deflection perpendicular to the B_0-field Braun et al. [2003]. For data acquisition a modified EPI sequence was used Braun [2002] (TR: 2 s; TE: 113 ms; FoV: 220 mm; matrix size: 96 × 128). The actuation of the biceps was achieved by a rocker unit with electromotive coil (figure 3.5). The device was mounted at the distal biceps tendon of one volunteer and adjusted to vibrate in x_1-direction. Here the data were acquired using a modified gradient echo imaging sequence (TR: 60 ms; TE = 12 ms; FoV: 320 mm $\times$ 160 mm; matrix size: 256 $\times$ 128). For mechanically exciting both phantom and muscle 7 cycles of 200 Hz oscillations were applied. Motion encoding was achieved by two trapezoidal gradient cycles (200 Hz) applied in x_1-direction. Profiles along the x_3-axis of the wave images were used to determine the shear modulus μ_{13} by the wavelength $\lambda_3 = \sqrt{\mu_{13}/\rho}/f_v$ Dresner et al. [2001].

For 2. a modified balanced steady-state free precession (b-SSFP) sequence with MEG in slice-select direction was used Rump et al. [2005]. The vibration frequency was chosen to be equal to n_v/TR (with integer number of vibration cycles n_v) to avoid image artifacts in the phase-encoding direction. The image acquisition parameters were as follows: FOV, matrix size, slice thickness, and flip angle = 150 mm, 128$\times$128, 5 mm, and 65°, respectively. The elastography parameters vibration frequency, number of vibration cycles, MEG frequency, number of MEG periods, and MEG amplitude were adjusted to be 205 Hz, 3, 205 Hz, 2, and 35 mT/m in phantom studies, and 75-126 Hz, 1, 100-200 Hz, 1, and 35 mT/m in volunteer studies, respectively. Shear vibrations were introduced to the phantom using an electromechanical actuator Braun et al. [2003] whose transducer rod plugged a few millimeters into the gel. In vivo experiments were performed on five healthy male volunteers (mean age = 35 years) using the same actuator as described above (figure 3.5). The direction of transducer motion was approximately in the anterior-posterior (A-P) direction. Motion sensitization was parallel to the principal direction of vibration (x_2) and perpendicular to the image plane (x_1-x_3). Twenty wave images were acquired to produce 10 phase difference wave images $u_2(x_1, x_3, t)$ incrementing θ_{rel} from 0 to 2π. The total measure time was 50 s. The reproducibility of the method was validated on the biceps muscle of volunteer 2. Therefore, eight MRE studies with mechanical vibration frequencies from 75 to 118 Hz were performed on five different days.

3.2 Numerical Methods

Numerical methods were employed to simulate time harmonic shear wave propagation in isotropic and anisotropic materials.

3.2.1 Simulation of Waves due to an Extended Actuator

To study the effect of actuator plate size and relative orientation, motion encoding and predominant actuator motion a quasi half-space model was employed Lhemery [1994]. The plate sizes were varied between 1.5 mm and 100 mm and frequencies were varied according to the experiment described in section 3.1.1. The surface integral (2.78) was numerically evaluated using the adaptive Simpson quadrature method of Matlab at different plate sizes from $d = 1.5$ to 100 mm, driving frequencies from $f = 10$ to 100 Hz and the three configurations shown in figure 3.6. A phase speed of $c = 0.81$ m/s

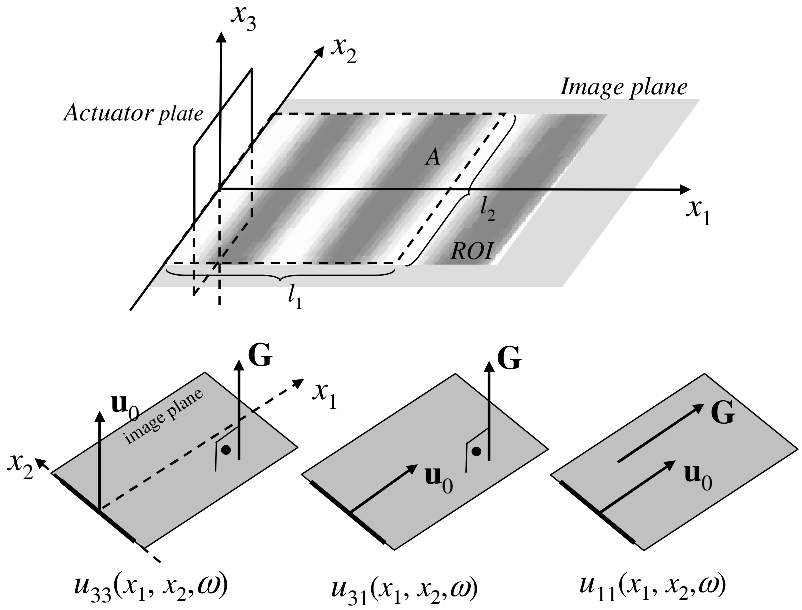

Abbildung 3.6: Three configurations of actuator polarization $\mathbf{u}_0$ and displacement encoding direction $\mathbf{G}$. The first index in u_{jk} refers to the direction of $\mathbf{G}$ and the second index refers to the direction of $\mathbf{u}_0$. The actuator plate is situated at the head of the image plane ($x_1 x_2$) and occupies a region within the $x_2 x_3$-plane.

was used in the simulations similar to the experimental value which was deduced by a 1-D fit of wave profiles. To model noise, separate sets of normally distributed random numbers with variance σ and zero mean were added to the real and imaginary parts of the simulated displacement fields.

3.2.2 Finite Difference Simulations

For simulating elastic waves in a transverse isotropic material under plane stress a method is employed similar to the coupled harmonic oscillator approach in Sack et al. [2002]. A finite difference scheme was developed incorporating non-reflecting boundary conditions defined by equation (2.44) and a local harmonic excitation in x_1-direction at the center of the upper boundary of a 100×200 matrix. Details of the difference scheme and the descriptions of the corresponding Matlab functions are given in the appendix A.

3.2.3 Solution of the Equations of Motion by Fourier Transform

The equations of motion in an anisotropic medium were solved in entire space using the spatial Fourier transform

$$\mathbf{v}(\mathbf{k},t) = \int_{-\infty}^{\infty} \mathbf{u}(\mathbf{x},t) e^{-i\mathbf{k}\cdot\mathbf{x}} d^3 r \tag{3.1}$$

and its inverse

$$\mathbf{u}(\mathbf{x},t) = \frac{1}{(2\pi)^3} \int_{-\infty}^{\infty} \mathbf{v}(\mathbf{k},t) e^{i\mathbf{k}\cdot\mathbf{x}} d^3 k. \tag{3.2}$$

Upon spatial Fourier transform (3.1) the equations of motion become three coupled ordinary differential equations representing three coupled harmonic oscillators

$$\ddot{\mathbf{v}} + \mathbf{\Gamma} \cdot \mathbf{v} = \mathbf{0}, \tag{3.3}$$

where $\mathbf{\Gamma}$ is the symmetric Christoffel tensor (2.50). The system (3.3) was decoupled and solved by changing into the eigensystem of $\mathbf{\Gamma}$. Details are given in the appendix B and the corresponding Matlab functions are described in the appendix A.

4 Results

4.1 Algebraic Helmholtz Inversion

Figure 4.1 shows the results of AHI applied to experimentally measured shear waves at different vibration frequencies in a gel phantom. Although the phantom is homogeneous a spatial variation of phase speed is observed. This spatial variation is apparently smaller at higher vibration frequencies. Figure 4.2(a) shows the phase speed averaged over the image as function of frequency. There, a dispersion is clearly visible that was not expected as the elastic behavior of the gel implies no phase speed dispersion in the investigated frequency range. Manual evaluation of 1D profiles in the direction of the experimental wave propagation yielded a phase speed of $c = 0.81 \pm 0.02$ m/s. This phase speed was used as a gold standard for further analysis. The corresponding wavelengths $\lambda = c/f$ in the frequency range between 10 and 100 Hz are plotted onto the measured wave data at all frequencies as shown in figure 4.2(b). The λ-graph approximately crosses each wave-image section at a one wavelength distance from the actuator. This strongly indicates the absence of any intrinsic dispersion in the gel observable by MRE. The à priori knowledge that the gel is homogeneous in its elastic properties combined with the absence of dispersion in figure 4.2(b), shows that the observed deviation from the expected behavior is caused by the algebraic inversion technique. As AHI is based on the plane wave assumption (see section 2.3.6), the observed phase speed is due to the following points:

1. The probed region, e.g. a gel phantom or an organ, is bounded by vessel walls or connective tissue and hence boundary conditions must in principle be considered.
2. There is a source of waves, i.e. a forced surface traction or a corresponding body force, due to the external actuator. The actuator acts in either shear mode or more often because of efficiency in compressional mode. Depending on its working mode it produces a distinct radiation pattern of elastic waves and the observed wave field depends on the relative orientations of actuator polarization $\mathbf{u}_0$, image plane and motion encoding direction $\mathbf{G}$.
3. The elastic waves radiated by a point source acting in an elastic medium are generally non-plane waves and feature a near-field with different behavior than the far-field. Moreover, the size of the actuator plate determines the diffraction observed.
4. The pressure field is not zero.
5. The measured data is discrete and noisy.

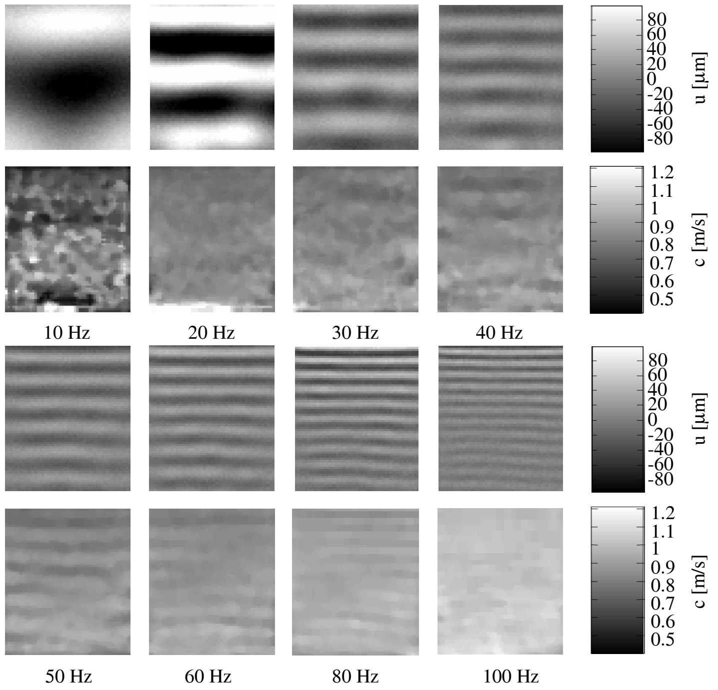

Abbildung 4.1: Elastic waves measured by MRE in a gel phantom and the corresponding spatially resolved phase speed c as determined by application of AHI to the wave data at different vibration frequencies. Experimental setup corresponds to $\hat{u}_3(x_1, x_2, \omega)$ as shown figure 3.6 in the methods section.

As a result, AHI yields only apparent phase speeds displaying spatial variations also in homogeneous materials:

$$c^* = \frac{\omega}{k^*(x_1, x_2, \omega)}. \tag{4.1}$$

In the following, c^* is considered as the averaged apparent phase speed in an area $A = l_1 l_2$ (see figure 3.6). Point 1 plays an important role for enforcing uniqueness of spatially resolved elasticities Barbone and Gokhale [2004]. In the approach made here, boundary effects are diluted by spatial averaging and henceforth neglected. In the following the results of the analysis of points 2 through 5 are presented.

4.1.1 Influence of Noise and Data Discreteness on Phase Speed

The role of point 5 given in the previous section can be analyzed by using a plane wave model. Consider an ideal plane wave

$$u(\mathbf{x}) = e^{i\mathbf{k}\cdot\mathbf{x}}. \tag{4.2}$$

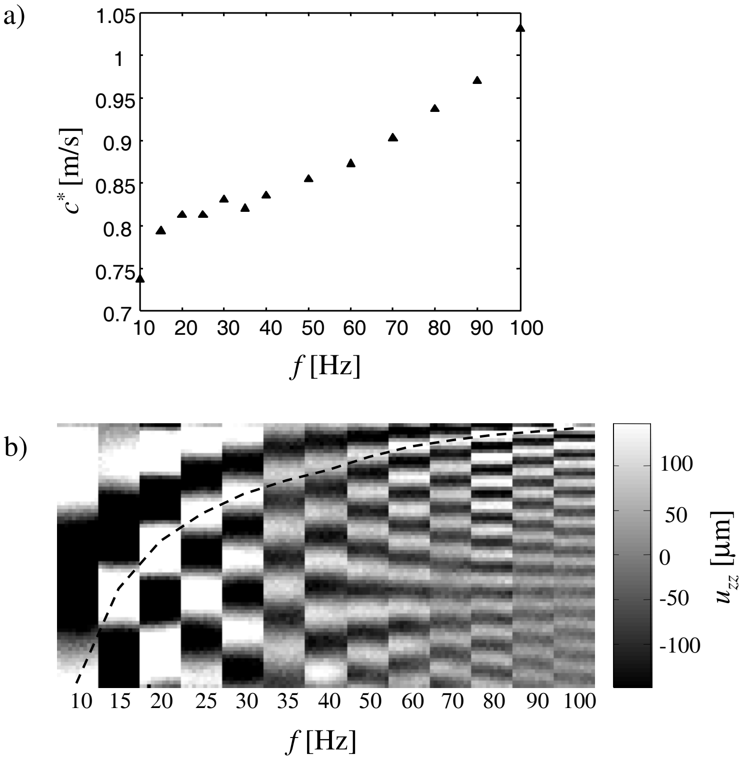

Abbildung 4.2: (a) Apparent phase speed as function of frequency averaged over a ROI as shown in figure 3.6. (b) The function $\lambda = c/f$ plotted onto segments of experimental wave images (dashed line).

Further assume that **k** lies within the image plane (x_1x_2-plane). The positions at which (4.2) is known form a discrete square grid with spacing a. Therefore, the position vector **r** is uniquely defined by two integer indices m, n and $\mathbf{x} = (x_{1,m}, x_{2,n})$ and consequently the plane wave can be labeled $u(\mathbf{x}) = u_{m,n}$. For evaluating the Laplacian in (2.63) a scheme employing repeated central differences is used. Applied to the plane wave (4.2) the scheme yields the approximation

$$\hat{D}u_{m,n} \approx \frac{1}{4a^2}\left(u_{m+2,n} - 2u_{m,n} + u_{m-2,n} + u_{m,n+2} - 2u_{m,n} + u_{m,n-2}\right), \tag{4.3}$$

where $\hat{D}$ is the finite difference approximation to the Laplace operator. Let the wave vector be $\mathbf{k} = (k, 0)$, where $k = \omega/c$. Then AHI together with the approximation scheme (4.3) applied to (4.2) yields for the apparent phase speed

$$c_0^* = \frac{a\omega\sqrt{2}}{\sqrt{1-\cos 2ka}}. \tag{4.4}$$

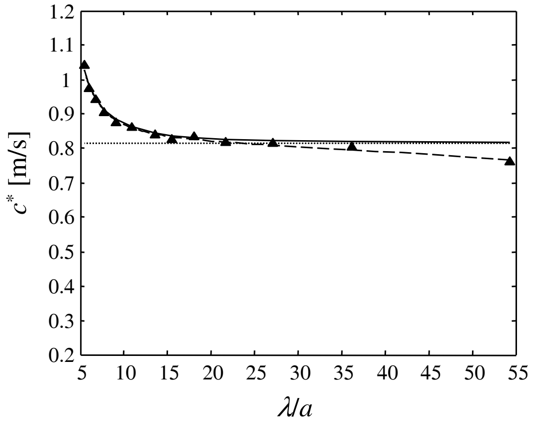

Abbildung 4.3: Apparent phase speed as function of pixel-per-wavelength determined by applying AHI to waves measured in gel and averaging over a ROI as given in methods section (triangles). Phase speed according to (4.4) (straight line). $c^\star$ according to (4.7) with $\sigma = 0.03$ (dashed line). Phase speed determined from one dimensional fit of profiles applied to wave images in figure 2.9 (dotted line).

For including noise the wave (4.2) must be replaced by

$$v'_{m,n} = u_{m,n} + \sigma w_{m,n}, \tag{4.5}$$

where $w_{m,n}$ assumes random values, that are normally distributed with zero mean and σ is the noise-to-signal ratio. The apparent wave number then reads

$$\begin{aligned} k^* &= \left(-\frac{\hat{D}u_{m,n}}{u_{m,n} + \sigma w_{m,n}} - \frac{\sigma \hat{D} w_{m,n}}{u_{m,n} + \sigma w_{m,n}} \right)^{1/2} \\ &= \left(-\frac{\hat{D}u_{m,n}}{u_{m,n}} \frac{1}{1 + \sigma w_{mn}/u_{mn}} - \frac{\hat{D} w_{m,n}}{w_{m,n}} \frac{\sigma}{u_{mn}/w_{mn} + \sigma} \right)^{1/2} \\ &= \left(\frac{k_0^2}{1+\sigma^2} + \frac{k_{noise}^2}{1/\sigma^2 + 1} \right)^{1/2} \\ &\approx \left(\frac{k_0^2}{1+\sigma^2} + \frac{1}{a^2} \frac{1}{1/\sigma^2 + 1} \right)^{1/2}, \end{aligned} \tag{4.6}$$

where $k_0 = \omega / c_0^*$ and the approximation $w_{mn}/u_{mn} \approx \sigma$ is used. The wave number $k_{noise} \approx 1/a$ was found empirically through application of AHI to pure random noise. Expanding $c^* = \omega / k^*$ to first order in σ^2 one obtains for the apparent phase speed

$$c^* \approx \frac{\omega}{k_0} \left[1 - \frac{\sigma^2}{2} \left(\frac{1}{a^2 k_0^2} - 1 \right) \right]. \tag{4.7}$$

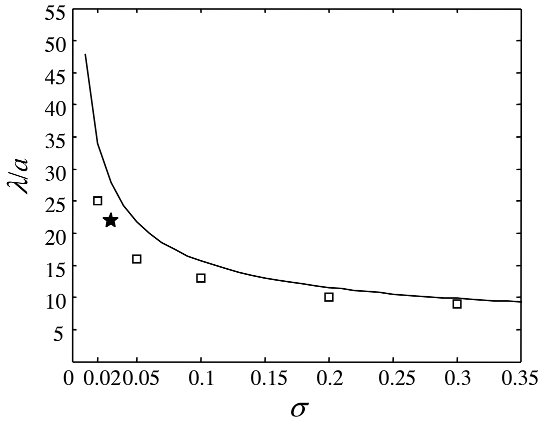

Abbildung 4.4: Number of pixels-per-wavelength required for AHI to yield the correct phase speed as found from numerical solution of equation (4.8) (straight line), AHI applied to simulated plane waves at a given noise level (σ) (squares). AHI applied to wave images measured in a phantom experiment (star)(point of intersection in figure 4.3).

Expression (4.7) gives the dispersion of the apparent phase speed for the plane wave model at low σ. Equating $k = k^*$ (4.6), using (4.4) and substituting $\Omega = ka$ yields the equation

$$\Omega = \left(\frac{1-\cos 2\Omega}{2}\frac{1}{1+\sigma^2} + \frac{1}{1/\sigma^2+1}\right)^{1/2} \tag{4.8}$$

for which no solution in closed form could be found. Noting that $\lambda/a = 2\pi/\Omega$, equation (4.8) enables the numerical calculation of the number of pixels-per-wavelength required for AHI to yield the correct phase speed, i.e. $c^* = c$, depending only on the noise level (figure 4.3). The overshot of c^* at low λ/a values, i.e. at high driving frequencies, is due to discretization, whereas the underestimation of c^* at low driving frequencies is the result of noise. At a resolution of $\lambda/a \approx 24$ the apparent phase speed coincides with the true speed, which is in very good agreement with the approximation (4.7). To further investigate at which optimal resolution an MRE experiment should be run, numerical solutions of equation (4.8) are plotted in figure 4.4 and compared with AHI applied to simulated and experimental plane waves. There, the theory tends to overestimate the optimal λ/a, whereby the observed deviation causes a λ/a error of approximately 5%.

4.1.2 Influence of Diffraction and Pressure Field on Phase Speed

The influence of point 2 to 4 can be analyzed by employing the expression for the displacement field in a quasi half-space given by (2.77). Figure 4.5 shows the results for AHI applied to simulated wave fields produced by actuator plates of various sizes. In ab-

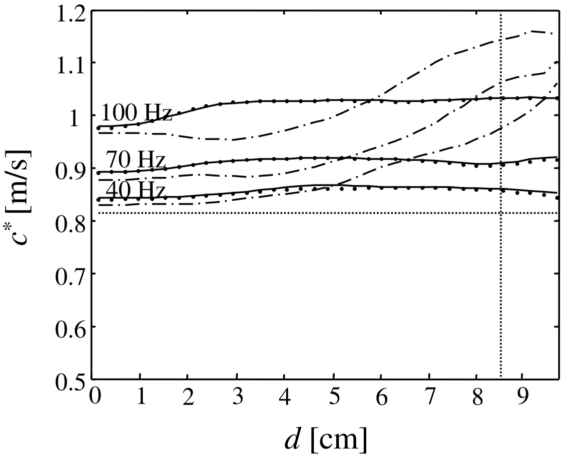

Abbildung 4.5: Apparent phase speed determined by AHI applied to simulated waves according to (2.78) as function of plate size d for the three configurations shown in figure 3.6. Inversion based on $u_{33}(x_1, x_2, \omega)$ (straight line), inversion based on $u_{31}(x_1, x_2, \omega)$ (dots) and inversion based on $u_{11}(x_1, x_2, \omega)$ (dash dotted line). The straight dotted horizontal line shows the true phase speed $c = 0.81$ m/s used in the simulations while the vertical line corresponds to the plate size $d = 8.5$ cm used in the experiment.

sence of noise, AHI based on out-of-plane displacement $u_{33}(x_1, x_2, \omega)$ or $u_{31}(x_1, x_2, \omega)$ is less biased by diffraction than AHI based on $u_{11}(x_1, x_2, \omega)$. In particular, at the plate size used in the experiment, $u_{11}(x_1, x_2, \omega)$ yields strongly overestimated values c^*. However, also out-of-plane displacement modes are influenced by the extension of the driver. A threshold appears when the actuator plate exceeds one wavelength ($d \approx \lambda$), causing c^* to increase by about 10% due to diffraction. For $d > 2\lambda$ variation is only shallow for $u_{33}(x_1, x_2, \omega)$ and $u_{31}(x_1, x_2, \omega)$. The deviation from $c = 0.81$ m/s of all wave modes at $d = 0$ is due to discretization similarly to the data at low λ/a seen in figure 4.3. Figure 4.6(a) shows that the quasi half-space model used predicts an overestimation of c within the entire parameter range if data are noiseless. This effect is the result of wave diffraction due to an extended source. However, if noise is added c^* decreases below 0.81 m/s for $\lambda/a > 20$ as shown in figure 4.6(b). The out-of-plane displacement modes u_{33} and u_{31} resemble the behavior of c^* observed in the experiment and in the plane wave model of figure 4.3. In contrast, the in-plane polarization u_{11} causes a strong deviation of c^* from the plane-wave behavior, although these waves have their optimum resolution at $\lambda/a = 21$, which is similar to c^* deduced from u_{33}. However, the steep slope of c^* of u_{11} near the intersection with c results in greater inaccuracies of c^* than expected for u_{31}, whose shallow slope allows λ/a to be varied between 15 and 30 without exceeding an error of c^* of 5%.

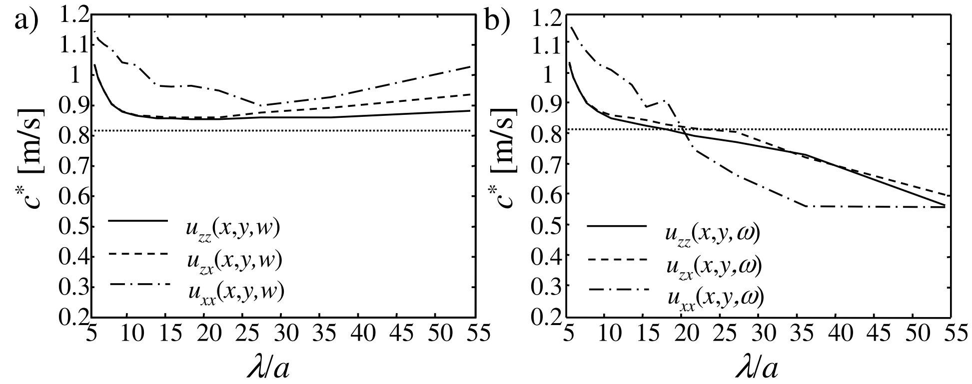

Abbildung 4.6: c^* as function of λ/a for the three configurations shown in figure 3.6. (a) (no noisy data) straight line: inversion based on $u_{33}(x_1, x_2, \omega)$, dashed line: inversion based on $u_{31}(x_1, x_2, \omega)$ and dash dotted line: inversion based on $u_{11}(x_1, x_2, \omega)$. (b) the same as (a) with noise added ($\sigma = 0.1$). Dotted line: phase speed used in the simulations.

4.2 Shear Wave Scattering from a Nonwelded Interface

Figure 4.7 shows SH-waves measured in a gel phantom with interfaces. It is visible that in case of a welded contact at the interface, waves propagate undisturbed through the gel. This was expected since the shear wave speed is the same in both compartments. In contrast, the non-welded interface suppresses the transmission of SH-waves with increasing frequency. This behavior of a non-welded interface enables the determination of the degree of weldedness by MRE by determining transmission and reflection coefficients as function of frequency. Only waves normally incident on the interface are considered corresponding to the experimental setup. At small angles of incidence the cos-terms in (2.84) are approximately one, and if the two compartments are identical, i.e. $c_1 = c_2 = c$ and $\rho_1 = \rho_2 = \rho$, (2.84) is further reduced to

$$\begin{aligned} R &= \frac{-i\xi\omega\rho c}{2 - i\xi\omega\rho c}, \\ T &= \frac{2}{2 - i\xi\omega\rho c}. \end{aligned} \tag{4.9}$$

Since the scattering coefficients R and T are complex, they can be expressed as the product of their absolute value and the corresponding phase factor. For the reflection coefficient R one finds

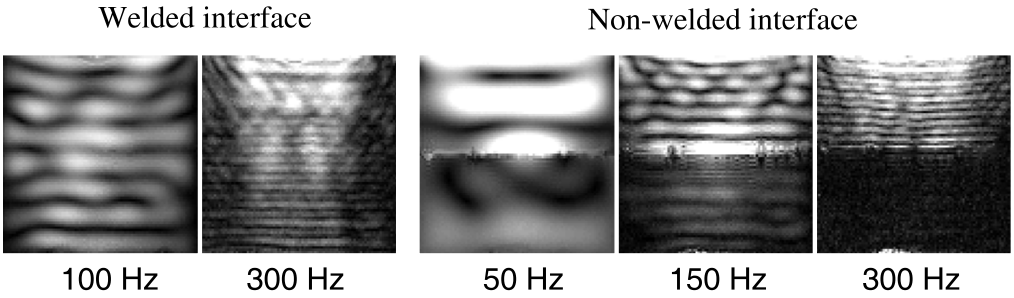

Abbildung 4.7: Magnitude images of SH-waves (displacement out of image plane) due to different vibration frequencies which travel through a gel phantom with either a welded or a non-welded contact interface. In each case the elastic properties above and below the interface are identical.

$$
\begin{aligned}
R &= |R|e^{i\phi_r}\,, \\
\phi_r &= -\frac{2}{\xi\omega\rho c}\,, \\
|R| &= \frac{\xi\omega\rho c}{\sqrt{4+\xi^2\omega^2\rho^2c^2}}\,,
\end{aligned}
\tag{4.10}
$$

and the transmission coefficient is

$$
\begin{aligned}
T &= |T|e^{i\phi_t}\,, \\
\phi_t &= \frac{1}{2}\xi\omega\rho c\,, \\
|T| &= \frac{2}{\sqrt{4+\xi^2\omega^2\rho^2c^2}}\,.
\end{aligned}
\tag{4.11}
$$

If $\epsilon = \xi\omega\rho c$ is introduced as a small dimensionless parameter one finds the asymptotic low non-weldedness or low-frequency behavior ($\epsilon \longrightarrow 0$)

$$
\begin{aligned}
|R| \approx &\quad \frac{1}{2}\epsilon - O(\epsilon^3)\,, \\
|T| \approx &\quad 1 - O(\epsilon^2)\,.
\end{aligned}
\tag{4.12}
$$

for the scattering coefficients. These results show that at very low frequencies, only a transmitted wave exists, having the same amplitude as the incident wave and no change in its phase. The behavior is as if the contact had been welded. On the other

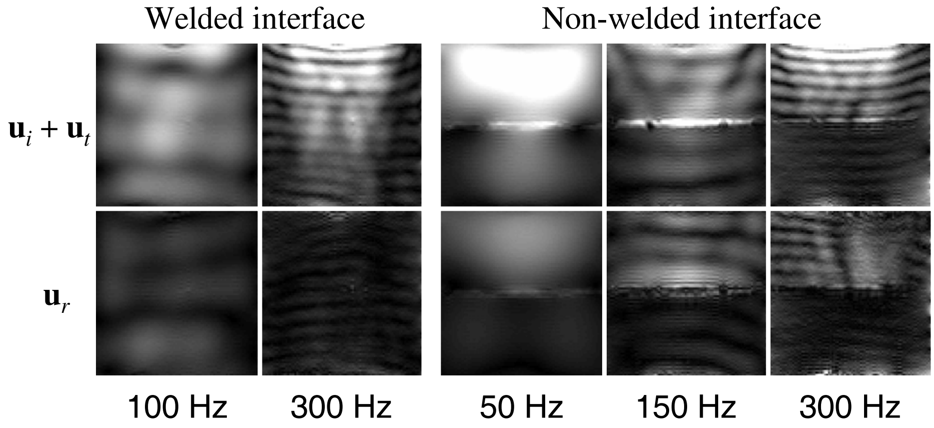

Abbildung 4.8: Magnitude images of SH-waves ($|\hat{u}(x,z,\omega)|$) due to different vibration frequencies (given above the images) which travel through a welded and a non-welded contact surface. The first row shows $|\hat{u}(x,z,\omega)|$ of the originally acquired data. The second and third row show spatiotemporally filtered data, for extracting the downwards or upwards running wave, respectively.

hand, it is apparent that the amplitude of the transmitted wave is suppressed at high frequencies, thus providing a low-pass filter for SH-wave scattering. Moreover, the phase shift is always positive for the transmitted and negative for the reflected wave. Figure 4.8 shows sample images of the wave magnitudes in both phantoms with welded and non-welded interface. Wave speeds of the phantom gel matrix and layer material were determined with 3.3 ± 0.2 m/s and 0.9 ± 0.2 m/s, respectively. The first row in figure 4.8 shows the magnitudes of the superposed incident, transmitted and reflected waves. It can be seen that the welded interface barely influences the wave amplitudes, whereas the non-welded contact acts as a low-pass filter rejecting higher vibration frequencies. This behavior is even better illustrated by the second and third row of figure 4.8. There, the downward- and upward-running waves are separated, yielding amplitudes for the incident and the transmitted waves in the second row and the reflected waves in the bottom row. The amplitudes of the transmitted waves do not significantly change while traveling through the welded interface. In contrast, a drop of wave amplitude beneath the non-welded interface is visible at 300 Hz. The magnitude images of the upward-running waves clearly show reflections at the bottom of the vessel. Such reflections are increasingly suppressed at higher vibration frequencies as a result of the non-welded contact interface and viscosity of the phantom. Figure 4.9 shows the transmission and reflection coefficients as functions of the frequency. The data was fitted to equations (4.11) and (4.10), respectively, using $\kappa = 30$ kPa/mm for the welded contact and 0.7 kPa/mm for the non-welded contact. The upper and lower error margins are given with 50 and 20 kPa/mm for the welded contact and 1.0 and 0.5 kPa/mm for the non-welded interface. These margins do not confine the experimental transmission coefficient of the welded contact. Figure 4.9 shows that in the range of small ϵ given by

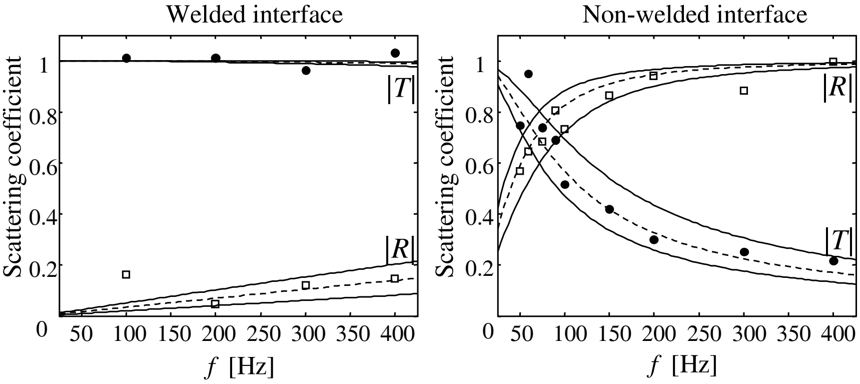

Abbildung 4.9: Scattering coefficients $|R|$ (open squares) and $|T|$ (closed circles) according to equations 4.10 and 4.11 for the welded and the non-welded interface measured by MR elastography experiments. The dashed lines indicate the best match in a least squares sense of the experimental data to the linear slip model, while the solid lines provide error margins.

the welded interface the linear approximation of equations (4.12) is well applicable. $|T|$ shows no significant variation with vibration frequency which increases the tolerance of the fit of κ.

Figure 4.10 shows the scattering coefficients using the three-layer model as given in (2.85). Viscosity was included according to (2.87). The transmission coefficient was fitted by changing c_0 and η in equation (2.85) in a least square minimization routine. Best fit values were $c_0 = 1.7 \pm 0.4$ m/s and $\eta = 3.6 \pm 0.4$ Pa s. The shown reflection coefficient corresponds to these values. Using the fitted c_0 as $\bar{c}$ (representing the limit $f \longrightarrow 0$) and an approximate layer thickness of the intermediate layer of 4 mm allows to recalculate κ from (2.86) with $\kappa(f \longrightarrow 0) = 0.6 \pm 0.2$ kPa/mm. While this value agrees to the linear slip model, c_0 is larger than the experimentally observed shear wave speed of the layer material (0.9 ± 0.2 m/s). This difference increases with frequency as a result of viscosity, which is opposed to the experimental findings where no wave speed dispersion was observed.

4.3 The Shear Modulus in Anisotropic Materials

In the following, the results from the analysis of a 2D and a 3D model of transverse isotropy applied to MRE biceps data are presented. The section starts with the evaluation of the anisotropic wave patterns using a scenario of plane stresses and then proceeds to the evaluation of muscle anisotropy by using the newly developed group velocity inversion (GVI).

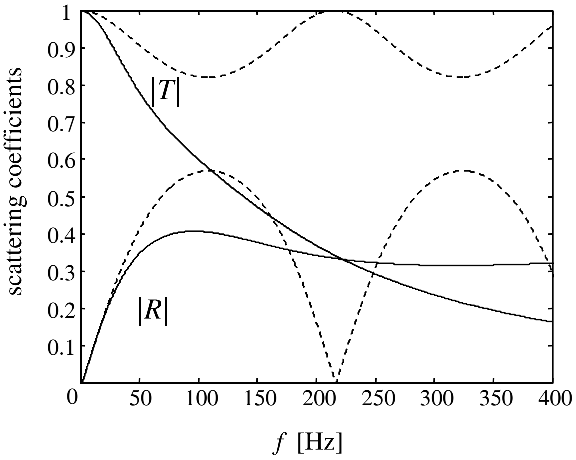

Abbildung 4.10: Scattering coefficients $|R|$ and $|T|$ according to a three- layer model (2.85) without viscosity (dashed lines) and including viscosity (solid lines)

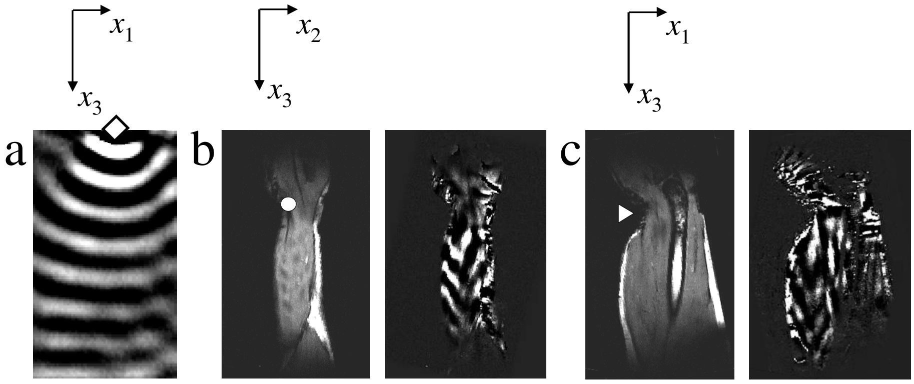

Abbildung 4.11: Experimental shear waves in agarose (a) and skeletal muscle tissue (b) and (c). Harmonic shear excitation (200 Hz) was focally introduced in x_1-direction at positions symbolized by the rhombus, circle and triangle, respectively. The symbols also demarcate the origins of the coordinates. The muscle wave images are shown in sagittal (b) and coronal slice position (c) of the right arm of the same volunteer. On the left-hand side of (b) and (c) the magnitudes MRE images are shown that were used for weightening the phase difference signal with the signal magnitude (right-hand side).

4.3.1 Shear Wave Patterns in Agarose Gel and Biceps Muscle

Figure 4.11 shows waveforms as measured by MRE in isotropic agarose and in human muscle due to a focal source. In agarose the waves emanate in concentric circular waves. This is also expected from the Green's function (2.69). In contrast, they form tapered V-

waves in case of human biceps as a result of the strong anisotropy in muscle tissue.

4.3.2 Analytical Description of Anisotropic Wave Patterns

In this section the experimentally observed V-waves are analyzed using the plane stress scenario described in theory sections 2.2.4 and 2.3.5. For quantifying the experimentally observed V-shaped wave pattern the equations of motion (2.60) are spatially Fourier transformed (3.1). Thereby, the boundary value problem is turned into an initial value problem

$$\rho \frac{\partial^2}{\partial t^2} \begin{pmatrix} \hat{u}_1 \\ \hat{u}_3 \end{pmatrix} + \begin{pmatrix} A_{11} & A_{12} \\ A_{12} & A_{22} \end{pmatrix} \begin{pmatrix} \hat{u}_1 \\ \hat{u}_3 \end{pmatrix} = \begin{pmatrix} 0 \\ 0 \end{pmatrix}, \tag{4.13}$$

where the elements of $\mathbf{A}$ are

$$\begin{aligned} A_{11} &= C_{11} k_1^2 + \mu_{13} k_3^2, \\ A_{12} &= \left(\frac{C_{11}}{2} + \mu_{13} \right) k_1 k_3, \\ A_{22} &= \mu_{13} k_1^2 + C_{33} k_3^2. \end{aligned} \tag{4.14}$$

This set of second-order differential equations describes two coupled harmonic oscillators. The equation for $\hat{u}_1$ is differentiated twice with respect to time in order to obtain a single equation for $\hat{u}_1$, which was the component measured in the MRE experiments as described in the methods section, . Then using the equation for $\hat{u}_3$ one obtains the fourth order differential equation

$$\rho \frac{\partial^4 \hat{u}_1}{\partial t^4} + (A_{11} + A_{22}) \frac{\partial^2 \hat{u}_1}{\partial t^2} + \left(A_{11} A_{22} - A_{12}^2 \right) \hat{u}_1 = 0. \tag{4.15}$$

Assuming a δ-like excitation $u_1(x_1 = 0, x_3 = 0)$ at time $t = 0$ and setting all derivatives up to third order zero, the initial value problem (4.15) is solved by

$$\hat{u}_1 = a_1 \left(e^{i\omega_1 t} + e^{-i\omega_1 t} \right) + a_2 \left(e^{i\omega_2 t} + e^{-i\omega_2 t} \right), \tag{4.16}$$

where

$$\begin{aligned} \omega_{1,2} &= \frac{1}{\sqrt{2\rho}} \sqrt{A_{11} + A_{22} \pm \xi} \qquad \text{and} \\ a_{1,2} &= \pm \frac{A_{11} - A_{22}}{4\xi} + \frac{1}{4}, \\ \xi &= \sqrt{(A_{11} - A_{22})^2 + 2A_{12}^2}. \end{aligned} \tag{4.17}$$

The angular frequencies $\omega_{1,2}$ are the eigenvalues of $\mathbf{A}$. They describe two plane wave modes, a fast (FT) and a slow transverse mode (ST), modulated by a_1 and a_2, respec-

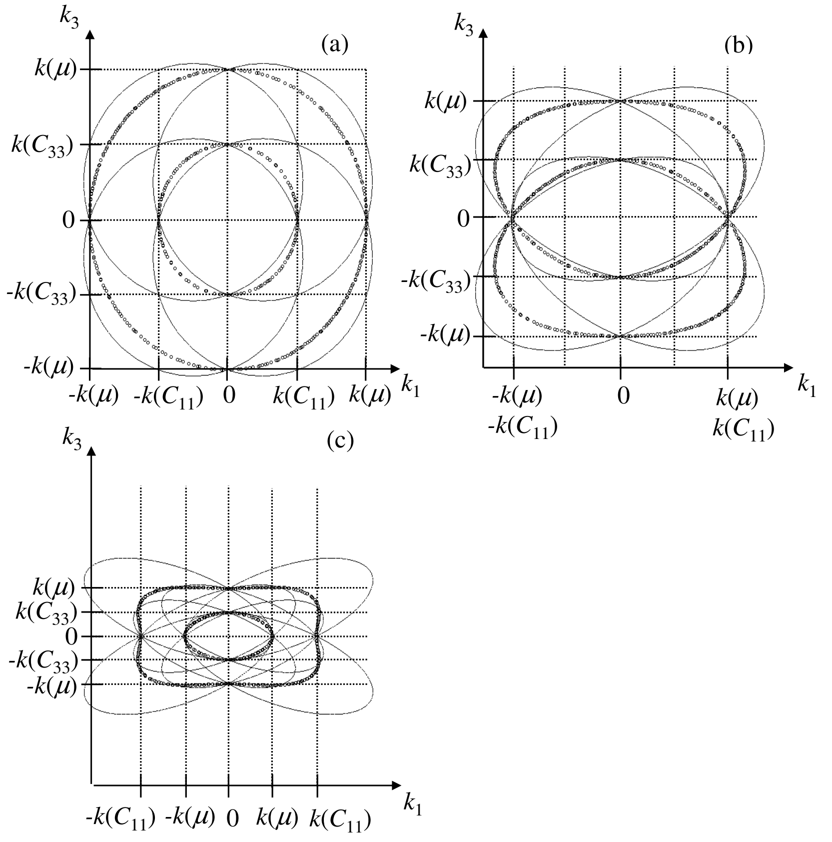

Abbildung 4.12: Implicit plot of $\omega(k_1, k_3)$. The material is assumed to be incompressible ($\nu_{31} = 1/2$) and the ratio C_{33}/μ_{13} is fixed to 4 (isotropic relation), whereas C_{11}/μ_{13} is varied with 4 (a), 1 (b) and 1/4 (c). The solutions to the fourth-order equation (4.17) yields the scattered plots, while the roots (4.18) and (4.19) are shown as line graphs. Tick marks: $k(\mu) = \omega\sqrt{\rho/\mu_{13}}$, $k(C_{11}) = \omega\sqrt{\rho/C_{11}}$ and $k(C_{33}) = \omega\sqrt{\rho/C_{33}}$.

tively. The lines of constant frequency $\omega_{1,2} = 2\pi f_v$ (f_v = vibration frequency) describe closed curves, which represent the waveform in k-space. Figure 4.12 exemplary shows the angular frequencies $\omega_{1,2}$ for three different constitutive ratios C_{11}/μ_{13} and C_{33}/μ_{13} that provide a measure for the anisotropy of the material. For an isotropic, incompressible medium Hooke's law yields $C_{11}/\mu_{13} = C_{33}/\mu_{13} = 4$. Transverse isotropy abolishes all constraints on C_{11} and C_{33} with respect to μ_{13}. However, C_{33} is assumed to be at least greater than $C_{11}/4$ for ensuring $E_3 > 0$ (see equation (5)). The apparent form of the shear waves observed in MRE experiments is determined by the superposition of the FT and ST wave modes (4.16) transformed back into spatial coordinates using equation (3.2). Therefore, analyzing the waveform requires an expression that accounts for the geometry of both wave modes in spatial coordinates. To tackle this goal the forth-order equations $\omega_{1,2}$ were approximated by second-order equations yielding a single

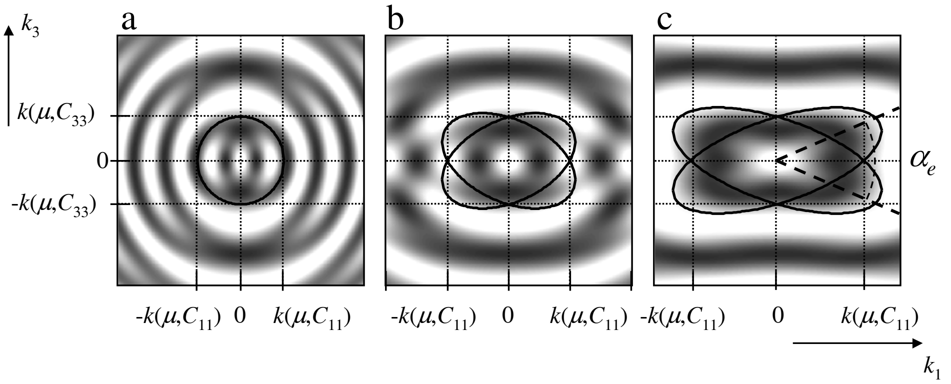

Abbildung 4.13: u_1 wave images calculated using (4.16) and the ratios C_{11}/μ_{13} = 4 (a), 1 (b), 1/4 (c) all with C_{33}/μ_{13} = 4. The elliptic approximations for ω_1 and ω_2 with $e4 = e5 = 0$ in (4.18) and (4.19) are superposed as line graphs. α_e defines the elliptic rotation angle. Tick marks: $k(\mu_{13}, C_{11}) = \omega\sqrt{\rho/\sqrt{\mu_{13}C_{11}}}$, $k(\mu_{13}, C_{33}) = \omega\sqrt{\rho/\sqrt{\mu_{13}C_{33}}}$.

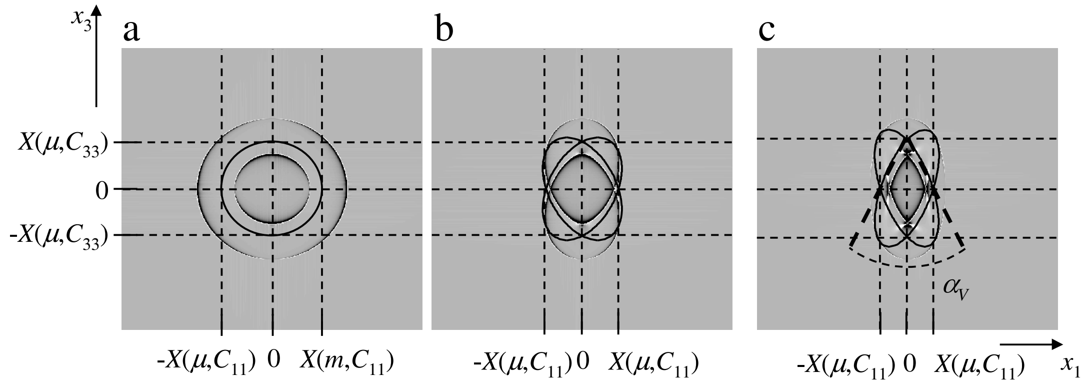

Abbildung 4.14: Real parts of u_1-waves calculated with C_{11}/μ_{13} = 4 (a), 1 (b), 1/4 (c) all with C_{33}/μ_{13} = 4. α_V is used to define the apparent V-angle given by (4.22). The axes labels refer to the positions $X(\mu_{13}, C_{11}) = \sqrt{\sqrt{\mu_{13}C_{11}}/\rho}/\omega$ or $X(\mu_{13}, C_{33}) = \sqrt{\sqrt{\mu_{13}C_{33}}/\rho}/\omega$.

apparent wave mode. In this approach the coefficients e_i of a squared elliptic equation,

$$\left(e_1k_1^2 + 2e_2k_1k_3 + e_3k_3^2 + 2e_4k_1 + 2e_5k_3 + e_6\right)^2 = 0 \tag{4.18}$$

are compared to the elastic coefficients of $\omega_{1,2}$ (4.17). This procedure yields 8 distinct ellipses with coefficients

$$\begin{aligned}
e_1 &= 2\sqrt{C_{11}\mu_{13}} \\
e_2 &= \pm\sqrt{\left|C_{33}\mu_{13} + C_{11}^2/4 + 2\mu_{13}\sqrt{C_{11}C_{33}} - C_{11}C_{33}\right|} \\
e_3 &= 2\sqrt{C_{33}\mu_{13}} \\
e_4 &= \pm\omega\sqrt{\rho}\sqrt{\mu_{13} - C_{11} - 2\sqrt{C_{11}\mu_{13}}} \\
e_5 &= \pm\omega\sqrt{\rho}\sqrt{\mu_{13} - C_{33} - 2\sqrt{C_{11}\mu_{13}}} \\
e_6 &= -2\omega^2\rho
\end{aligned} \tag{4.19}$$

as displayed in figure 4.12 for different anisotropic elasticities. The signs of the roots are chosen to obtain real ellipses. The waveform in k-space is now ascribed to superposed ellipses whereby a translation of the ellipses along k_1 and k_3 shall be neglected for further proceeding. This simplification implies that $e_4 = e_5 = 0$ and thus, two ellipses remain, which express the geometry of the apparent wave in terms of their axis ratio

$$R = \frac{r_1}{r_2} \qquad \text{where} \qquad r_{1,2} = e_1 + e_3 \pm \sqrt{(e_1 - e_3)^2 + 4e_2^2} \tag{4.20}$$

and the tilt angel

$$\alpha_e = \arctan 2e_2/(e_1 - e_3). \tag{4.21}$$

Since the symmetry is conserved during Fourier transformation the elliptic approximation can be used for geometrical considerations of the waveform also in spatial coordinates. An analytic expression for the V-angle (henceforth denoted as α_V) can be deduced from the ratio of the intercepts of the ellipses at the x_1- and x_3-axis as shown in figure 4.14(c):

$$\alpha_V = 2\arctan\left[\left(\frac{E_1}{E_3}\right)^{1/4}\right]. \tag{4.22}$$

This holds for $R >> 1$, i.e. the branches of the ellipses enclosing α_V can be approximated by straight lines. From this condition certain constraints for the deducibility of α_V arise according to the straightness of the wave fronts. In the case of anisotropy the wave vector $\mathbf{k}$ and the corresponding group velocity $\mathbf{v} = \partial\omega/\partial\mathbf{k}$ are not necessarily collinear so that interferences of plane waves may appear Taylor et al. [1969], Salo and Salomaa [2003]. Figure 4.15 shows the projection of $\mathbf{v}$ and $\mathbf{k}$ onto the k_1-axis, which shows that the direction of wave propagation is increasingly different from the wave normals with increasing anisotropy. An estimate of the degree of such internal interferences can be derived from the elliptic approximation by consideration of the tilt of the ellipses α_e

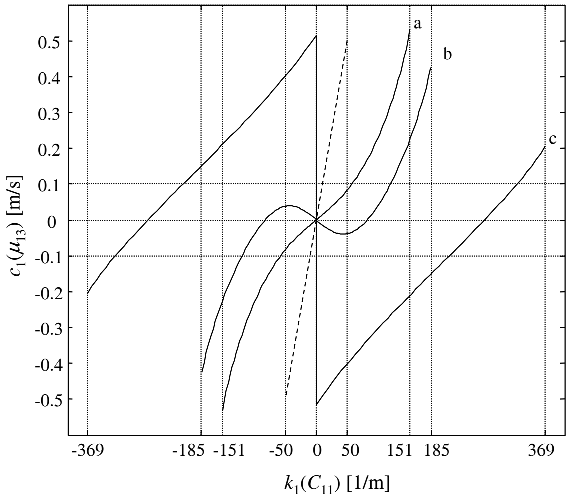

Abbildung 4.15: x_1-component of the group velocity $v_1 = \partial\omega_2(k_1, k_3)/\partial k_1$ versus k_1 with k_3-values derived from equation (4.19). The graphs (a),(b) and (c) were calculated with the elastic ratios used in figures 4.14(a), (b) and (c). The k_1-ticks correspond to ω= 100 rad Hz, ρ= 1.1 10^3 kg/m^3. It is visible that decreasing ratios C_{11}/μ_{13} and C_{33}/μ_{13} cause a increasing v_1 of opposite sign with respect to k_1. A negative component v_1 yields caustics since forward and backward running waves cross each other. The dashed line indicates the isotropic scenario, i.e. circular propagating waves.

and the elliptic aspect ration R:

$$R' = R \tan\left(\frac{\alpha_e}{2}\right) \tag{4.23}$$

i.e. the main axes of the ellipses are projected on k_1 and weighted by R. In spatial coordinates this provides an estimate of the directionality of the group velocity component v_1 relative to k_1. Now, the determination of the anisotropic elastic coefficients can proceed as follows: the wavelength on the x_3-axis in the u_1 image directly provides the shear modulus μ_{13}. This is the measurement commonly used in MRE. The second measurement is the V-angle α_V, that determines the ratio E_1/E_3. Additionally, the conditions of straightness (R) and interferences (R') constrain possible constitutive ratios C_{11}/μ_{13} and C_{33}/μ_{13}.

4.3.3 Finite Difference Simulations of Plane Stresses

Figure 4.16 shows three u_1-wave images calculated according to section 3.2.2 using elastic parameters C_{11}, C_{33} and μ_{13} that fit to the experimentally determined angle $\alpha_V = 55°$. It is visible that the straightness of the wave fronts is a crucial parameter to determine the elastic anisotropy of the tissue. While the waves in figure 4.16(a) show

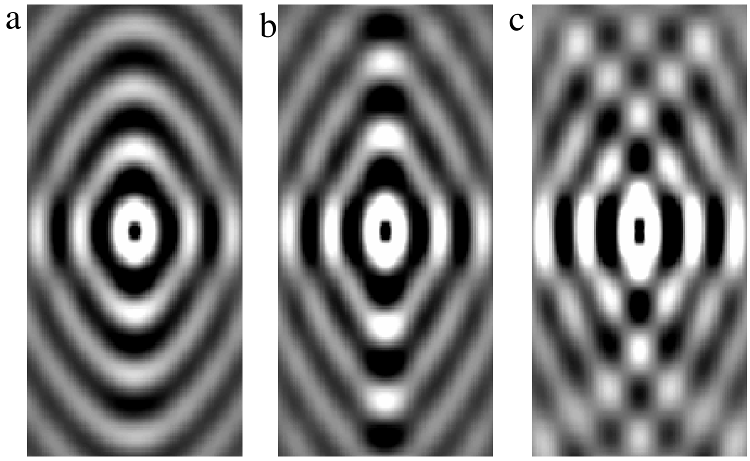

Abbildung 4.16: Finite difference simulations of u_1-waves applying a hypothetical x_1-excitation at the image center. The simulation parameters were chosen to constrain $\alpha_V \approx 55°$. with C_{11}/μ_{13} = 0.4406, C_{33}/μ_{13} = 6 (a); C_{11}/μ_{13} = 0.2937, C_{33}/μ_{13} = 4 (b); C_{11}/μ_{13} = 0.0734, $C_{33}/\mu_{13} = 1$ (c).

circular cusps and curved wave fronts, figures 4.16(b) and (c) display rather straight and tapered wave fronts, which allow the determination of α_V. The aspect ratio R (4.20) was determined with 5, 6.4 and 9.9, for figures 4.16(a), (b) and (c) respectively. Additional variation of the elliptic aspect ratio $R = 1$ to $R = 10$ (corresponding to isotropy, i.e. circular waves as shown in the experiment of figure 4.11(a) revealed an approximate threshold of $R = 6$ for discriminating between circular and straight wave fronts. This eye-guided estimate indicates that for small R-values equation (4.21) becomes obsolete since the observed wave shape is no longer represented by V-waves and thus, no α_V exists. Moreover, finite difference simulations revealed the influence of internal interferences to the apparent waveform. Such distortions of V-waves are clearly visible in figure 4.16(c). Since in MRE experiments, no such pronounced interferences were found certain combinations of C_{11}, C_{33} and μ_{13} could be excluded. The wave images shown in the figures 4.16(a) to (c) corresponding to R' = 1.4, 2.2 and 4.1, respectively, demonstrate that beyond a certain threshold of R' internal interferences dominate the apparent waveform. This empirical threshold was found to be R' = 3 which is equal to an inverse v_1-component (relative to k_1) of 0.1/s (figure 4.15). Figure 4.17 shows how the upper (R) and lower (R') margins of C_{11}/μ_{13} and C_{33}/μ_{13}, which apply for estimating the occurrence of V-waves. The gray patch indicates elastic ratios that yield V-waves, while the fat solid line corresponds to α_V = 55.. The conjunction of both criteria allowed the determination of the elastic ratios C_{11}/μ_{13} = 0.25±0.07 and C_{33}/μ_{13} = 3.4±1.0 for the biceps. Using the experimental shear modulus μ_{13}, C_{11} was derived with 13.5±4.5 kPa and C_{33} with 190±60 kPa yielding μ_{12}, E_1 and E_3 with 3.4±1.1, 13±4.5 and 185±60 kPa, respectively. Assuming a density of muscle tissue of approximately 1.1 kg/l the shear wave speeds perpendicular and parallel to the muscle fibers followed with 1.76±0.03 m/s and 7±1.65 m/s, respectively. Thus, the ratio between these two shear wave speeds is

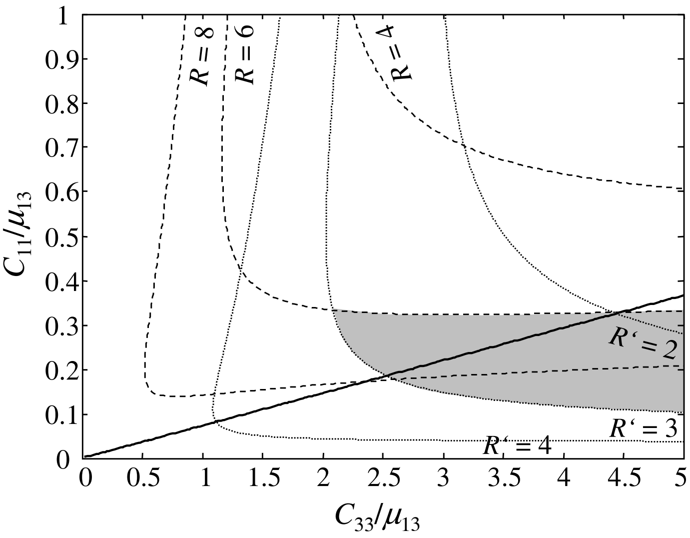

Abbildung 4.17: Contours of R and R' dependent on the constitutive ratios C_{11}/μ_{13} and C_{33}/μ_{13}. The isolines $R = 6$ and $R' = 3$ are used as thresholds enclosing the area of possible ratios where V-waves appear (gray patch). The fat solid line gives all constitutive ratios that yield an apparent V-angle $\alpha_V = 55°$ as observed in MRE of the human biceps.

approximately 1 to 4.

4.3.4 Analysis of Anisotropic Wave Patterns using Group Velocity Inversion

In the following section a method is developed and evaluated that uses the measurement of group velocities along profiles outwards from the focal source of waves. In contrast to the proceeding section a full 3D-model of plane shear waves is employed. A group velocity inversion (GVI) applicable to human muscle tissue requires knowledge of the plane wave modes (see section 2.3.2) that can propagate in the bulk of an incompressible material with transverse isotropy. Since the corresponding elasticity tensor **C** is not given in the literature, it is now derived from the compliance tensor **S** (2.36). There are three different Poisson's ratios for such type of material: ν_{31}, ν_{13} and ν_{21}. Due to the symmetry of **S** one finds $\nu_{31} = \nu_{32}$, $\nu_{21} = \nu_{12}$ and $\nu_{13} = \nu_{31} E_1 / E_3$. The trace of the strain tensor **ffl** is assumed to be a small number δ that is close to zero:

$$\epsilon_{ii} = \delta. \tag{4.24}$$

Then, for the Poisson's ratios, $\nu_{ij} = \epsilon_{jj}/\epsilon_{ii}$ (with $i \neq j$, no summation over repeating indices) follows

$$\nu_{ij} + \nu_{jk} = (1 - \zeta_{ii}) \qquad \text{where} \qquad \zeta_{ii} = \frac{\delta}{\epsilon_{ii}}. \tag{4.25}$$

Using equation 4.25 together with the symmetry properties of the compliance tensor all Poisson ratios can be expressed as function of only one ζ_{ii}. With respect to the principal axis x_3 one finds

$$\nu_{31} = \nu_{13}\frac{E_3}{E_1} \quad = \quad \frac{1}{2}\left(1 - \zeta_{33}\right). \tag{4.26}$$

Determination of the isotropic Poisson' ratio ν_{12} requires the evaluation of ζ_{11} in terms of ζ_{33}

$$\zeta_{11} = -\nu_{13}\zeta_{33} \quad = \quad \frac{1}{2}\frac{E_1}{E_3}\left(\zeta_{33}^2 - \zeta_{33}\right), \tag{4.27}$$

yielding

$$\nu_{12} = 1 + \frac{E_1}{E_3}\left(\zeta_{33} - \frac{\zeta_{33}}{2} - \frac{1}{2}\right) \tag{4.28}$$

The limit of incompressibility is then achieved by taking ζ_{33} to zero, which yields the Poisson's ratios

$$\begin{aligned} \lim_{\zeta_{33}\to 0} \nu_{31} &= \frac{1}{2}, \\ \lim_{\zeta_{33}\to 0} \nu_{12} &= 1 - \frac{1}{2}\frac{E_1}{E_3}. \end{aligned} \tag{4.29}$$

Hence, the elasticity tensor can be expressed in the limit ν_{31}=1/2:

$$C_{11} = \lim_{\nu_{31}\to 1/2} \frac{\left(E_3 - \nu_{31}^2 E_1\right) E_3}{\left(2\nu_{31} - 1\right)\left(\nu_{31}E_1 - 2E_3\right)\nu_{31}} \tag{4.30}$$

$$C_{12} = \lim_{\nu_{31}\to 1/2} \frac{\left(E_3 - \nu_{31}E_1 + \nu_{31}^2 E_1\right) E_3}{\left(2\nu_{31} - 1\right)\left(\nu_{31}E_1 - 2E_3\right)\nu_{31}} \tag{4.31}$$

$$C_{13} = C_{23} = C_{33} = \lim_{\nu_{31}\to 1/2} \frac{E_3}{1 - 2\nu_{31}} \tag{4.32}$$

$$C_{66} = \mu_{12} = \frac{E_1 E_3}{4E_3 - E_1} \tag{4.33}$$

$$C_{44} = C_{55} = \mu_{13} \tag{4.34}$$

Apart from the shear moduli μ_{12} and μ_{13}, all elements of the elasticity tensor diverge. Inserting the algebraic expressions of C_{ijkl} into equation (2.49) and solving for c^2 yields three eigenmodes in the limit $\nu_{31} \to 0$, including one diverging longitudinal wave mode that is discarded from further analysis. The remaining two modes are determined using

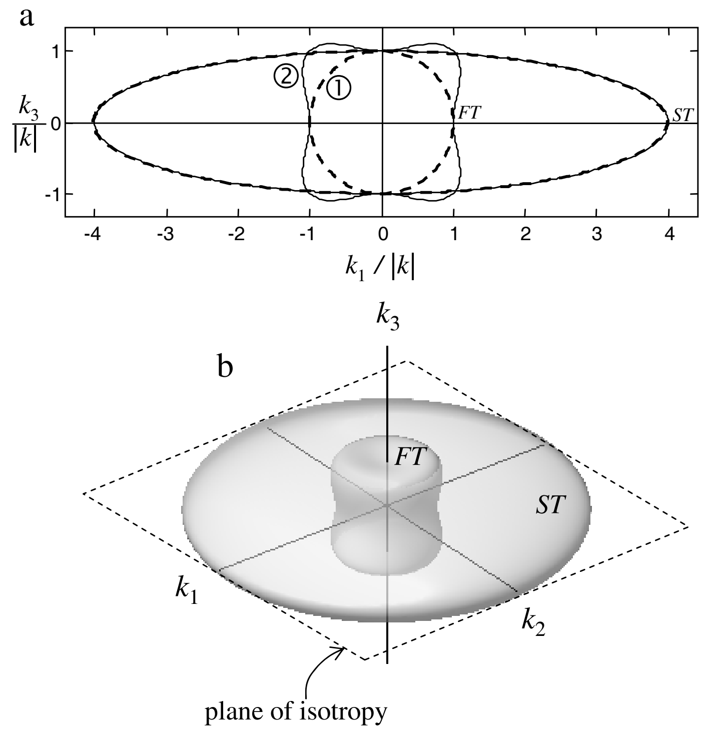

Abbildung 4.18: Phase velocity surfaces $\rho c_M^2 = 1$ kPa according to (4.35) in normalized k-space plotted for two elastic scenarios. (a): $\mu_{12} = 1/16$ kPa, $\mu_{13} = 1$ kPa, $E_3/E_1 = 16$ (case 1, dashed graphs), $E_3/E_1 = 8$ (case 2, solid graphs; unit density of 1 kg/l). The concave curvature of the FT-mode of case 2 yields caustics of spatial waves Musgrave [1970]. (b): 3D representation of case 2 in (a).

de l'Hôpital's rule:

$$\begin{aligned} \rho c_{ST}^2 &= \mu_{12}\left(n_1^2 + n_2^2\right) + \mu_{13} n_3^2 \\ \rho c_{FT}^2 &= 4\left(\mu_{13} - \mu_{12}\frac{E_3}{E_1}\right)\left(\frac{n_3^4}{\mathbf{n}^2} - n_3^2\right) + \mu_{13}\mathbf{n}^2, \end{aligned} \tag{4.35}$$

where $\mathbf{n} = \mathbf{k}/|\mathbf{k}|$ represents the wave normal vector. Figure 4.18 shows the shape of phase velocity contours of ST- and FT-mode for two elastic cases that deviate solely by the ratio of the Young's moduli E_3/E_1. Since the ST-mode controls pure out-of-plane displacement in the case of transverse isotropy, c_{ST} in equation (4.35) also applies to compressible media. Its shape is described by an ellipsoid whose axes are determined by μ_{12} and μ_{13}. In contrast, c_{FT} additionally depends on the ratio E_3/E_1, resulting in more complex wave patterns for $E_3/E_1 \neq \mu_{13}/\mu_{12}$. Since the FT-mode also describes in-plane motions, the given expression applies only to incompressible materials. The displacement field in real space resulting from harmonic transducer motions can be

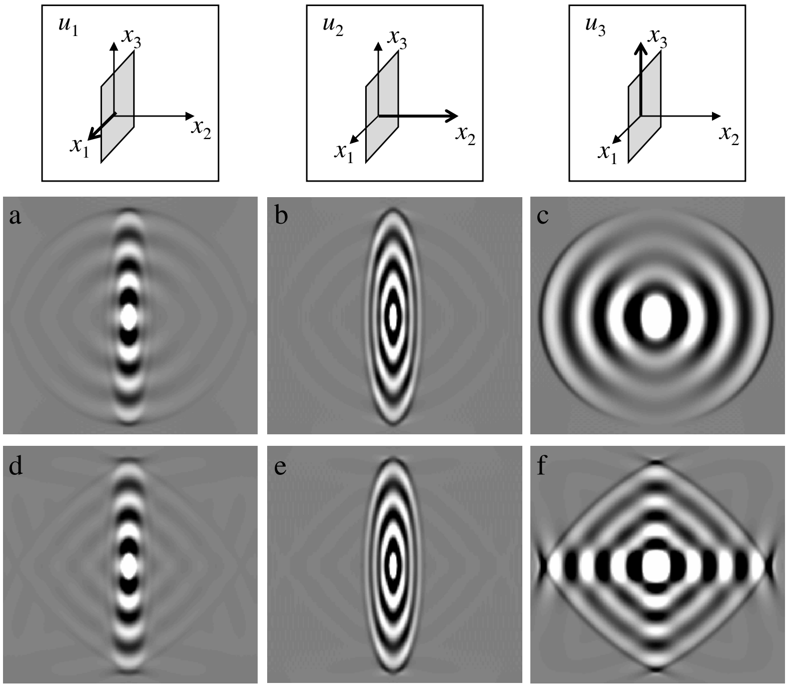

Abbildung 4.19: Calculated wave images using equation (.15). The plane of projection and the polarization of **u** (which is parallel to the polarization **U**) are symbolized in the pictograms at the first row. The elastic parameters correspond to cases 1 (a) to (c) and 2 (d) to (f) in figure 4.18(a). The image planes are aligned with the principal axis system so that ST- and FT-wave modes can be seen separately. The out-of-plane deflection given in (b) and (e) is governed by c_{ST}, while transverse waves travel perpendicular to this plane with c_{FT} (see equation (4.35)).

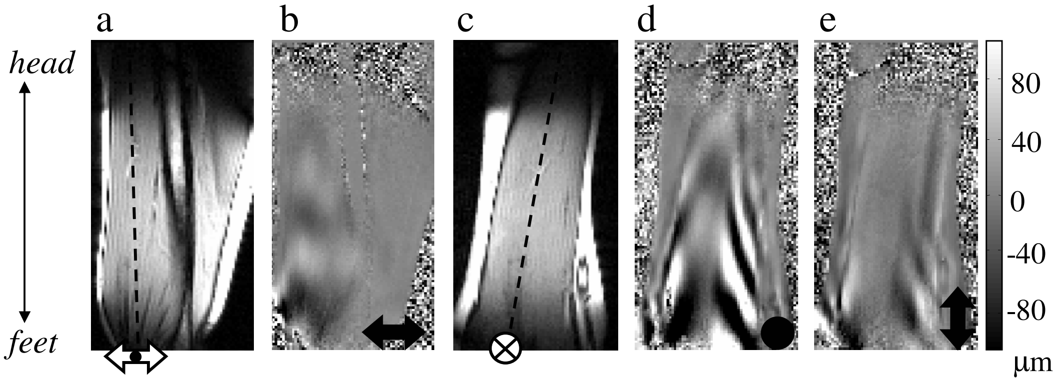

Abbildung 4.20: MRE of the human biceps with mechanical excitation of 99 Hz. The magnitude images (a) and (c) display the anatomical contrast of the adjacent phase-difference images (b), (d), and (e). The perpendicular image planes are aligned with the long axis of the biceps, which represents the mutual image axis (dashed graphs). White symbols indicate the direction and the source of in-plane (arrows) and out-of-plane (cross) vibrations. The actuator attached to the distal tendon induced mainly unidirectional up-and-down vibrations. Correspondingly, the black symbols indicate the direction of motion sensitization and thus the polarization of the waves. (a): Image slice parallel to the vibration direction with demarcation (dashed line) of the position of the perpendicular images (c), (d), and (e). (b): Transverse in-plane waves corresponding to the FT-mode (cf., figure 4.19(a) and (d). (c): Image plane through the origin of the waves perpendicular to the motion. The dashed line indicates the image plane of (a) and (b). (d): Out-of-plane waves parallel to the direction of the transducer vibrations $u_2(x_1, x_3, t)$. This setup was applied in volunteer studies to acquire pure ST-wave images. (e): In-plane motions encoded perpendicular to the major direction of wave excitation. Since an excitation of waves parallel to the tendon was experimentally not feasible, only minor fractions of the waves arise in the vicinity of the muscle boundaries.

calculated as described in methods section 3.2.2. Accordingly, figure 4.19 shows the displacement vector components $u_1(x_1, 0, x_3)$, $u_2(x_1, 0, x_3)$, $u_3(x_1, 0, x_3)$ with excitation along x_1, x_2, and x_3, respectively, for the elastic scenarios corresponding to figure 4.18. It is apparent that μ_{12} and μ_{13} are simultaneously accessible by out-of-plane waves, while the ratio E_3/E_1 can only be estimated by in-plane deflections. To analyze the experiments, it is necessary to know whether the observed waves in MRE are due to the ST-mode, the FT-mode, or a superposition of both wave modes. Fortunately, MRE allows the encoding and, in some cases, also the excitation of single components of $\mathbf{u}$ with an arbitrary image slice position. In the experiments pure ST-waves are observed, since only motions perpendicular to the image plane were excited and encoded. In

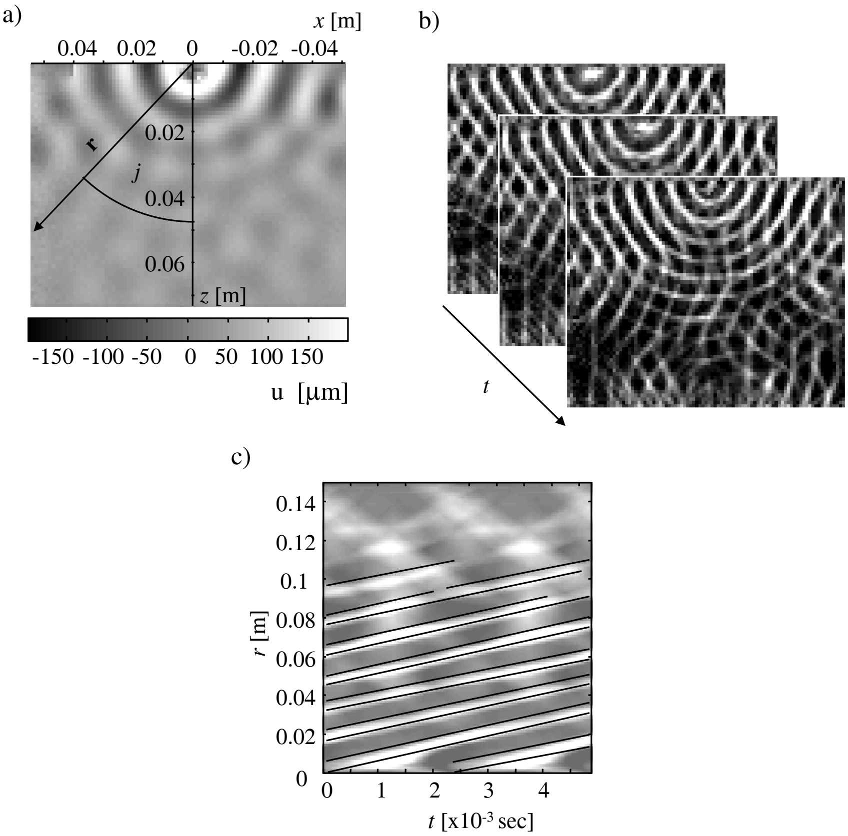

Abbildung 4.21: Experimental MRE wave image of agarose subjected to 205 Hz mechanical excitation. For determination of group velocities $\mathbf{v}(\varphi)$ the vector r is rotated with φ (a). (b): Phase symmetry-enhanced contrast images of a with additional temporal resolution to demonstrate the propagation of wave fronts. (c): Symmetry enhanced wave propagation of a 1D-spatial profile corresponding to the vector r in (a) with φ =45°. Lines of constant phase (solid lines) were automatically found using edge detection. The algorithm was adjusted to ignore fractional wave fronts due to boundary effects (here at r >0.11 m). The slopes of the curves represent $\mathbf{v}(\varphi = 45°)$.

general, the experimental setup is chosen in such a way as to avoid a superposition of ST- and FT-wave modes. Thus the image plane must be aligned with the principal axes of the wave field, which in turn will be polarized along a principal axis of the elasticity tensor. ST- and FT-waves are then separately visible so that $\mathbf{v}_M(\varphi)$ (see also figure 2.6) can be analyzed by the corresponding c_M in equation (4.35). The analysis of group velocities $\mathbf{v}(\varphi)$ (assignable to an arbitrary wave mode M) is based on rays $\mathbf{r}(\varphi)$ (with length r) emanating from the apparent point source of the waves. Along such rays, the wavelength λ varies with φ due to the anisotropy of the elasticity.

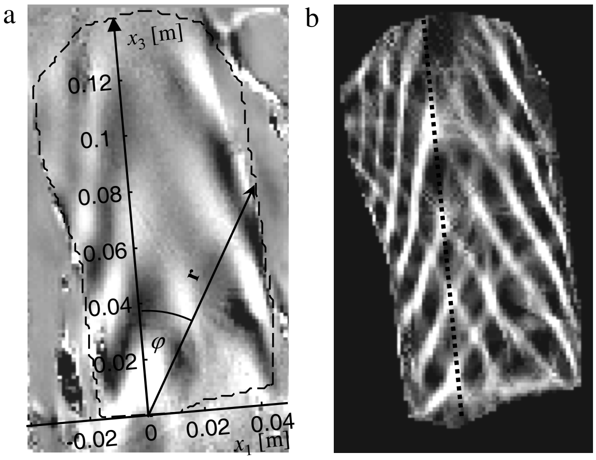

Abbildung 4.22: Wave data $u_2(x_1, x_3, t)$ of volunteer 1. (a): Phase contrast MRE wave image acquired with 126.3 Hz mechanical actuation. The length of r was constrained by the boundaries of the ROI (dashed line). (b): Symmetry-enhanced wave image of (a). The principal muscle axis (indicated as dotted line) is clearly distinguishable through tapered waves.

4.3.5 Automatic Data Evaluation Protocol for Group Velocity Inversion

As a result of the derivations made in the previous section, GVI in MRE requires the following steps:

1. Manual demarcation of the coordinate system and the lengths of **r** as shown in figure 4.21(a).

2. Interpolation of $r - t$-images ($u_2(\mathbf{x}, t)$) corresponding to $\mathbf{r}(\varphi)$.

4. Automatic recognition of the slopes in $u_2(x, t)$ (see figure 4.21(c)), that correspond to $\mathbf{v}(\varphi)$, by an edge detection algorithm.

4. Fit of the experiments: The analytical solution of equation (2.51) is used with variable combinations of μ_{12} and μ_{13} to calculate $\mathbf{v}_{ST}(\theta)$. Then, $\varphi(\theta)$ is calculated using

$$\varphi = \arctan \frac{v_1}{v_3} \tag{4.36}$$

to map $\mathbf{v}_{ST}(\theta)$ versus $\varphi(\theta)$ and determine the variation between experimental and calculated curves. The variation is defined here as the mean of $|\mathbf{v}(\varphi) - \mathbf{v}_{ST}(\varphi(\theta))|$ normalized by the standard deviation (SD) of the experimental data. This procedure was repeated 100 times from 0.5 to 20 kPa with independently varying μ_{12} and μ_{13}. The resulting variations were stored in memory as functions of μ_{12} and

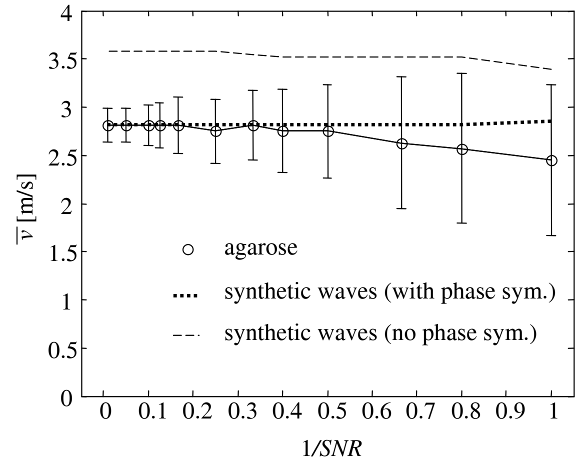

Abbildung 4.23: Application of the wave inversion program to synthetic isotropic waves and phantom experiments modified by added noise. In simulations $\hat{v}$ (i.e., the mean of v_1 and v_3) was 2.87 m/s for reproducing phantom experiments at their initial SNR of 82. Edge detection with synthetic data was performed with and without phase symmetry enhancement ($r = \lambda$ for all data).

μ_{13}. The shear moduli at the global minimum of all variations were taken as the final results. The value of the minimum itself was used as error tolerance of the wave speeds if no multiple experiments were performed (as in volunteer 2).

This routine was tried with $r=\lambda$ on synthetic circular waves with $\bar{v} \equiv (v_1 - v_3)/2 = 2.87$ m/s, and on experimental circular waves observed in agarose. The stability against a decrease of SNR was investigated by adding noise to both synthetic and experimental waves. In muscle the x_1 and x_3- coordinates were aligned corresponding to the direction of largest wavelengths, as demonstrated in figure 4.22. The length of r was limited by the size of the region of interest (ROI), yielding $r = 0.13$ m, 0.134 m, 0.11 m, 0.107 m, and 0.132 m for volunteers 1-5, respectively. Equation (4.35) provides an analytical relation between the elastic moduli and phase velocity surface, showing that μ_{12}, μ_{13}, and the ratio E_3/E_1 are the only elastic parameters that are relevant for GVI applied to incompressible, transversely isotropic media. Interestingly, it is not possible to deduce all three elastic parameters from a single component of $\mathbf{u}$. This is illustrated by figure 4.19, which shows the dependency of the shear wave form on distinct functions of phase velocity in k-space (figure 4.18). These simulations reproduce the experimental scenarios shown in figure 4.20, which reveal that only the ST-waves on the biceps bear significant information about the elastic anisotropy of the material. In contrast, waves belonging to the FT mode are either limited due to muscle boundaries or are too weakly excited by the conventional actuator that is based on a rocker design. Consequently, the setup of volunteer experiments was chosen to obtain waves correspondingly to figure 4.20(d). Figure 4.23 demonstrates the effect of noise on the inversion technique.

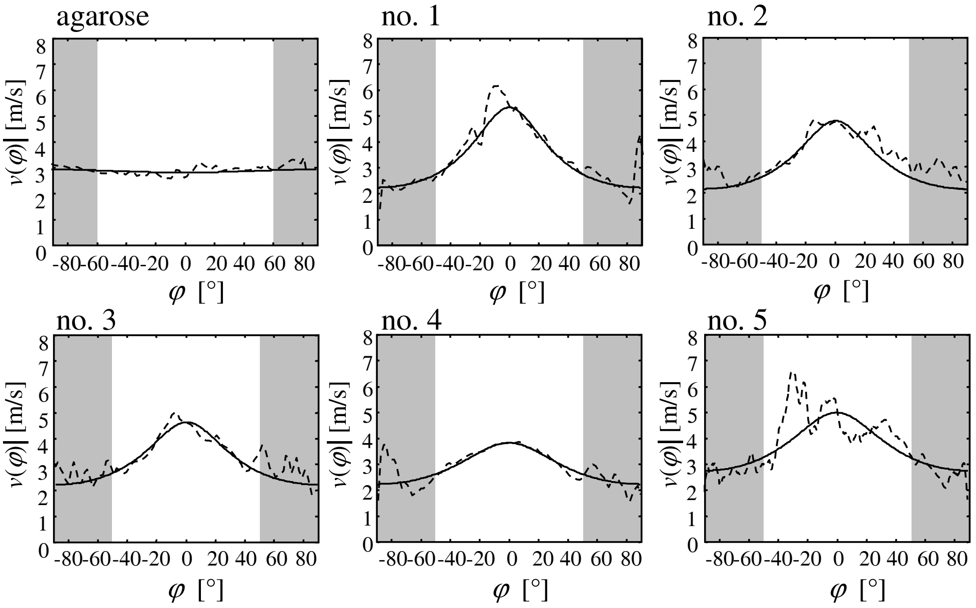

Abbildung 4.24: Experimental magnitude of group velocities $v(\varphi) = |\mathbf{v}(\varphi)|$ in agarose and human biceps of volunteers 1-5 (corresponding to the labels above the graphs). Although φ was varied between ±90° a constricted range was used to determine the minimum variation between experiment (dashed graphs) and simulated $\mathbf{v}_{ST}(\varphi)$ (solid curves). The considered φ range (white area) was ±80° for agarose and ±60° in muscle experiments, which takes into account that the ROI is shorter in x_1 than in x_3 (see figure 4.23(a)). The values of μ_{12} and μ_{13} used to fit the data are listed in 4.1

The variation in the fit of the synthetic data was at maximum ±0.4 m/s. Omitting the phase symmetry enhancement prior to the edge detection resulted in an overestimation of the wave speeds of about 30%. This deviation decreased with an increasing length of the rays. An r of approximately 4λ yielded correct wave speeds even without phase symmetry enhancement. The wave speed in agarose was found to be 2.87±0.19 m/s at the initial SNR of 82. Decreasing SNR leads to an about 15% underestimation of $v(\varphi)$ at SNR=1. Synchronously, the error tolerances increase up to 300%, which indicates increased scattering of the detected wave slopes, although their mean remains largely constant. Figure 4.24 illustrates GVI on the human biceps of five volunteers in comparison to isotropic waves acquired in agarose. The group velocities of muscle tissue clearly differ from isotropic wave speeds by the shape of their functions over φ. While the wave speed vector $\mathbf{v}$ of an isotropic elastic material is represented by a circle with constant radius v, in muscle tissue $v(\varphi)$ changes elliptically with v_3 greater than 2.86 (±0.41)v_1 (interindividual median). The group velocities and corresponding shear moduli used to fit the experiments are listed in 4.1. No significant correlation between

	Agarose	1	2^a	3
v_1 [m/s]	2.93 (0.19)	2.22 (0.23)	2.27 (0.19)	2.21 (0.36)
v_3 [m/s]	2.81 (0.19)	5.32 (0.23)	5.28 (0.45)	4.62 (0.36)
v_3/v_1	0.97 (0.13)	2.43 (0.35)	2.36 (0.4)	2.18 (0.52)
μ_{12} [kPa]	9.5 (1.22)	5.48 (1.1)	5.69 (0.95)	5.51 (1.75)
μ_{13} [kPa]	8.74 (1.17)	31.21 (2.64)	30.89 (5.23)	23.66 (3.67)
μ_{13}/μ_{12}	0.95 (0.25)	6.03 (1.69)	5.74 (1.87)	5.02 (2.26)

Tabelle 4.1: Shear wave velocities of the slow transverse (ST) mode (v_1, v_3) and anisotropic shear moduli (μ_{12}, μ_{13}) of agarose and the biceps muscle of volunteers 1 to 5^*.

* The variations between simulation and experiments are given in parentheses. In muscle tissue, μ_{12} corresponds to the shear modulus perpendicular to the muscle fibers (within the plane of isotropy), while μ_{13} represents the shear stiffness parallel to the fibers.

^{a} In this column, the tolerances correspond to the standard deviation between eight experiments performed on five different days with variable mechanical excitation frequencies from 75 to 118 Hz.

^{b} The median of all volunteer studies with 95% confidence intervals.

	4	5	$1\text{-}5^b$
v_1 [m/s]	2.22 (0.25)	2.69 (0.44)	2.22 (0.18)
v_3 [m/s]	3.82 (0.25)	5.13 (0.44)	5.13 (0.55)
v_3/v_1	1.75 (0.31)	1.99 (0.49)	2.35 (0.44)
μ_{12} [kPa]	5.5 (1.2)	8.18 (2.6)	5.46 (0.88)
μ_{13} [kPa]	16.11 (2.07)	29.21 (4.96)	29.28 (6.21)
μ_{13}/μ_{12}	3.17 (1.07)	4.19 (1.94)	5.7 (2.06)

Tabelle 4.2: Table 4.1 continued.

shear wave speed and vibration frequency was found. The limit of viscosity that would cause significant wave dispersion in the biceps can be estimated by assuming Voigt's relation between wave speed dispersion and excitation frequency in a viscous body. Such maximum viscosity is approximately given by 3.5±1.0 Pas. Since no dispersion was found in the experiments, any possible viscosity is assumed to be below this value and thus all shear moduli presented in 4.1 were calculated in the absence of viscosity, which resulted in an error below the experimental accuracy.

4.3.6 Position Dependence of Group Velocity

The source location may be difficult to determine precisely under experimental conditions. For this reason the sensitivity of the GVI to dislocations of the presumed source location was analyzed. Figure 4.25 shows the components of the group velocity as func-

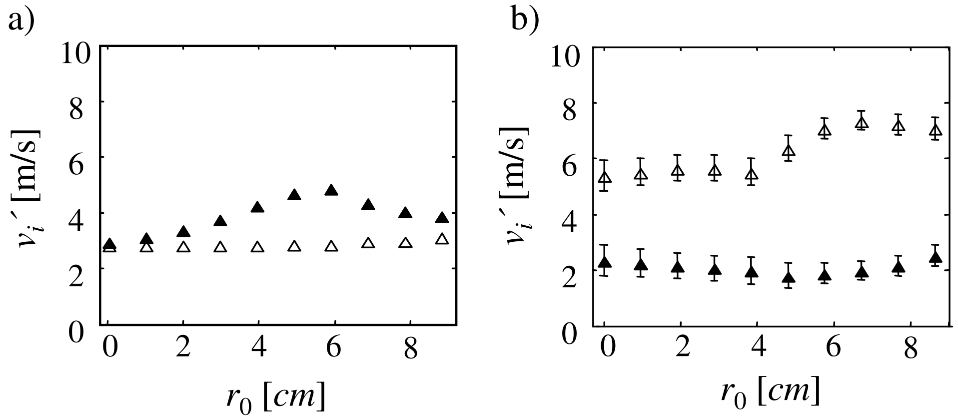

Abbildung 4.25: Position dependent velocity components v_1' (closed symbols) and v_3' (open symbols) determined at $\mathbf{r}_0 = [0, 0, x_3]$ away from the original source location. (a) as measured in agarose (error bars are within symbol size) and (b) measured in human biceps at r_0 away from the distal tendon.

tion of displacement r_0 of the source location along x_3 as determined by GVI applied to isotropic agarose and human biceps. In case of agarose it is seen that the velocity component v_1 is increasing due to geometric biases with increasing distance from the original source location. Above 6 cm ray length a decrease of v_1 with further increase of ray length is seen. In contrast, such a behavior is not observed in human muscle. There, v_1 remains constant over approximately the same range of r_0 it increases in agarose. In case of a dislocation of the source location the components of the apparent wave speed v_i' differs from the true v_i due to geometrical biases of the waves along x_i

$$v_i' = \lambda_i' \frac{\omega}{2\pi}, \qquad \text{with} \qquad \lambda_i' = \frac{x_i - x_{i0}}{N}. \tag{4.37}$$

N is the number of repeated waves along $\mathbf{r}$ ($N = x_i/\lambda_i$; no summation over i) due to the continuous wave excitation. The distortions on the apparent wavelength along the x_i- axis λ_i' can be quantified in a straightforward way for elliptic wave patterns. $\mathbf{r}_0$ and $\mathbf{r}$ can be related to the true wavelengths λ_i using

$$\left[\sum_{i=1}^{3}\left(\frac{x_{0i}}{\lambda_i}\right)^2\right]^{1/2} = N_0 \tag{4.38}$$

and

$$\left[\sum_{i=1}^{3}\left(\frac{x_i}{\lambda_i}\right)^2\right]^{1/2} = N_0 + N. \tag{4.39}$$

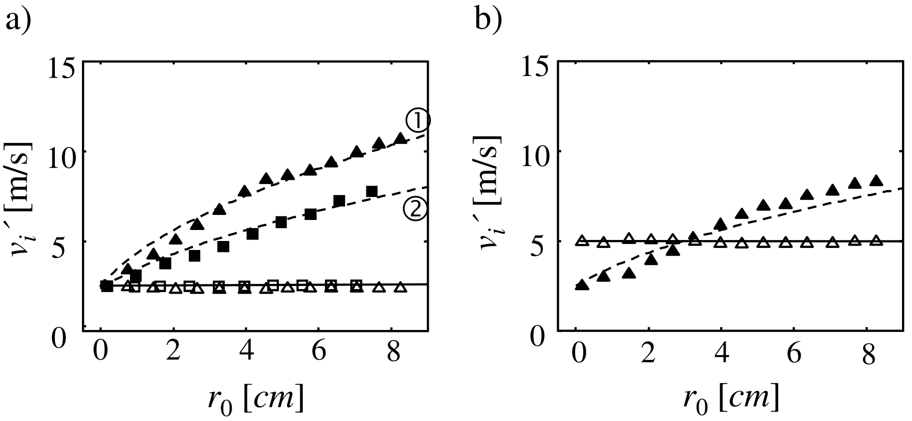

Abbildung 4.26: Position dependent velocity components v_1' (closed symbols) and v_3' (open symbols) determined at $r_0 = [0, 0, x_3]$ (a): wave speeds of synthetic isotropic waves emerging from a point source at $x_i = 0$ ($\lambda_1 = \lambda_3 = 0.0125m$, $v_1 = v_3 = 2.5m/s$). The solid line shows that v_3' is constant with $v_3' = v_3$. The increasing dashed lines were fitted to data received with $r = 0.75\lambda_3$ (1) and $r = 1.5\lambda_3$ (2). (b): Components of $\mathbf{v}'$ of synthetic anisotropic waves that are equivalent to (a) but $\lambda_3 = 0.025m$ ($v_3 = 5m/s$). Inversion and simulation were performed using $r = 0.75\lambda_3$.

For the initial case of $r_0 = |\mathbf{r}_0|$ and $\mathbf{r}||\mathbf{e}_i$ equations (4.37), (4.38) and (4.39) yield $\lambda_i' = \lambda_i$. The same results for $\mathbf{r}_0||\mathbf{e}_i$ and $\mathbf{r}||\mathbf{e}_i$ whereas a perpendicular dislocation requires the knowledge of x_j and x_k for deriving x_i ($i \neq j, k$). For example with $\mathbf{r}_0||\mathbf{e}_j$ and $\mathbf{r}||\mathbf{e}_i$ we can write $x_j = N_0\lambda_j$ so that the apparent wavelength follows with

$$\lambda_i' = \lambda_i\sqrt{2\frac{N_0}{N} + 1}. \tag{4.40}$$

Equation (4.40) holds for any $\mathbf{r}_0$ if the wave profile runs parallel to $\mathbf{e}_i$. The ratio N_0/N represents the dislocation over profile length, which equals $\sqrt{x_{0j}^2 + x_{0k}^2}$ where $(i \neq j \neq k)$. Consequently, the maximum bias occurs if $\mathbf{r}_0 \perp \mathbf{r}$. From (4.40) follows that the apparent shear modulus depends linearly on N_0. Figure 4.26 shows the components of group velocity as determined by application of GVI to simulated waves. Note that if $\mathbf{r}_0 \neq \mathbf{0}$, the apparent wavelength is always larger than the true wavelength and consequently the minimum of $v_i'(\mathbf{r}_0)$ can indicate the location of the wave source. N_0 and N need not be integers and can be identified as distances to the source normalized by the corresponding wavelength, i.e. $N_0 = r_0/\lambda_3$ and $N' = r/\lambda_1'$ (see figure 4.27).

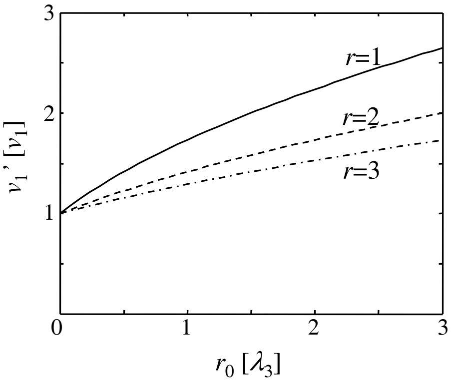

Abbildung 4.27: The apparent wave speed according to (4.40) in units of the correct wave speed as function of dislocation $\mathbf{r}_0$ at three different ray lengths r (in units of λ'). It is seen that the bias decreases with increasing ray length and increases with increasing distance from the source.

5 Discussion and Conclusions

5.1 MRE on Isotropic Materials

The results presented in section 4.1 demonstrate that AHI based on discrete and noisy wave data yields frequency dependent apparent phase speeds (figure 4.3), even when the material is not intrinsically dispersive. The excellent agreement of the plane-wave model (4.7) with experimental and simulated data shown in figures 4.3 and 4.4 suggests that at low resolution (λ/a) the discrete second derivatives in (4.3) yield overestimated apparent phase speeds. On the other hand, at large λ/a noise decreases the speed below its correct value. Between these two limits an optimal λ/a exists, where the true phase speed is measured. However, in a real experiment waves are hardly perfectly plane and therefore biases due to diffraction on the apparent phase speed cannot be entirely excluded. This is supported by the results of AHI applied to simulated waves due to different actuator plate sizes shown in figure 4.5. However, biases can be minimized by using out-of-plane displacement data for AHI as shown in figures 4.5 and 4.6. There, the pressure field is weaker than in case of $u_{11}(x_1, x_2, \omega)$, where it strongly biases the determined phase speed. Hence the presence of a pressure field in this direction is responsible for the strongly varying apparent phase speed obtained from in-plane data. Moreover, the ROI encloses only one to two wavelengths at large λ/a or correspondingly at low driving frequencies. In contrast to the simple plane-wave model, the half-space model features a near field in this region, which shows different wave numbers than the far field. This can be seen from the increase of c^* with increasing λ/a in figure 4.6(a). In conclusion, large plate sizes, low vibration frequencies and a ROI close to the actuator plate yield overestimated apparent phase speeds, which is in agreement with findings in the literature Sandrin et al. [2004], whereby $u_{33}(x_1, x_2, \omega)$ is least affected. The situation close to the source could be further complicated by surface effects such as Rayleigh waves or head waves Aki and Richards [2002], Benech and Negreira [2005], which are not included in our model. Therefore, the following recipe for minimizing systematic errors in the apparent phase speed is deduced: AHI should be based on out-of-plane displacement, with a direction of motion encoding that is preferably parallel to the direction of actuator motion. The phase speed should be spatially averaged in order to better approach a plane-wave behavior of experimental waves and thus to minimize biases on c^* due to diffraction and near field. Then, the dispersion is mainly governed by noise and discretization according to (4.7). This allows the determination of correct phase speeds, if the optimal λ/a at the given noise-to-signal ratio is chosen. Instead of consulting figure 4.4 to find the optimal λ/a, the fitting function $\lambda/a \approx 2\sqrt{2}\pi/\sigma$ can be used to directly calculate the required resolution. Although this study demonstrates the potential of AHI to deduce correct phase speeds and shear moduli from planar MRE data, further investigation is required to elaborate the size and the position of the ROI relative to the actuator geometry. It should also be noted that filters, like those for suppressing noise, change the effective wavelengths in the image. Thus, a careful match of filter thresholds may be able to compensate for dispersive effects as seen in figure 4.3 Klatt et al. [2007]. However, this does not impair principal findings of this study, since the refinement of filter parameters is certainly improved by the knowledge about AHI-intrinsic biases. Finally, although this study accounted for two dimensions, similar effects of noise and discretization are expected for 3-D inversion techniques. However, one important source of error in planar MRE is not relevant in 3-D methods: The occurrence of geometrical biases as investigated in the section of group velocity inversion 4.3.6.

5.2 Shear Wave Scattering from a Nonwelded Interface

A further effect observed in MRE is the scattering of shear waves from elastic discontinuities. It was demonstrated in section 4.2 that wave scattering can be used as basis for a wave amplitude analysis which allows to measure the weldedness of soft material layers. The results agree with theoretical predictions of SH-wave scattering from a linear slip interface in the dynamic range of in vivo MRE. In this model, the weldedness of two layers is deduced from the discontinuity of wave amplitudes at an interface and the traction across this interface. These quantities are combined in κ as a phenomenological means for characterizing interfaces and elastic contacts in elastography. However, κ provides only limited insight into the elastic properties of the underlying materials. Therefore, Schoenberg [1980] introduced the three-layer model given in section 2.3.8. There, κ is related to the stiffnesses of an intermediate layer, the surrounding medium and the thickness of the layer. If the thickness is small compared to the length of shear waves, equation (2.86) is valid. However this limit is exceeded by the frequency range examined in this study as demonstrated in figure 4.10. Resonances of the scattering coefficients characterized by maximum transmission and no reflection of wave energy at integer multiples of $f = \bar{c}/2d$ were not seen in the experiments. Figure 4.10 further illustrates that such resonances can be suppressed if viscosity is taken into account as given by equation (2.87). A transmission coefficient similar to that of the linear slip model is obtained at a viscosity of 3.6 Pas. However, the loss of wave energy shown by the low reflection coefficient in figure 4.10 indicates that η is presumably overestimated and there are further transport mechanisms of wave energy through the interface. Also the discrepancy between experimental and fitted c_0 indicates the limited applicability of (2.86) for explaining the physical meaning of ξ or κ. In our analysis, wave amplitudes were related to SH-wave scattering, assuming an alignment of the plane wave driver parallel to the interface and the corresponding adjustment of the scanner frame. Although the experimental setup was optimized to solely capture SH-waves, a small contribution of P- and SV-waves to the wave images as shown in figure 4.8 cannot entirely be excluded. In more realistic situations, the existence of multiple interfaces in oblique positions to each other would prevent a distinction between SH-and SV-waves as made in this study. For instance, in human brain MRE, sulci, blood vessels and interfaces between gray and white matter cause multiple scattering of shear waves with unclear directionality and polarization of the incident and the reflected waves. The quantification of in vivo scattering experiments is thus more complex and cannot be solved by the equations used in this study. On the other hand, the quality of amplitude variations can be utilized to identify the location of interfaces in complex media Sack et al. [2006]. This observation agrees well to the wave images shown in figure 4.8 where the non-welded interface is clearly distinguishable by means of steep amplitude changes. In future MRE applications the scattering of shear waves might be exploited to gain information on the mechanical properties of local lesions and tumors. This would describe an improvement to algebraic techniques such as AHI, for which it was demonstrated that only spatially averaged moduli can be determined. Therefore, studying principal effects of shear wave scattering is a crucial step towards in vivo scatter-based MRE Sack et al. [2005].

5.3 MRE on in vivo Human Biceps

In sections 4.3.2 and 4.3.3 it was shown that the anisotropic wave patterns observed in MRE experiments on human biceps can be described by a model of transverse isotropic under plane stress. From figures 4.11(b) and (c) it is visible that a rotation of the image plane around the main axis of the muscle does not change principle characteristics of V-waves. The assumption of cylindrically symmetric waves from 2D-MRE images is still the most compelling 3D-wave shape in muscles. It was shown that a V-waveform arises independently of the wavelength λ_3, implying that the stiffness of the muscle due to muscle load does not influence the waveform. Further, V-wave patterns with an equal angle α_V were found among different individuals as shown in Sack et al. [2002]. Also in muscles other than the biceps tapered patterns have been observed (data not shown), which were, however, more convoluted and superposed due to overlaid and less separated muscle groups. This indicates that living human skeletal muscles impose characteristic wave patterns due to characteristic symmetries of the elasticity tensor. However, the occurrence of V-waves is restricted to non-reflecting boundary conditions as well as an excitation via tendon. If the waves are excited by a point source the waveform is governed by elastic properties of the material rather than shape and surface pressure of the actuator. Then, the waveform analysis proposed in section 4.3.2 is applicable to 2D MRE wave data. Since it is based on a two-dimensional description of the wave propagation it can directly be applied to MRE waves, which are commonly acquired as 2D-image slices. The used simplification of planar stresses is justified for a cylinder symmetrical problem if the torsion component of the acting force is zero and the analyzed waveform does not depend on the rotation of the image plane. Under these assumptions it is possible to derive simple analytical expressions for the 2D-waveform as well as to implement a finite difference scheme to solve the equation of motion. The assumption of plane stresses is obsolete if the actuator produced torsion of the tendon or the image plane was off-centered within the muscle. The plane stress model reveals two wave modes with different wave speeds that are superposed in the waveform observed by MRE. The angular frequencies $\omega_{1,2}$ given in (4.17) describe different waveforms of the FT and ST mode in an anisotropic elastic tissue (figure 4.12). A mean wave mode is obtained an elliptic equation with coefficients e_1, e_2, e_3 and e_6 (4.19) predicting two conversely rotated ellipses whose intercepts precisely describe the geometric mean of the FT and ST wave modes. Thus for the elastic scenario where C_{11}, C_{33} and μ_{13} are equal to each other the proposed elliptic expression coincides with the complete $\omega_{1,2}$-solution. For arbitrary combinations of these elastic coefficients the ellipses approximate fast and slow running shear waves as a single mean shear wave that conveys the entire elastic information. This important property of the elliptic approximation can be used to estimate the coefficient E_3 that is not accessible by axial wave profiles. Furthermore, in anisotropic media C_{11} and μ_{13} are not necessarily related to the axial wavelengths λ_1 and λ_3. In the presence of internal interferences ($R' < 3$) these profiles would reveal a shorter apparent wavelength and thus, both C_{11} and μ_{13} are underestimated. The elliptic approximation is capable of yielding the ratios C_{11}/μ_{13} and C_{33}/μ_{13}, by simply considering a specific apparent waveform. In the case of V-waves the elastic parameters that constrain this unique waveform are illustrated in figure 4.17. The thresholds R and R' that determine the range of possible elastic coefficients are derived from considerations about the straightness of the wave fronts and the degree of internal interferences. Both criteria were found by simulations to be the simplest and most objective waveform-parameters that can predict the occurrence of V-waves in terms of E_1, E_2 and μ_{13}. Although the empirically found thresholds of $R > 6$ and $R' > 3$ do not express analytical limits, they provide a practical means to immediately conclude about the probable elasticity behind V-waves. Therefore, the important information carried by in vivo wave images is the occurrence of V-waveform itself. The specific angle α_V displays a means to further refine the possible elastic parameters indicating that the shear wave speed parallel to the muscle fibers is about four times faster than perpendicular to them. The same directional dependence of the shear wave speed was found by ultrasound elastography Gennisson et al. [2003], which demonstrates the feasibility of the new developed waveform analysis to investigate the elastic anisotropy of muscle by MRE.

The elastic anisotropy of human muscle tissue was further elucidated by a 3D analysis in section 4.3.4 using a new developed group velocity inversion technique. In this approach, anisotropic elastic parameters are derived by means of the directional dependency of group velocities over profiles, in contrast to the 2D waveform analysis discussed in the previous section. Using GVI, it is possible to adapt the spatial sector of wave inversion to a boundary-free ROI. This can be particularly important for evaluating MRE experiments of thin muscle layers or less separated muscle groups Jenkyn et al. [2003], Heers et al. [2003], Uffmann et al. [2004], Bensamoun et al. [2006]. As figure 4.24 illustrates, the anisotropy of wave propagation was analyzed within a sector of ±60° relative to the principal axis of the biceps. As a result, the determined shear modulus μ_{12} well reproducible as shown in table 4.1. Since this elastic parameter is related to the short axis of the biceps, it indicates the stability of the method against boundary effects. Few in vivo data regarding shear moduli perpendicular to skeletal muscle fibers are available from US elastography or MRE studies. These data also vary considerably. Although values in the range of 0.92 kPa were found by transient US elastography Gennisson et al. [2005], previous MRE studies revealed much higher values of 16 kPa Kruse et al. [2000] and 14.8 kPa Oida Kang et al. [2005]. The 2D waveform analysis yielded values between 3.4 kPa and 8 kPa Papazoglou et al. [2005], which is similar to the quantities measured by GVI. However, that analysis revealed much higher values for μ_{13} ($\approx$54 kPa), with a ratio μ_{13}/μ_{12} of approximately 16. In contrast, the GVI study revealed a maximum ratio of 6.03 ± 1.69 (volunteer 1). The difference may be due to the elliptical wave form predicted by the ST mode that was not seen in the MRE wave data of the biceps. It was previously shown that straight waves emerging as V-waves result from a certain combination of three elastic parameters of a plate model (figure 4.17), which does not support the existence of bulk shear waves in muscle Papazoglou et al. [2005]. The proposed elastic model is the simplest 3D bulk shear wave model for transverse isotropic solids. The absence of reflecting boundaries assumes the absence of shear wave scattering and wave mode conversions. These processes in combination with surface effects surely influence the observed wave shape. Despite this limitation of the model used to explain the correct V-wave shape, it is feasible to fit $v(\varphi)$ curves as demonstrated by figure 4.24. The measured variations for v_1 and v_3 are reasonably low with regard to inverse problems in shear-wave-based elastography Barbone and Gokhale [2004].

The proposed phase gradient method for automatically detecting wave velocities is a robust technique that provides reproducible results even for noisy data with low wave numbers. For such data the enhancement of wave contrast based on symmetry recognition supports an automatic fit of the wave fronts. However, when r covers at least three to four wavelengths, the applied edge detection robustly recognizes wave fronts even without prior symmetry enhancement. It is important to note that GVI requires the image slice to be aligned with the focal wave source similarly to the 2D waveform analysis. This prerequisite fails if bundles of muscle fibers cross the image plane along a bent principal axis of the muscle so that the waves are guided through-plane. In that case, geometrical biases would result in an overestimation of the deduced wave speeds. Such biases can be mitigated by the special property of straight V-waves characterized by self-repeating patterns along the principal axis of the muscle Papazoglou et al. [2005]. This hypothesis is supported by an analysis of position-dependent group velocities with the origin of the coordinate system shifted away from the wave source. The increase of v_1 observed by analyzing elliptic waves was not found for biceps data (compare figures 4.25(b) and 4.26(b)). The projection of the wave speed perpendicular to the muscle fibers remains constant along the muscle axis, as wave patterns repeat themselves parallel to that axis. This waveform is different to the model, which predicts elliptical or circular concentric wave fronts. However, even without revision of the underlying model GVI may benefit from the stability of the apparent wave speed in muscle. In case of image slices dislocated from the point of wave excitation correct wave speeds are found as long as $\mathbf{r}_0$ is parallel to the muscle fibers.

6 Summary

This work demonstrates that correct elasticity reconstruction in MRE requires certain experimental conditions. The MRE experiment has to be based on a-priori knowledge about the spatial structure and the type of elasticity of the object under investigation. Moreover, depending on these properties different data processing strategies have to be employed in order to determine correct elastic constants.

For isotropic materials standard AHI can be used. However, it was shown that diffraction at the actuator plate and presence of the pressure field lead to biases on the observed phase speeds yielding spatial variations of the apparent phase speed even in homogeneous materials. From an experimental point of view it is therefore necessary to adjust motion encoding so that only out-of-image plane displacement is measured. For that case the measured phase is least biased. Moreover, since even under these experimental conditions spatial variations occur, the phase speed has to be spatially averaged. The resulting dispersion of the averaged phase speed can then be explained by plane waves subjected to noise and discretization. From this model a simple relation was found which allows an estimation of the resolution required in the MRE wave image. The correctness of the measured phase speeds thus requires adjustment of the vibration frequency by an a-priori estimate of the elasticity. This approach is particular valuable for the application of MRE to measure global elastic parameters sensitive to diffuse diseases such as liver fibrosis.

In case of presence of an elastic discontinuity, e.g. a tissue interface, it was shown that MRE allows the determination of scattering coefficients. This was achieved by analyzing wave amplitudes. Spatio-temporal filtering was used to separate incident, reflected and transmitted waves at different vibration frequencies. Experimentally, the motion encoding gradients are required to be parallel to the elastic interface. As an example a study on a gel phantom was presented. In this study shear horizontal wave scattering from an interface was used to determine the degree of weldedness of two elastically identical compartments. The analysis may provide insight in more complex scattering phenomena as they occur in heterogeneous structures like the human brain. As a first step in analyzing boundary conditions that can occur in in vivo tissue, the presented study may also play a role for future development of effective medium theories.

Although algebraic inversion techniques that rely on local plane wave assumptions also apply in case of anisotropic materials, the mathematical structure of the anisotropic problem impedes direct wave inversion. For this reason two methods were developed and evaluated in this work, that allow the determination of anisotropic elastic constants from single MRE images. In both methods the typical V-waves observed by MRE in human biceps were investigated. A model of transverse isotropy under plane stress yielded a set of geometric parameters such as straightness of the wavefronts and V-angle,

Isotropy: Algebraic Helmholtz inversion	**Scattering from interfaces**: wave amplitude analysis	**Anisotropy**: group velocity inversion
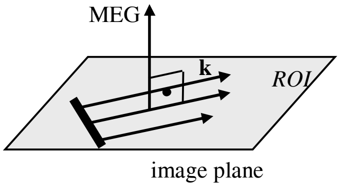	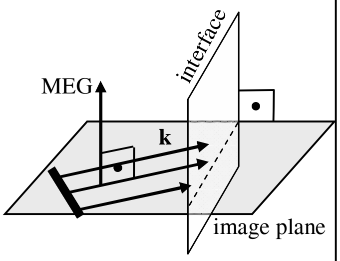	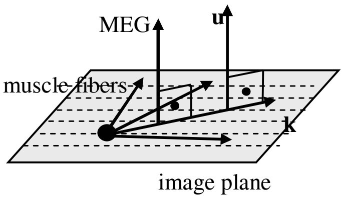
- extended source - out-of-plane motion encoding - phase speeds averaged over *ROI*	- extended source - out-of-plane motion encoding - image plane perpendicular to the interface	- point source - out-of-plane motion encoding - out-of-plane excitation - muscle fibres in image plane

Abbildung 6.1: Experimental setups for correct determination of elastic parameters by AHI, wave amplitude analysis and group velocity inversion.

that fully describe the underlying 2D elasticity tensor. Furthermore, a group velocity inversion employing the full 3D scenario of transverse isotropy was developed and applied to in vivo data. It was demonstrated that the image plane should be selected aligned with the main axis of the elasticity tensor and motion sensitization has to be out-of-plane. Moreover, a point source with through-plane wave excitation is needed in order to measure the slow transverse wave mode. Then, a measurement of group velocity as function of direction of propagation allows the determination of two shear moduli, perpendicular and parallel to the fibers. A noise analysis demonstrated that the developed protocol for group velocity inversion is robust. By this analysis it was shown that anisotropic wave patterns can reveal more information on the anisotropy of human biceps than the evaluation of 1D profiles commonly employed in muscle MRE. The principal requirements for measuring correct elastic constants by shear waves are summarized in figure 6.1.
In summary, MRE is an unique method for measuring elastic constants in isotropic, anisotropic and heterogeneous soft tissue. Since elastic properties depend on structural details on the cellular level MRE provides important information not available by other medical imaging techniques.

Appendix A

Description of Matlab functions.

AHI

Algebraic Helmholtz inversion

Syntax

[cstar, cmedian] = ahi(data, freq, rho, pixsize, filtering, n, k0)

Description

[cstar, cmedian] = ahi(data, freq, rho, pixsize, filtering, n, k0)

returns the local distribution of apparent phase speed CSTAR as determined by algebraic inversion of the Helmholtz equation applied to the 2D complex wave image DATA. CSTAR is a 2D real array of same size as DATA. FREQ is the driving frequency [Hz], PIXSIZE is a two component vector containing the pixel size in the two directions in DATA. CMEDIAN is the apparent phase speed averaged over the whole image excluding a fringe of three pixel width that is subject to errors due to the gradient function. If desired DATA can be low-pass filtered prior to inversion, which is specified by setting the logical variable FILTERING = 1 or true. If FILTERING is any number other than 1 or false, the data are not filtered. As filter a Butterworth filter of order N with spatial frequency cut off at distance K0 from the origin of k-space is used.

Remarks

QUASIHALFSPACE

Calculates the displacement field due to an extended actuator using the quasi half-space approximation given by equation ().

Syntax

u = quasihalfspace(freq,c,platesize,component,fov,matsize,pth)

Description

u = quasihalfspace(freq,c,platesize,component,fov,matsize,pth)

returns the displacement field U. FREQ is the vibration frequency and can be a single scalar or a vector containing all the frequencies at which the field is computed. C is the phase velocity in the material. The column vector PLATESIZE contains the side lengths of the actuator plate. More than one plate size can be given at once, whereby two values in each row give the length of the two perpendicular sides of the plate. The string COMPONENT specifies the Cartesian direction of external vibration and which component of the displacement field is computed. The two component vector FOV contains the side lengths of the field of view (image plane), whereas the two component vector MATSIZE contains the number of pixel in both direction. The string PTH gives the path where U is saved.

Remarks

QUASIHALFSPACE requires the function POINTSOURCE.

POINTSOURCE

Elastic field in an incompressible isotropic material due to a point source according to equation().

Syntax

u = pointsource(x,y,z,Y,Z,cs,f,str)

Description

u = pointsource(x,y,z,Y,Z,cs,f,str)

returns the displacement field U at a position x,y,z due to a point source located at Y, Z. The material is assumed to isotropic, homogeneous and incompressible. CS is the phase velocity in the material. F is the vibration frequency and the string STR specifies which component of the displacement field is desired.

Remarks

TRANSIENTFIELD

Calculates the transient displacement field in a transverse isotropic material.

Syntax

[ux uy uz] = transientfield(scenario,para,ini,u0,flag,mode,time,matsize,L)

Description

[ux uy uz] = transientfield(scenario,para,ini,u0,flag,mode,time,matsize,L)

returns the Cartesian components of the displacement field ux, uy, and uz in k-space at time points given by TIME. MATSIZE is a three component vector containing the pixel size of the 3D k-space. L is a three component vector containing the size of the volume in real space, which is required to determine k-space resolution. The string INI can either be u or v and determines whether displacement or velocity initial conditions are used. The vector PARA contains the numerical values for the elastic constants and has different lengths depending on the SCENARIO:

- PARA = [e1;e3;mu13;nu31;nu21] for SCENARIO = ’compressible’
- PARA = [e1;e3;mu13] for SCENARIO = ’incompressible’
- PARA = [e1;e3;mu13;nu31] for SCENARIO = ’planestress’

MODE = [mode1 mode2 mode3] selects wave modes mode1 = slow transverse, mode2 = fast transverse, mode3 = longitudinal U0 = [ux0 uy0 uz0] initial conditions

Remarks

If velocity initial conditions are used the computed wave data can be employed to find the field due to a harmonic source using the function CONVOLUTE. TRANSIENTFIELD requires the function CHRISTOFFEL.

CHRISTOFFEL

Calculates the components of the Christoffel tensor, which is defined by equation ().

Syntax

g = christoffel(k, para, scenario)

Description

g = christoffel(k, para, scenario)

returns the Christoffel tensor G at position K in k-space. For an explanation of PARA and SCENARIO see the description of the function TRANSIENTFIELD.

Remarks

CONVOLUTE

Convolutes the field computed by TRANSIENTFIELD with a time harmonic excitation

Syntax

u = convolute(time,om,path)

Description

u = convolute(time,om,path)

returns the field U due to a harmonic source.

Remarks

PLANESTRESS

Calculates the field due to a harmonic point source in a transverse isotropic material under the assumption of plane stress using the finite differences as described in appendix B.

Syntax

[u, w] = planestress(C11,C33,MU13,omega,F,damp,width)

Description

[u, w] = planestresss(C11,C33,MU13,omega,F,size,width)

returns the two components of the wave field **u** and **w**. C11, C33 and MU13 are the elastic constants. Omega is the angular frequency, F is the matrix describing the body force, size gives the number of points of the square matrix and width is the side length in expressed in meters.

Remarks

Requires the functions DXDX, DYDY and DXDY.

DXDX

Determines the discretized simple derivative according to the first equation in (.1).

Syntax

dxdx = dxdx(si,delta,bc)

Description

dxdx = dxdx()

Remarks

DYDY

Determines the discretized simple derivative according to the second equation in (.1).

Syntax

dydy = dydy(si,delta,bc)

Description

dydy = dydy()

Remarks

DXDY

Determines the discretized mixed derivative according to equation (.2).

Syntax

dxdy = dxdy(si,delta,ac,bc)

Description

u = dxdy()

Remarks

Appendix B

Description of the numerical methods employed for solving the anisotropic equations of motion. The temporally Fourier transformed equations of motion for plane stress (2.60) are discretized on a square $N \times N$ grid whose lattice points are labeled by (i, j) with $i \in \{1, .., N\}$ and $j \in \{1, .., N\}$ (see figure .2). It is assumed that the pixel are squares of size a. The components of displacement are correspondingly written $u_{i,j} = u_1(x_1, x_3, \omega)$ and $w_{i,j} = u_3(x_1, x_3, \omega)$. For approximating the derivatives occurring in the equations of motion the following difference schemes are chosen for the simple derivatives

$$\begin{aligned} \partial_1^2 u_1(x_1, x_3, \omega) \approx & \quad \frac{1}{a^2}\left(u_{i+1,j} - 2u_{i,j} + u_{i-1,j}\right), \\ \partial_3^2 u_1(x_1, x_3, \omega) \approx & \quad \frac{1}{a^2}\left(u_{i,j+1} - 2u_{i,j} + u_{i,j-1}\right) \end{aligned} \tag{.1}$$

and the symmetric difference scheme

$$\begin{aligned} \partial_1 \partial_3 u_1(x_1, x_3, \omega) \approx & \quad \frac{1}{2a^2}\left(u_{i+1,j+1} - u_{i+1,j} - u_{i,j+1} - u_{i,j}\right) \\ + & \quad \frac{1}{2a^2}\left(u_{i,j} - u_{i-1,j} - u_{i,j-1} - u_{i-1,j-1}\right). \end{aligned} \tag{.2}$$

for the mixed derivatives. The non-reflecting boundary conditions defined by (2.44) are incorporated using the ghost point method (see figure). At a point at the boundary the conditions read in discretized form

$$u_{0+1,j} - u_{0,j} = iaku_{0,j}, \tag{.3}$$

i.e.

$$u_{0,j} = \frac{u_{0+1,j}}{1 + iak}. \tag{.4}$$

Expression (.4) is substituted into the discretized derivatives (.1) and (.2) at the boundary. The procedure is repeated for $u_{j,0}$, $u_{N+1,j}$ and $u_{j,N+1}$ and for w. The values for the

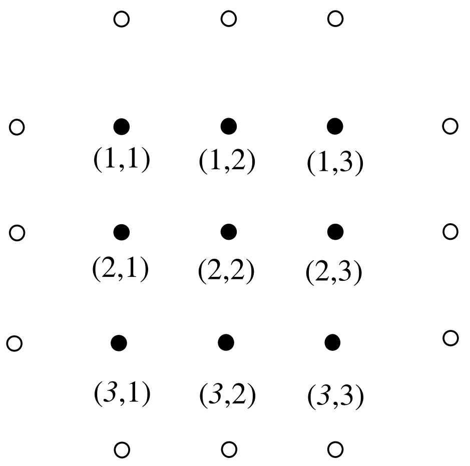

Abbildung .2: Schematic of a 3 × 3 grid. Black points represent reglular points belonging to the lattice while the open circles describe the ghost points used for incorporating the non-reflecting boundary conditions into the finite difference scheme (see text below).

wave number k are determined by substituting the plane waves

$$\begin{aligned} u_1 &= e^{\pm i k_1 x_1} \\ u_2 &= e^{\pm i k_2 x_3} \\ w_3 &= e^{\pm i k_3 x_1} \\ w_4 &= e^{\pm i k_4 x_3} \end{aligned} \tag{.5}$$

into the equations of motion (2.60). Here, the index of u, w and k refers to the boundary as shown in figure . This yields

$$\begin{aligned} k_1 &= \omega \sqrt{\frac{\rho}{C_{11}}} \\ k_2 &= \omega \sqrt{\frac{\rho}{\mu_{13}}} \\ k_3 &= \omega \sqrt{\frac{\rho}{\mu_{13}}} \\ k_4 &= \omega \sqrt{\frac{\rho}{C_{33}}} \end{aligned} \tag{.6}$$

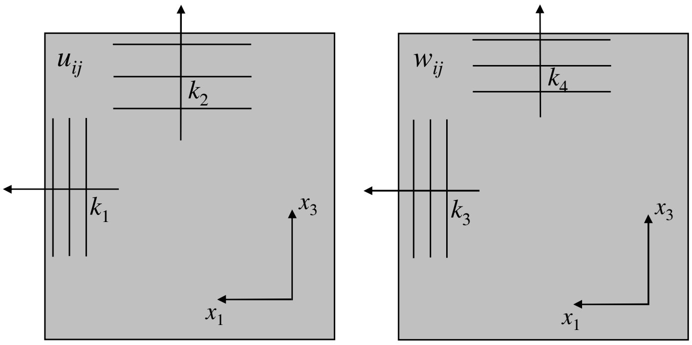

Abbildung .3: It is assumed that at each of the boundaries only outgoing plane waves (.5) exist with the corresponding wave numbers given by (.6).

By changing to the lattice point basis, the combined displacement vector can be written as

$$\begin{bmatrix} u_1(x_1,x_3) \\ u_3(x_1,x_3) \end{bmatrix} = \begin{bmatrix} u_{1,1} \\ \vdots \\ u_{1,N} \\ \vdots \\ u_{M,1} \\ \vdots \\ u_{M,N} \\ w_{1,1} \\ \vdots \\ w_{1,N} \\ \vdots \\ w_{M,1} \\ \vdots \\ w_{M,N} \end{bmatrix} =: \begin{bmatrix} \mathbf{u} \\ \mathbf{w} \end{bmatrix} \tag{.7}$$

With this notation the equation of motion can be written as a matrix equation

$$\begin{bmatrix} \mathbf{D}_1 & \mathbf{D}_{12} \\ \mathbf{D}_{21} & \mathbf{D}_2 \end{bmatrix} \begin{bmatrix} \mathbf{u} \\ \mathbf{w} \end{bmatrix} = \begin{bmatrix} \mathbf{f} \\ \mathbf{0} \end{bmatrix}, \tag{.8}$$

where $\mathbf{D}_1$, $\mathbf{D}_2$ and $\mathbf{D}_{12,21}$ are block diagonal matrices representing the finite differences and incorporating the absorbing boundary conditions. Since they are invertible, the

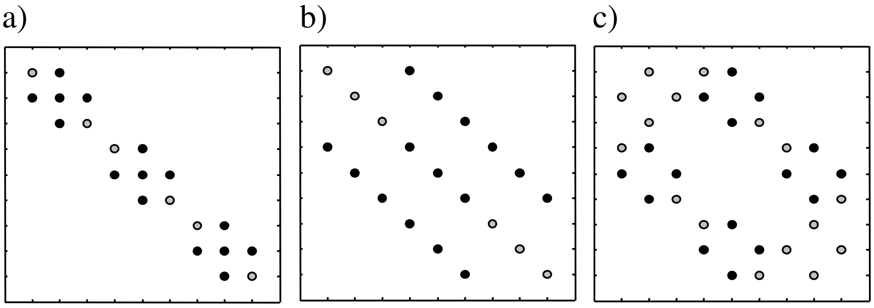

Abbildung .4: This figure shows the sparse structure of the discretized derivatives for the square 3×3 sample grid shown in figure .2: a), b) equations (.1) and c) equation (.2). Gray filled circles demarcate points modified to incorporate the non-reflecting boundary conditions (.4).

solution to (.8) is

$$\begin{bmatrix} \mathbf{u} \\ \mathbf{w} \end{bmatrix} = \begin{bmatrix} \mathbf{D}_1 & \mathbf{D}_{12} \\ \mathbf{D}_{21} & \mathbf{D}_2 \end{bmatrix}^{-1} \begin{bmatrix} \mathbf{f} \\ \mathbf{0} \end{bmatrix} \tag{.9}$$

The two displacement components are then obtained by rearranging the components of the vector $(\mathbf{u}, \mathbf{w})$.

Appendix C

Let λ_1, λ_2 and λ_3 denote the three eigenvalues of the Christoffel tensor and let $\mathbf{U}$ be the matrix whose columns are the corresponding eigenvectors and $\mathbf{V} = \mathbf{U}^{-1}$. In the eigensystem on then has

$$\begin{aligned} \bar{\mathbf{v}} &= \mathbf{V} \cdot \mathbf{v} \\ \bar{\boldsymbol{\Gamma}} = \mathbf{V}\,\boldsymbol{\Gamma}\,\mathbf{U} &= \begin{bmatrix} \omega_1^2(\mathbf{k}) & 0 & 0 \\ 0 & \omega_2^2(\mathbf{k}) & 0 \\ 0 & 0 & \omega_3^2(\mathbf{k}) \end{bmatrix}, \end{aligned} \tag{.10}$$

where the eigenvalues $\omega_{1,2,3}$ correspond to the angular frequencies of the slow transverse (ST), fast transverse (FT) and the longitudinal (L) mode. The solution reads

$$\begin{aligned} \bar{v}_1 &= a_1 \sin \omega_1 t + b_1 \cos \omega_1 t \\ \bar{v}_2 &= a_2 \sin \omega_2 t + b_2 \cos \omega_2 t \\ \bar{v}_3 &= a_3 \sin \omega_3 t + b_3 \cos \omega_3 t. \end{aligned} \tag{.11}$$

The constants a_i and b_i are to be determined by the initial conditions and the solution in the original frame is given by

$$\mathbf{v} = \mathbf{U} \cdot \bar{\mathbf{v}}. \tag{.12}$$

Let the initial values in the original frame be $\mathbf{v}(\mathbf{k}, t = 0) = \mathbf{0}$ and $\dot{\mathbf{v}}(\mathbf{v}, t = 0) = (\dot{u}_{01}, \dot{u}_{02}, \dot{u}_{03})^T$. The solution in the eigensystem then reads

$$\begin{aligned} \bar{v}_1 &= (V_{11}\dot{v}_{01} + V_{12}\dot{v}_{02} + V_{13}\dot{v}_{03}) \sin \omega_1 t \\ \bar{v}_2 &= (V_{21}\dot{v}_{01} + V_{22}\dot{v}_{02} + V_{23}\dot{v}_{03}) \sin \omega_2 t \\ \bar{v}_3 &= (V_{31}\dot{v}_{01} + V_{32}\dot{v}_{02} + V_{33}\dot{v}_{03}) \sin \omega_3 t \end{aligned} \tag{.13}$$

Finally, the components in the original frame can be written as

$$v_i = U_{il} V_{lj} \dot{v}_{0j} \sin \omega_l t, \tag{.14}$$

so that (showing the dependence on $\mathbf{k}$) the solution in position space reads according to (.14) and (3.2)

$$u_i(\mathbf{x}, t) = \frac{1}{(2\pi)^3} \int_{-\infty}^{\infty} U_{il}(\mathbf{k}) V_{lj}(\mathbf{k}) \dot{v}_{0j} \sin \{\omega_l(\mathbf{k}) t\} \, \exp(i\mathbf{k} \cdot \mathbf{x}) \, \mathrm{d}^3 k \tag{.15}$$

Consider now the particular initial condition when $\dot{\mathbf{u}}_0 = [\delta(\mathbf{x}), 0, 0]^T$. The Fourier transform of this initial condition is $[1, 0, 0]^T$. Then the solution (.15) is

$$g_i(\mathbf{x}, t) = \frac{1}{(2\pi)^3} \int_{-\infty}^{\infty} U_{il}(\mathbf{k}) V_{l1}(\mathbf{k}) \sin\{\omega_l(\mathbf{k})t\} \exp(i\mathbf{k} \cdot \mathbf{x}) \; \mathrm{d}^3 k. \tag{.16}$$

For an arbitrary source time function $f(t)$ the solution is given by the convolution

$$w_i(\mathbf{x}, t) = \int_0^t g_i(\mathbf{x}, t - \tau) f(\tau) \mathrm{d}\tau, \tag{.17}$$

or correspondingly in frequency domain by the product

$$\hat{w}_i(\mathbf{x}, \omega) = \hat{w}(\mathbf{x}, \omega) \hat{f}(\omega). \tag{.18}$$

Literaturverzeichnis

K. Aki and P.G. Richards. *Quantitative Seismology*. University Science Books, Sausalito, California, USA, 2nd edition, 2002.

P.E. Barbone and N.H. Gokhale. Elastic modulus imaging: on the uniqueness and nonuniqueness of the elastography inverse problem in two dimensions. *Inverse Problems*, 20(1):283–296, FEB 2004. ISSN 0266-5611. doi: {10.1088/0266-5611/20/1/017}.

J.R. Basford, T.R. Jenkyn, K.N. An, R.L. Ehman, G. Heers, and K.R. Kaufman. Evaluation of healthy and diseased muscle with magnetic resonance elastography. *Archives of Physical Medicine and Rehabilitation*, 83(11):1530–1536, NOV 2002. ISSN 0003-9993. doi: {10.1053/apmr.2002.35472}.

N. Benech and C.A. Negreira. Longitudinal and lateral low frequency head wave analysis in soft media. *Journal of the Acoustical Society of America*, 117(6):3424–3431, JUN 2005. ISSN 0001-4966. doi: {10.1121/1.1920147}.

S.F. Bensamoun, S. Ringleb, Q. Chen, T. Hulshizer, P. Rossma, R.L. Ehman, and K.N. An. Preliminary database of thigh muscle stiffness using magnetic resonance elastography. In *Proceedings of the ISMRM 13th Scientific Meeting & Exhibition, Miami Beach*, 2005.

S.F. Bensamoun, S.I. Ringleb, L. Littrell, Q.S. Chen, M. Brennan, R.L. Ehman, and K.N. An. Determination of thigh muscle stiffness using magnetic resonance elastography. *Journal of Magnetic Resonance Imaging*, 23(2):242–247, FEB 2006. ISSN 1053-1807. doi: {10.1002/jmri.20487}.

S.F. Bensamoun, K.J. Glaser, S.I. Ringleb, Q. Chen, R.L. Ehman, and K.N. An. Rapid magnetic resonance elastography of muscle using one-dimensional projection. *Journal of Magnetic Resonance Imaging*, 27(5):1083–1088, MAY 2008. ISSN 1053-1807. doi: {10.1002/jmri.21307}.

M.A. Bernstein, K.F King, and X.J. Zhou. *Handbook of MRI Pulse Sequences*. Elsevier Academic Press, San Diego, California, USA, 1st edition, 2004.

J. Bishop, A. Samani, J. Sciarretta, and D.B. Plewes. Two-dimensional MR elastrography with linear inversion reconstruction: methodology and noise analysis. *Physics in Medicine and Biology*, 45(8):2081–2091, AUG 2000. ISSN 0031-9155.

F. Bloch. Nuclear Induction. *Physical Review*, 70(7-8):460–474, 1946. ISSN 0031-899X.

J. Braun. In vivo magnetic resonance of the human brain using ultrafast acquisition techniques. In *Proceedings of the ISMRM 10th Scientific Meeting & Exhibition, Honolulu*, 2002.

J. Braun, G. Buntkowsky, J. Bernarding, T. Tolxdorff, and I. Sack. Simulation and analysis of magnetic resonance elastography wave images using coupled harmonic oscillators and Gaussian local frequency estimation. *Magnetic Resonance Imaging*, 19(5): 703–713, JUN 2001. ISSN 0730-725X.

J. Braun, K. Braun, and I. Sack. Electromagnetic actuator for generating variably oriented shear waves in MR elastography. *Magnetic Resonance in Medicine*, 50(1):220–222, JUL 2003. ISSN 0740-3194. doi: {10.1002/mrm.10479}.

S. Catheline, F. Wu, and M. Fink. A solution to diffraction biases in sonoelasticity: The acoustic impulse technique. *Journal of the Acoustical Society of America*, 105(5):2941–2950, MAY 1999. ISSN 0001-4966.

D.L. Colton and R. Kress. *Inverse Acoustic and Electromagnetic Scattering Theory*. Springer-Verlag, Berlin, Germany, 1st edition, 1997.

M.A. Dresner, G.H. Rose, P.J. Rossman, R. Muthupillai, A. Manduca, and R.L. Ehman. Magnetic resonance elastography of skeletal muscle. *Journal of Magnetic Resonance Imaging*, 13(2):269–276, FEB 2001. ISSN 1053-1807.

F.I. Fedorov. *Theory of Elastic Waves in Crystals*. Plenum Press, New York, USA, 1968.

D.A. Feinberg, L. Crooks, J. Hobnninger, M. Arakawa, and J. Watts. Pulsatile Blood Velocity in Human Arteries Displayed by Magnetic-Resonance Imaging. *Radiology*, 153(1):177–180, 1984. ISSN 0033-8419.

Y. C. Fung. *Biomechanics*. Springer-Verlag, New York, USA, 2nd edition, 1993.

C.J. Galban, B.L. Maderwald, S. Herrmann, K. Brauck, A. de Greiff, K. Uffmann, and M.E. Ladd. Measuring skeletal muscle elasticity in patients with hypogonadism by mr elastography. In *Proceedings of the ISMRM 13th Scientific Meeting & Exhibition, Miami Beach*, 2005a.

C.J. Galban, H. Maderwald, S. Eggebrecht, W. Grote, A. de Greiff, K. Uffmann, and M.E. Ladd. Monitoring the effects of chronic obstructive pulmonary disease on muscle elasticity by mr elastography. In *Proceedings of the ISMRM 13th Scientific Meeting & Exhibition, Miami Beach*, 2005b.

J.L. Gennisson, S. Catheline, S. Chaffai, and M. Fink. Transient elastography in anisotropic medium: Application to the measurement of slow and fast shear wave speeds in muscles. *Journal of the Acoustical Society of America*, 114(1):536–541, JUL 2003. ISSN 0001-4966. doi: {10.1121/1.1579008}.

J.L. Gennisson, C. Cornu, S. Catheline, M. Fink, and P. Portero. Human muscle hardness assessment during incremental isometric contraction using transient elastography. *Journal of Biomechanics*, 38(7):1543–1550, JUL 2005. ISSN 0021-9290. doi: {10.1016/j.jbiomech.2004.07.013}.

E.L. Hahn. Spin Echoes. *Physical Review*, 80(4):580–594, 1950. ISSN 0031-899X.

U. Hamhaber, I. Sack, S. Papazoglou, J. Rump, D. Klatt, and J. Braun. Three-dimensional analysis of shear wave propagation observed by in vivo magnetic resonance elastography of the brain. *Acta Biomaterialia*, 3(1):127–137, JAN 2007. ISSN 1742-7061. doi: {10.1016/j.actbio.2006.08.007}.

G. Heers, T. Jenkyn, M.A. Dresner, M.O. Klein, J.R. Basford, K.R. Kaufman, R.L. Ehman, and K.N. An. Measurement of muscle activity with magnetic resonance elastography. *Clinical Biomechanics*, 18(6):537–542, JUL 2003. ISSN 0268-0033. doi: {10.1016/S0268-0033(03)00070-6}.

D.I. Hoult and R.E. Richards. Signal-to-Noise Ratio of the Nuclear Magnetic-Resonance Experiment. *Journal of Magnetic Resonance*, 24(1):71–85, 1976. ISSN 1090-7807.

J.D. Humphrey. Continuum biomechanics of soft biological tissues. *Proceedings of the Royal Society A-Mathematical Physical and Engineering Sciences*, 459(2029):3–46, JAN 8 2003. ISSN 1364-5021. doi: {10.1098/rspa.2002.1060}.

L. Huwart, F. Peeters, R. Sinkus, L. Annet, N. Salameh, L.C. ter Beek, Y. Horsmans, and B.E. Van Beers. Liver fibrosis: non-invasive assessment with MR elastography. *NMR in Biomedicine*, 19(2):173–179, APR 2006. ISSN 0952-3480. doi: {10.1002/nbm.1030}.

E.K. Insko, M.A. Elliott, J.C. Schotland, and J.S. Leigh. Generalized reciprocity. *Journal of Magnetic Resonance*, 131(1):111–117, MAR 1998. ISSN 1090-7807.

T.R. Jenkyn, R.L. Ehman, and K.N. An. Noninvasive muscle tension measurement using the novel technique of magnetic resonance elastography (MRE). *Journal of Biomechanics*, 36(12):1917–1921, DEC 2003. ISSN 0021-9290. doi: {10.1016/S0021-9290(03)00005-8}.

D. Klatt, P. Asbach, J. Rump, S. Papazoglou, R. Somasundaram, J. Modrow, J. Braun, and I. Sack. In vivo determination of hepatic stiffness using steady-state free precession magnetic resonance elastography. *Investigative Radiology*, 41(12):841–848, DEC 2006. ISSN 0020-9996.

D. Klatt, U. Hamhaber, P. Asbach, J. Braun, and I. Sack. Noninvasive assessment of the rheological behavior of human organs using multifrequency MR elastography: a study of brain and liver viscoelasticity. *Physics in Medicine and Biology*, 52(24):7281–7294, DEC 21 2007. ISSN 0031-9155. doi: {10.1088/0031-9155/52/24/006}.

H. Knutsson, C.J. Westin, and G. Granlund. Local multiscale frequency and bandwidth estimation. In *Proceedings of the IEEE International Conference on Image Processing*, 1994.

S.A. Kruse, J.A. Smith, A.J. Lawrence, M.A. Dresner, A. Manduca, J.F. Greenleaf, and R.L. Ehman. Tissue characterization using magnetic resonance elastography: preliminary results. *Physics in Medicine and Biology*, 45(6):1579–1590, JUN 2000. ISSN 0031-9155.

S.A. Kruse, G.H. Rose, K.J. Glaser, A. Manduca, J.P. Felmlee, C.R. Jack, Jr., and R.L. Ehman. Magnetic resonance elastography of the brain. *Neuroimage*, 39(1):231–237, JAN 1 2008. ISSN 1053-8119. doi: {10.1016/j.neuroimage.2007.08.030}.

W.M. Lai. *Introduction to Continuum Mechanics*. Butterworth-Heinemann, USA, 3rd edition, 1994.

L.D. Landau and E.M. Lifshitz. *Theory of Elasticity*. Butterworth-Heinemann, USA, 3rd edition, 1986.

R.M. Lerner, S.R. Huang, and K.J. Parker. Sonoelasticity Images Derived from Ultrasound Signals in Mechanically Vibrated Tissues. *Ultrasound in Medicine and Biology*, 16(3):231–239, 1990. ISSN 0301-5629.

C.J. Lewa and J.D. DeCertaines. Viscoelastic property detection by elastic displacement NMR measurements. *Journal of Magnetic Resonance Imaging*, 6(4):652–656, JUL-AUG 1996. ISSN 1053-1807.

A Lhemery. A Model for the Transient Ultrasonic-Field Radiated by an Arbitrary Loading in a Solid. *Journal of the Acoustical Society of America*, 96(6):3776–3786, DEC 1994. ISSN 0001-4966.

Z.P. Liang and P.C. Lauterbur. *Principles of Magnetic Resonance Imaging*. Wiley-IEEE Press, New York, USA, 1st edition, 2000.

J. Lorenzen, R. Sinkus, M. Lorenzen, M. Dargatz, C. Leussler, P. Roschmann, and G. Adam. MR elastography of the breast: preliminary clinical results. *Fortschritte auf dem Gebiet der Röntgenstrahlen und der bildgebenden Verfahren*, 174(7):830–834, JUL 2002. ISSN 1438-9029.

A. Manduca, D.S. Lake, S.A. Kruse, and R.L. Ehman. Spatio-temporal directional filtering for improved inversion of MR elastography images. *Medical Image Analysis*, 7 (4):465–473, DEC 2003. ISSN 1361-8415. doi: {10.1016/S1361-8415(03)00038-0}. 5th International Conference on Medical Image Computing and Computer-Assisted Intervention, TOKYO, JAPAN, SEP 25-28, 2002.

P.J. McCracken, A. Manduca, J. Felmlee, and R.L. Ehman. Mechanical transient-based magnetic resonance elastography. *Magnetic Resonance in Medicine*, 53(3):628–639, MAR 2005. ISSN 0740-3194. doi: {10.1002/mrm.20388}.

P.R. Moran. A flow zeugmatographic interlace for nmr imaging in humans. *Magnetic Resonance Imaging*, 1:197–203, 1982.

M.J.P. Musgrave. *Crystal Acoustics*. Holden.Day, San Francisco, California, USA, 1st edition, 1970.

R. Muthupillai, D.J. Lomas, P.J. Rossmann, J.F. Greenleaf, A. Manduca, and R.L. Ehman. Magnetic-Resonance Elastography by Direct Visualization of Propagating Acoustic Strain Waves. *Science*, 269(5232):1854–1857, SEP 29 1995. ISSN 0036-8075.

R. Muthupillai, P.J. Rossman, D.J. Lomas, J.F. Greenleaf, S.J. Riederer, and R.L. Ehman. Magnetic resonance imaging of transverse acoustic strain waves. *Magnetic Resonance in Medicine*, 36(2):266–274, AUG 1996. ISSN 0740-3194.

Y. Oida Kang, T. Azuma, J. Okamoto, A. Amano, L. Axel, O. Takizawa, S. Tsutsumi, and T Matsuda. The measurement of anisotropic elasticity in skeletal muscle using mr elastography. In *Proceedings of the ISMRM 13th Scientific Meeting & Exhibition, Miami Beach*, 2005.

T.E. Oliphant, A. Manduca, R.L. Ehman, and J.F. Greenleaf. Complex-valued stiffness reconstruction for magnetic resonance elastography by algebraic inversion of the differential equation. *Magnetice Resonance in Medicine*, 45(2):299–310, FEB 2001. ISSN 0740-3194.

J. Ophir, I. Cespedes, H. Ponnekanti, Yazdi Y., and X. LI. Elastography - A Quantitative Method for Imaging the Elasticity of Biological Tissues. *Ultrasound Imaging*, 13(2): 111–134, APR 1991. ISSN 0161-7346.

S. Papazoglou, J. Braun, U. Hamhaber, and I. Sack. Two-dimensional waveform analysis in MR elastography of skeletal muscles. *Physics in Medicine and Biology*, 50(6): 1313–1325, MAR 21 2005. ISSN 0031-9155. doi: {10.1088/0031-9155/50/6/018}.

S. Papazoglou, J. Rump, J. Braun, and I. Sack. Shear wave group velocity inversion in MR elastography of human skeletal muscle. *Magnetic Resonance in Medicine*, 56(3): 489–497, SEP 2006. ISSN 0740-3194. doi: {10.1002/mrm.20993}.

S. Papazoglou, U. Hamhaber, J. Braun, and I. Sack. Horizontal shear wave scattering from a nonwelded interface observed by magnetic resonance elastography. *Physics in Medicine and Biology*, 52(3):675–684, FEB 7 2007. ISSN 0031-9155. doi: {10.1088/0031-9155/52/3/010}.

E. Park and A.M. Maniatty. Shear modulus reconstruction in dynamic elastography: time harmonic case. *Physics in Medicine and Biology*, 51(15):3697–3721, AUG 7 2006. ISSN 0031-9155. doi: {10.1088/0031-9155/51/15/007}.

K.J. Parker, S.R. Huang, R.A. Musulin, and R.M. Lerner. Tissue-Response to Mechanical Vibrations for Sonoelasticity Imaging. *Ultrasound in Medicine and Biology*, 16(3):241–246, 1990. ISSN 0301-5629.

D.B. Plewes, I. Betty, S.N. Urchuk, and I. Soutar. Visualizing tissue compliance with MR imaging. *Journal of Magnetic Resonance Imaging*, 5(6):733–738, NOV-DEC 1995. ISSN 1053-1807.

S.I. Ringleb, S.F. Bensamoun, Q. Chen, A. Manduca, K. An, and R.L. Ehman. Applications of magnetic resonance elastography to healthy and pathologic skeletal muscle. *Journal of Magnetic Resonance Imaging*, 25(2):301–309, FEB 2007. ISSN 1053-1807. doi: {10.1002/jmri.20817}.

O. Rouviere, M. Yin, M.A. Dresner, P.J. Rossman, L.J. Burgart, J.L. Fidler, and R.L. Ehman. MR elastography of the liver: Preliminary results. *Radiology*, 240(2):440–448, AUG 2006. ISSN 0033-8419. doi: {10.1148/radiol.2402050606}.

J. Rump, D. Klatt, C. Warmuth, J. Braun, U. Hamhaber, S. Papazoglou, and I. Sack. Synchronisation of shear vibrations and balanced stead state free precession in mr elastography. In *Proceedings of the ISMRM 13th Scientific Meeting & Exhibition, Miami Beach*, 2005.

J. Rump, D. Klatt, J. Braun, C. Warmuth, and I. Sack. Fractional encoding of harmonic motions in MR elastography. *Magnetic Resonance in Medicine*, 57(2):388–395, FEB 2007. ISSN 0740-3194. doi: {10.1002/mrm.21152}.

I. Sack, A. Samani, D.B. Plewes, and J. Braun. Simulation of in vivo mr elastography wave patterns of skeletal muscle using a transverse isotropic elasticity model. In *Proceedings of the ISMRM 11th Scientific Meeting & Exhibition, Toronto*, 2003.

I. Sack, S. Papazoglou, U. Hamhaber, D. Klatt, J. Rump, and J. Braun. Shear wave scattering in mr elastography: Detection of elastic interfaces. In *Proceedings of the ISMRM 13th Scientific Meeting & Exhibition, Miami Beach*, 2005.

I. Sack, J. Rump, S. Papazoglou, D. Klatt, U. Hamhaber, E. Gedat, and J. Braun. Enhancement in steady-state mr elastography. In *Proceedings of the ISMRM 14th Scientific Meeting & Exhibition, Seattle*, 2006.

I. Sack, J. Bernarding, and J. Braun. Analysis of wave patterns in MR elastography of skeletal muscle using coupled harmonic oscillator simulations. *Magnetic Resonance Imaging*, 20(1):95–104, JAN 2002. ISSN 0730-725X.

I. Sack, B. Beierbach, U. Hamhaber, D. Klatt, and J. Braun. Non-invasive measurement of brain viscoelasticity using magnetic resonance elastography. *NMR in Biomedicine*, 21(3):265–271, MAR 2008. ISSN 0952-3480. doi: {10.1002/nbm.1189}.

J. Salo and M.M. Salomaa. Nondiffracting waves in anisotropic media. *Physical Review E*, 67(5, Part 2), MAY 2003. ISSN 1063-651X. doi: {10.1103/PhysRevE.67.056609}.

L. Sandrin, D. Cassereau, and M. Fink. The role of the coupling term in transient elastography. *Journal of the Acoustical Society of Amercia*, 115(1):73–83, JAN 2004. ISSN 0001-4966. doi: {10.1121/1.1635412}.

A Sarvazyan. Mechanical imaging: A new technology for medical diagnostics. *International Journal of Medical Informatics*, 49(2):195–216, APR 1998. ISSN 1386-5056. 10th IEEE Symposium on Computer-Based Medical Systems, MARIBOR, SLOVENIA, JUN 11-13, 1997.

G. M. Schoenberg. Elastic Wave Behavior Across Linear Slip Interfaces. *Journal of the Acoustical Society of America*, 68(5):1516–1521, 1980. ISSN 0001-4966.

R. Sinkus, J. Lorenzen, D. Schrader, M. Lorenzen, M. Dargatz, and D. Holz. High-resolution tensor MR elastography for breast tumour detection. *Physics in Medicine and Biology*, 45(6):1649–1664, JUN 2000. ISSN 0031-9155.

R. Sinkus, M. Tanter, S. Catheline, J. Lorenzen, C. Kuhl, E. Sondermann, and M. Fink. Imaging anisotropic and viscous properties of breast tissue by magnetic resonance-elastography. *Magnetic Resonance in Medicine*, 53(2):372–387, FEB 2005a. ISSN 0740-3194. doi: {10.1002/mrm.20355}.

R. Sinkus, M. Tanter, T. Xydeas, S. Catheline, J. Bercoff, and M. Fink. Viscoelastic shear properties of in vivo breast lesions measured by MR elastography. *Magnetic Resonance in Medicine*, 23(2, Sp. Iss. SI):159–165, FEB 2005b. ISSN 0730-725X. doi: {10.1016/j.mri.2004.11.060}. 7th International Conference on Magnetic Resonance in Porous Media (MRPM7), Palaiseau, FRANCE, JUL 04-08, 2004.

R. Sinkus, K. Siegmann, T. Xydeas, M. Tanter, C. Claussen, and M. Fink. MR elastography of breast lesions: Understanding the solid/liquid duality can improve the specificity of contrast-enhanced MR mammography. *Magnetic Resonance in Medicine*, 58(6):1135–1144, DEC 2007. ISSN 0740-3194. doi: {10.1002/mrm.21404}.

A.R. Skovoroda, S.Y. Emelianov, and M. ODonnel. Tissue Elasticity Reconstruction Based on Ultrasonics Displacement and Strain Images. *IEEE Transactions on Ultrasonics Ferroelectrics and Frequency Control*, 42(4):747–765, JUL 1995. ISSN 0885-3010.

C.P. Slichter. *Principles of Magnetic Resonance*. Springer Series in Solid State Sciences, Springer, Berlin, Germany, 3rd edition, 1992.

E.O. Stejskal and J.E. Tanner. Spin Diffusion Measurements: Spin Echoes in the Presence of a Time-Dependent Field Gradient. *Journal of Chemical Physics*, 42(1):288+, 1965. ISSN 0021-9606.

B. Taylor, H.J. Maris, and C. Elbaum. Phonon Focusing in Solids. *Physical Review Letters*, 23(8):416–&, 1969. ISSN 0031-9007.

H.C. Torrey. Bloch Equations with Diffusion Terms. *Physical Review*, 104(3):563–565, 1956. ISSN 0031-899X.

K. Uffmann, S. Maderwald, W. Ajaj, C.G. Galban, S. Mateiescu, H.H. Quick, and M.E. Ladd. In vivo elasticity measurements of extremity skeletal muscle with MR elastography. *NMR in Biomedicine*, 17(4):181–190, JUN 2004. ISSN 0952-3480. doi: {10.1002/nbm.887}.

E.E.W. Van Houten, K.D. Paulsen, I. Miga, F.E. Kennedy, and J.B. Weaver. An overlapping subzone technique for MR-based elastic property reconstruction. *Magnetic Resonance in Medicine*, 42(4):779–786, OCT 1999. ISSN 0740-3194.

E.E.W. Van Houten, J.B. Weaver, M.I. Miga, F.E. Kennedy, and K.D. Paulsen. Elasticity reconstruction from experimental MR displacement data: initial experience with an overlapping subzone finite element inversion process. *Medical Physics*, 27(1):101–107, JAN 2000. ISSN 0094-2405.

E.E.W. Van Houten, M.M. Doyley, F.E. Kennedy, J.B. Weaver, and K.D. Paulsen. Initial in vivo experience with steady-state subzone-based MR elastography of the human breast. *Journal of Magnetic Resonance Imaging*, 17(1):72–85, JAN 2003. ISSN 1053-1807. doi: {10.1002/jmri.10232}.

S. Webb, editor. *The Physics of Medical Imaging*. IOP Publishing Ltd., Bristol, UK, 1st edition, 1988.

Y. Yamakoshi, J. Sato, and T. Sato. Ultrasonic-Imaging of Internal Vibration of Soft-Tissue Under Forced Vibration. *IEEE Transactions on Ultrasonics Ferroelectrics and Frequency Control*, 37(2):45–53, MAR 1990. ISSN 0885-3010.

M. Yin, J.A. Talwalkar, K.J. Glaser, A. Manduca, R.C. Grimm, P.J. Rossman, J.L. Fidler, and R.L. Ehman. Assessment of hepatic fibrosis with magnetic resonance elastography. *Clinical Gastroenterology and Hepatology*, 5(10):1207–1213, OCT 2007. ISSN 1542-3565. doi: {10.1016/j.cgh.2007.06.012}.

M. Ziol, A. Handra-Luca, A. Kettaneh, C. Christidis, F. Mal, F. Kazemi, V. de Ledinghen, P. Marcellin, D. Dhumeaux, J.C. Trinchet, and M. Beaugrand. Noninvasive assessment of liver fibrosis by measurement of stiffness in patients with chronic hepatitis C. *Hepatology*, 41(1):48–54, JAN 2005. ISSN 0270-9139. doi: {10.1002/hep.20506}.

Abbildungsverzeichnis

Tabellenverzeichnis

Selbstständigkeitserklärung

Hiermit versichere ich, Sebastian Papazoglou, dass ich keine anderen als die genannten Quellen zum Erstellen dieser Arbeit verwendet habe und die vorliegende Arbeit selbstständig verfasst habe.

Berlin den 19.12.2009